William & Mary
CHARTERED 1693

W&M ScholarWorks

Dissertations, Theses, and Masters Projects

Theses, Dissertations, & Master Projects

1996

Surface reflection hyperthermal neutral stream source

Christopher A. Nichols
College of William & Mary - Arts & Sciences

Follow this and additional works at: https://scholarworks.wm.edu/etd

Part of the Materials Science and Engineering Commons, and the Plasma and Beam Physics Commons

Recommended Citation

Nichols, Christopher A., "Surface reflection hyperthermal neutral stream source" (1996). *Dissertations, Theses, and Masters Projects.* Paper 1539623889.
https://dx.doi.org/doi:10.21220/s2-s326-ak59

This Dissertation is brought to you for free and open access by the Theses, Dissertations, & Master Projects at W&M ScholarWorks. It has been accepted for inclusion in Dissertations, Theses, and Masters Projects by an authorized administrator of W&M ScholarWorks. For more information, please contact scholarworks@wm.edu.

INFORMATION TO USERS

This manuscript has been reproduced from the microfilm master. UMI films the text directly from the original or copy submitted. Thus, some thesis and dissertation copies are in typewriter face, while others may be from any type of computer printer.

The quality of this reproduction is dependent upon the quality of the copy submitted. Broken or indistinct print, colored or poor quality illustrations and photographs, print bleedthrough, substandard margins, and improper alignment can adversely affect reproduction.

In the unlikely event that the author did not send UMI a complete manuscript and there are missing pages, these will be noted. Also, if unauthorized copyright material had to be removed, a note will indicate the deletion.

Oversize materials (e.g., maps, drawings, charts) are reproduced by sectioning the original, beginning at the upper left-hand corner and continuing from left to right in equal sections with small overlaps. Each original is also photographed in one exposure and is included in reduced form at the back of the book.

Photographs included in the original manuscript have been reproduced xerographically in this copy. Higher quality 6" x 9" black and white photographic prints are available for any photographs or illustrations appearing in this copy for an additional charge. Contact UMI directly to order.

UMI

A Bell & Howell Information Company
300 North Zeeb Road, Ann Arbor MI 48106-1346 USA
313/761-4700 800/521-0600

Reproduced with permission of the copyright owner. Further reproduction prohibited without permission.

Reproduced with permission of the copyright owner. Further reproduction prohibited without permission.

SURFACE REFLECTION HYPERTHERMAL NEUTRAL STREAM SOURCE

A Dissertation

Presented to The Faculty of the Department of Applied Science

The College of William and Mary

In Partial Fulfillment

Of the Requirements for the Degree of

Doctor of Philosophy

By

Christopher A. Nichols

June 1996

Reproduced with permission of the copyright owner. Further reproduction prohibited without permission.

UMI Number: 9720977

Copyright 1997 by
Nichols, Christopher Allan

All rights reserved.

UMI Microform 9720977
Copyright 1997, by UMI Company. All rights reserved.

This microform edition is protected against unauthorized
copying under Title 17, United States Code.

UMI
300 North Zeeb Road
Ann Arbor, MI 48103

Reproduced with permission of the copyright owner. Further reproduction prohibited without permission.

APPROVAL SHEET

This dissertation is submitted in partial fulfillment
of the requirements for the degree of

Doctor of Philosophy.

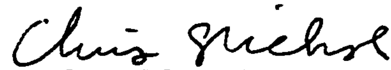

Christopher A. Nichols

Approved, June 1996

Dennis M. Manos

Lawrence Leemis
Department of Mathematics

Harlan Schone

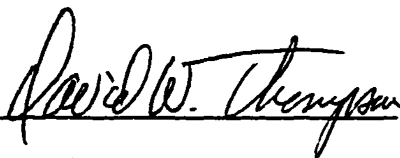

David Thompson

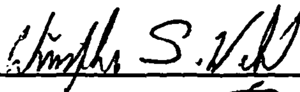

Chris Welch

Reproduced with permission of the copyright owner. Further reproduction prohibited without permission.

Dedicated to

Memaw,

for putting me in college,

and

Cathy,

for keeping me there.

Reproduced with permission of the copyright owner. Further reproduction prohibited without permission.

Contents

Acknowledgments vii

List of Tables x

List of Figures xi

Abstract xiii

Chapter 1 Introduction 2

1.1 Neutral Stream Processing 2

1.2 Devices and Charge-Induced Damage 6

1.3 Organization of this Thesis 9

Chapter 2 Theory of Operation 11

2.1 Plasma Concepts 11

2.1.1 Sheaths 13

2.1.2 Creation of Plasma Species 18

2.1.3 Inductive Coupling 21

2.2 Surface Reflection 26

Reproduced with permission of the copyright owner. Further reproduction prohibited without permission.

2.2.1 Reflection Characteristics 30

2.2.2 Effect of Applied Magnetic Field 30

2.3 Hyperthermal Neutral Stream Source Description 31

Chapter 3 Neutral Stream Source Modeling **35**

3.1 Introduction 35

3.2 Vacuum System Modeling 36

3.2.1 Vacuum System Transient Simulator 38

3.2.2 VSTS Results 45

3.2.3 VSTS Conclusions 53

3.3 3-D Ray-Tracing Model 53

3.3.1 3-D Model Description 53

3.3.2 3-D Ray-Trace Results 54

3.4 2-D Ray-Tracing Model 58

3.4.1 Model Descriptions 58

3.4.2 Results of 2-D Modeling 65

Chapter 4 Monte Carlo Simulation **82**

4.1 3-D Monte Carlo Simulation 82

4.2 Description of Model 84

4.3 Results and Discussion 94

4.4 Monte Carlo Conclusions 110

Chapter 5 Neutral Source Performance **113**

Reproduced with permission of the copyright owner. Further reproduction prohibited without permission.

5.1 Plasma Characterization 113
5.1.1 Langmuir Probes 113
5.1.2 Plasma Density Measurements 121
5.2 Etch Rate Characterization 129
5.3 Performance Conclusions 135

Chapter 6 Discussion and Future Work **137**

6.1 Discussion 137
6.2 Future Work 141
6.3 Conclusions 141

Appendix A Ionized Magnetron Sputter Deposition **143**

A.1 Abstract 143
A.2 Introduction 144
A.3 Experiment 145
A.4 Discussion 156
A.5 Conclusions 160

Bibliography **162**

Vita **170**

Reproduced with permission of the copyright owner. Further reproduction prohibited without permission.

Acknowledgments

As one may expect, there are many people without whom this work would not have been completed.

Special thanks go first to Prof. Dennis M. Manos, who was kind enough to take me on as a student on nothing more than a few scattered e-mail messages. This project was hatched in principle during that time, before he even arrived from Princeton. From those first days, Dennis gave me responsibilities and opportunities that few graduate students receive. He has a view that simply doing an experiment and writing a thesis while seeing all other aspects of the research experience as a "black box" that will take care of itself, is not enough to create first-rate scientists. Perhaps the finest example of this trust is the proposal to the National Science Foundation, "Neutral Beam Formation for Semiconductor Processing Application", which he allowed me to write after only a year and a half of graduate school, that was funded in the summer of 1995. Through this experience I was able to see one of the most important aspects of the research process, getting the money to do the work. This process also allowed me to learn much about the physics of my project, even before it began. Again, many thanks to Dennis Manos for his assistance, and just as importantly, his trust.

I would like to thank the members of my committee for coming on board on such short notice. Dr. Larry Leemis of Mathematics, Dr. Harlan Schone of Physics, Dr. David Thompson of Applied Science and Chemistry, and Dr. Chris Welch of Applied Science and NASA-Langley. Their discussions and material assistance were invaluable.

I would like to thank several members of the physics faculty that helped me through my first few years in graduate school. These are Gene Tracy, Roy Champion, Howard Funsten, Charles Perdrisat, Morton Eckhause, and the late Lynn Doverspike. During an internship at CEBAF, Rich Abbott and Ron Lauze' were terrific mentors to whom I owe much gratitude. They were valuable teachers in science and engineering, but more importantly, in how to "get things done".

Dr. Steve Rossnagel of IBM T. J. Watson Research Center in Yorktown Heights, New York invited me to come work with him in his laboratory during the summer of 1995. This work involved the study of Ionized Physical Vapor Deposition (I-PVD) of Cu for interconnects. During this time I was able to get first-hand experience with industrial research. In addition, the deposition nature of the project was completely different than my thesis project, based on etch processes. Many thanks to Steve for teaching me so much about other important aspects of the industrial world.

I would like to thank the graduate students that entered the physics program with me that year: Daniele Gaetano, Rob Martin, Phil Spickler, Maciek Sasiknowski, Jaewhan Oh, and Justin McIntyre. We got through it together, but the Physics qualifier, we did on our

Reproduced with permission of the copyright owner. Further reproduction prohibited without permission.

own. Daniele Gaetano deserves thanks for listening to my very frank criticism about Vortex, his scientific data visualization package. I can say that he took most of my suggestions very well. Although, it is a wonder that we are still good friends.

During my time at William & Mary, I had the privilege of working with some fine undergraduates. Thanks to Brian Tucker, Mike Johnson, Ryan Bubb, Winthrop Brown, Eric Schatz (at IBM) and Rob Bassett. I worked very closely with Rob Bassett, and our friendship continues. Thanks to Rob also for showing me around New York City and giving me someone to hang out with while I was at IBM. Thanks go to Rob Bassett's parents, Bob and Judy Bassett, for giving me a place to stay for a few weeks while I was in working in New York.

Thanks to Chree Haas and Matt Coffey for putting up with my near constant barrage of questions and pleas for assistance about computers and networking. Thanks to my fellow Applied Science grads: Jai Diggs, Adam Friedman (my roomie and office-mate), Joseph Ametepe, Jim Mckeon, Dawn Guilmet, and Tom Venhaus (my other office-mate). Special thanks to Tom for being such a good friend and not running away whenever I needed someone to talk to.

Very special thanks to the William & Mary Physics Machine shop. John Bensel, Kirk Jacobs and Mel Woods. They did great work for me, period. Sometimes they had to work under my schedule, which usually meant that I needed it yesterday, and they came through when they could. When I wanted to do something myself, they would take the time to set me up and give valuable pointers on machining. More importantly, they didn't laugh at my finished product (usually). It is safe to say that without their skill and understanding, this project would never be finished. They are, in short, a credit to the department.

In the physics department, thanks to Paula, Dianne, and Sylvia for their assistance while I was there, and even after I left. Thanks to Kathee Card in Applied Science for valuable assistance.

I would also like to thank Jane Ann and Marilyn at Arkansas State University for their invaluable help and friendship during my undergraduate years. Dr. Charles Hughes and Dr. Lawrence Mink were great instructors and advisors during that time. They spent a lot of time with me and taught me to love physics through their own enthusiasm.

Thanks to my dad, Rick Nichols, and my mom, Diane Ramsey, for bringing me into the world. I hope I will continue to make them proud. I would like to say thanks to my little sister, Kelly, and my little brother, Joshua. Thanks to my extended families, the Loftis' and the Aikmans. My grandparents, Alene and Ermie (Nana and Papa) Loftis, and Virginia (Memaw) McCartney, always deserve special thanks. I would also like to say thanks to my aunts and uncles, Loy and Nadyne, Jim and Jean, and Karo and Shirley Aikman.

Although they are no longer with us, I have to say that so much of what I am is owed to my great-grandparents, Bill and Anna (Pa and Dear) Aikman. I don't have the words to express what they meant to me, and the entire Aikman family, so I won't try. But the memory of them will always be alive in me. I wish that they could be here now to share in this accomplishment. I hope they would be proud. They were, and continue to be, the best people I have ever known.

The most special thanks of all must go to the two people to whom this thesis is dedicated. My grandmother, Virginia McCartney, affectionately known to my siblings and myself as Memaw, gave me the most encouragement to begin college when it looked I wouldn't. She gave so much moral support through the entire nine year process, as well as more financial support than she could have possibly afforded. I wouldn't have started college if it wasn't

Reproduced with permission of the copyright owner. Further reproduction prohibited without permission.

for her. I doubt I could have finished. Thank you, Memaw.

My wife, Cathy, deserves so much appreciation that I can't express it. She put up with my long absences during trips to IBM and conferences. She put up with those times I had to take one more data point in the lab, and didn't come home until midnight. She put up with my weekends at work. In short, she put up with everything under the sun while I pursued my goals, making them her goals. All of this while working a part-time job and getting her own B. S. in Biology. In May 1996, we had been married for six years, with 12 years since our first date. With all of my love, thank you, Cathy.

One more thing, I'm going to have a baby boy on or around November 18th. His name will be Richard William Nichols.

Reproduced with permission of the copyright owner. Further reproduction prohibited without permission.

List of Tables

3.1 Plasma source conductances 43

4.1 Energy reflection data used in the simulations 87
4.2 General parameter space of device 94

5.1 Parameters for simulation in etch rate analysis 129
5.2 Etch rates and ion fluxes at sample 133

Reproduced with permission of the copyright owner. Further reproduction prohibited without permission.

List of Figures

1.1 Typical ICP plasma source configuration 5
1.2 MOSFET device feature 7
1.3 Device fabrication steps 7

2.1 General plasma configurations. 12
2.2 Maxwellian energy distribution 14
2.3 Sheath formation 15
2.4 Sheath density profiles 17
2.5 Radial magnetic fields in the ICP 23
2.6 Effect of pressure on ICP characteristics 23
2.7 Magnetic multipole confinement 25
2.8 Radial density profile in ICP's 25
2.9 Resonance surface neutralization. 27
2.10 Auger neutralization and de-excitation processes 28
2.11 Neutral stream source schematic 32
2.12 Neutral stream source photo 33

3.1 Vacuum system modeled geometry 37
3.2 Equivalent process chamber geometry for VSTS simulation 41
3.3 Transmission probabilities for VSTS simulation 44
3.4 VSTS model components 46
3.5 Ideal pulsed pressure behavior of VSTS model 47
3.6 Test VSTS simulation 48
3.7 VSTS simulation with reduced flow rate and conductance 50
3.8 Alternate pump placement for VSTS 51
3.9 VSTS results with alternate pump placement 52
3.10 Mean free path variation with atom energy 55
3.11 3-D ray trace results for (a) 45° and (b) 55° 56
3.12 3-D ray trace results for (a) n = 1.0 and (b) n = 2.1 57

Reproduced with permission of the copyright owner. Further reproduction prohibited without permission.

3.13 Plasma density profile variation in 3-D ray trace model 59
3.14 Pressure effects on reflected neutral flux 60
3.15 2-D multi-source geometry 61
3.16 2-D shaped reflector schematic 63
3.17 2-D results for 3 plasma sources with same density 66
3.18 2-D results for 3 sources with varying densities 68
3.19 2-D simulation results for multi-facet plate with single plasma source 69
3.20 Combination of multi-source and multi-facet simulation 71
3.21 Seven source, single facet reflector simulation 73
3.22 2-D simulation with stair step shape and multiple densities 74
3.23 Positions on wafer for 2-D determination of angular distributions 75
3.24 Angular distributions from 2-D simulation of Fig. 3.18 76
3.25 Angular distributions from 2-D simulation of Fig. 3.22(c) 78
3.26 Angular distributions for multi-faceted reflector case of Fig. 3.19(b) 79
3.27 Possible 3-D configurations for multiple plasma sources 81

4.1 Geometry used for 3-D Monte Carlo simulation 83
4.2 Cosine emission distributions 86
4.3 Energy distributions as launched from the reflector plate 88
4.4 Flowchart of Monte Carlo simulation 92
4.5 3-D wafer flux maps vs. reflector angle from Monte Carlo simulation 96
4.6 Angular distributions from Monte Carlo simulation 97
4.7 Energy averaged θ' vs. reflector angle 98
4.8 Pressure effects on neutral flux 100
4.9 Normalized energy distributions 102
4.10 Average energy vs. wafer position vs. pressure 103
4.11 Average energy vs. reflector bias 105
4.12 Position dependence of neutral flux 107
4.13 Effect of wafer position on angular distributions 108
4.14 Etch yields for hyperthermal oxygen neutrals on Kapton 109
4.15 Etch rate of Kapton vs. pressure 111

5.1 General I-V characteristic for Langmuir single probe 115
5.2 Laframboise plot 119
5.3 Langmuir probe circuit 120
5.4 Measured radial plasma density profiles 123
5.5 I-V curves at reflector plate 124
5.6 Ion flux vs. power and pressure at reflector plate 126

Reproduced with permission of the copyright owner. Further reproduction prohibited without permission.

5.7 Axial magnetic confinement results 127
5.8 Ion current repeller for sample position 131
5.9 I-V curves for sample position 133

6.1 Alternate neutral stream source design 140

A.1 Schematic view of I-PVD apparatus 146
A.2 Trench fill profiles 148
A.3 Step coverage vs. ICP power 150
A.4 Step coverage vs. magnetron power 151
A.5 Wafer bias current vs. magnetron power 152
A.6 Wafer bias current vs. ICP power 154
A.7 Copper deposition rates 155
A.8 Ion density ratios 158

Reproduced with permission of the copyright owner. Further reproduction prohibited without permission.

Abstract

A novel source of hyperthermal (1 - 30 eV) reactive neutrals based on the surface-reflection-neutralization technique is described. This source is potentially capable of minimizing the charge-induced damage associated with plasma based semiconductor processing steps. The goal of this thesis is to investigate the issues involved in scale-up of this technology for processing of 8" diameter wafers used today in the semiconductor industry. This includes modeling the plasma ion source and trajectory simulations of the reflected neutral flux. A prototype source was constructed for experimental verification of the plasma model.

An inductively coupled plasma (ICP) source is used to provide a source of reactive ions. The ions are neutralized and reflected through interaction with a biased metal plate. These reflected neutrals are directed at a wafer to be etched (for feature delineation) or cleaned (removal of etch residue).

The plasma source is modeled with a global (volume averaged) power deposition model to determine plasma densities at the reflector plate. The modeled values are compared to measurements of a prototype neutral stream source. Plasma parameter measurements are carried out using Langmuir single probes. It is found that the plasma densities in the upstream plasma source and at the reflector plate agree well (within 10%) with the model.

Several models of reflected neutral trajectories are used to determine the final flux characteristics at the wafer. 2-D and 3-D ray trace models were first used to understand pressure effects on flux and angular distributions. The 2-D model was also used to model these characteristics for various plasma source configurations and reflector plate shapes. A full 3-D Monte Carlo simulation was used to explore reflected neutral energy and angular distributions at the wafer. 3-D flux maps at the wafer are also determined to understand flux uniformity. It is found that in the geometry considered in this work, background pressure plays a key role in delivering hyperthermal neutrals to the wafer. Energy and angular distributions are altered severely as the neutrals traverse the background gas and plasma. The results from these models have suggested a number of improvements which can be incorporated in the next-generation prototype neutral stream source.

Reproduced with permission of the copyright owner. Further reproduction prohibited without permission.

SURFACE REFLECTION HYPERTHERMAL

NEUTRAL STREAM SOURCE

Reproduced with permission of the copyright owner. Further reproduction prohibited without permission.

Chapter 1

Introduction

1.1 Neutral Stream Processing

Present semiconductor production, at feature sizes of 0.35 μ (16 Mbit), requires advanced forms of plasma processing tools. Research on equipment and process development is currently underway for the production of features with linewidths of 0.25 μ (256 Mbit DRAM), with continuation toward production of linewidths of $\leq$0.18 μ (1 Gbit) envisioned for the turn of the century. The number of layers required to build devices is expected to increase, while the thickness of certain individual layers, particularly dielectric layers, is expected to decrease dramatically [1]. To date, plasma etch technologies have produced adequate yield (successful chip fabrication rate). But as the critical dimension (CD) of features decrease, devices become more susceptible to damage due to wafer charging and uv bombardment during plasma processing, leading to a significant decrease in yield. This thesis describes a technology potentially capable of device fabrication at a rate suitable for semiconductor processing, while minimizing or eliminating the charge-induced damage associated with plasma-based etch steps.

The key to producing today's features has been the uniform ion bombardment at relatively low energies over a 200 mm diameter wafer, and a high flux of reacting species for adequate processing rates. Most chemical reactions have activation barriers less than

Reproduced with permission of the copyright owner. Further reproduction prohibited without permission.

10 eV. Indeed, many reactions have activation barriers below 1 to 2 eV [2]. Many solid lattices begin to show some form of nuclear displacement damage [3] (sputtering, dislocations, voids, etc.) at impingement energies of 20 to 30 eV. Some damage may appear at even lower impingement energies. Thus one wishes to provide a highly directional, high flux of reactants, with activation energies tunable between 1 and 20 eV, adequate to promote chemical processes, but below the threshold for lattice damage. Improvements in plasma sources, along with better means to measure low-energy ion and neutral atom distributions, certainly will be necessary to provide a portion of this capability.

However, recent work indicates that there may be problems inherent in the impingement of charged particles on wafer features. These include charge trapping and current stress on thin gate oxides [4, 5] which may occur even in highly uniform plasma reactors providing relatively low energy ion bombardment. X-ray and UV photon bombardment from plasmas are a known source of damage [6], which though annealable [7], may lead to long-term reliability problems with devices [4]. There have also been studies [8] indicating that lowering the ion energies in plasmas yield deflection of ion trajectories within features causing loss of profile control. Thus directed streams of neutral particles will play an important role in future processing.

The source described in this work is based on the surface reflection neutralization technique [9]. This method has been shown to be promising for fine-line, low-damage processing of semiconductors [7]. Ions are created in an upstream (downstream refers to the wafer processing region) plasma and flow along collimating magnetic field lines to a biased metal plate, called the reflector in this work. The downstream ions fall across a thin plasma sheath and are neutralized via electron tunneling from the metal reflector within a few angstroms of the surface [10]. The newly formed neutrals then reflect with a $\cos^n(\theta)$ angular distribution and an average energy approximately 1/2 to 1/3 of the reflector bias [11]. These hyperthermal (1 to 20 eV) neutrals then become incident on the wafer.

However, previous work with this technique was not suitable for large-scale ($\geq$ 8″

Reproduced with permission of the copyright owner. Further reproduction prohibited without permission.

diam.) wafer processing due to the small extent of the source ($\leq$ 2″ diam.) [7], although the results were promising. The primary output of this work will be evaluation of issues relevant to scale-up of the process to produce a high-flux, wide-area neutral stream for the charge-free processing of semiconductors on $\geq$ 8″ diameter wafers. Another important aspect of the work will be to determine the extent to which low energy charged particle processing affects the semiconductor product by directing hyperthermal reactive neutral atoms to the wafer.

The source will utilize the high-density, low-pressure inductively coupled plasma (ICP), or radio-frequency inductively coupled plasma (RFI), to provide reactive ions for neutralization. A schematic of a typical RFI source appears in Fig. 1.1. Rf current (13.56 MHz) is supplied to the planar spiral coil, facilitating power coupling to the electrons in the plasma via Faraday's Law. The neutral source will rely on the high uniformity and high ion density of the RFI to provide a uniform and intense neutral stream.

The present generation of capacitively coupled processing sources are operated to provide a degree of ionization of 10^{-6} to 10^{-4}, compared to 1 to 5% for an inductively coupled source. The degree of ionization (or dissociation of diatomic or polyatomic feedstock gases) can be increased in capacitively coupled sources by increasing the power, lowering the neutral pressure, or improving the confinement to raise the electron temperature. Unfortunately, this has a number of undesirable effects, including increasing the sheath potential at the wafer leading to higher ion bombardment velocities, resulting in greater damage to the wafer. Conversely, attempts to lower damage by lowering the sheath voltage, i.e., lowering power or increasing pressure, adversely affect process rate, uniformity, and anisotropy.

Due to the drawbacks associated with current capacitively coupled plasma sources described here, the industry is moving towards the RFI source for etching and plasma-enhanced-chemical-vapor-deposition (PECVD). The RFI source allows lower pressure operation due to more efficient coupling of power to the electrons as well as a very localized ionization region. Because the source is electrode-less (power is coupled through a dielectric window), lower plasma potentials are obtainable, decreasing the ion energies at the wafer by an order of

Reproduced with permission of the copyright owner. Further reproduction prohibited without permission.

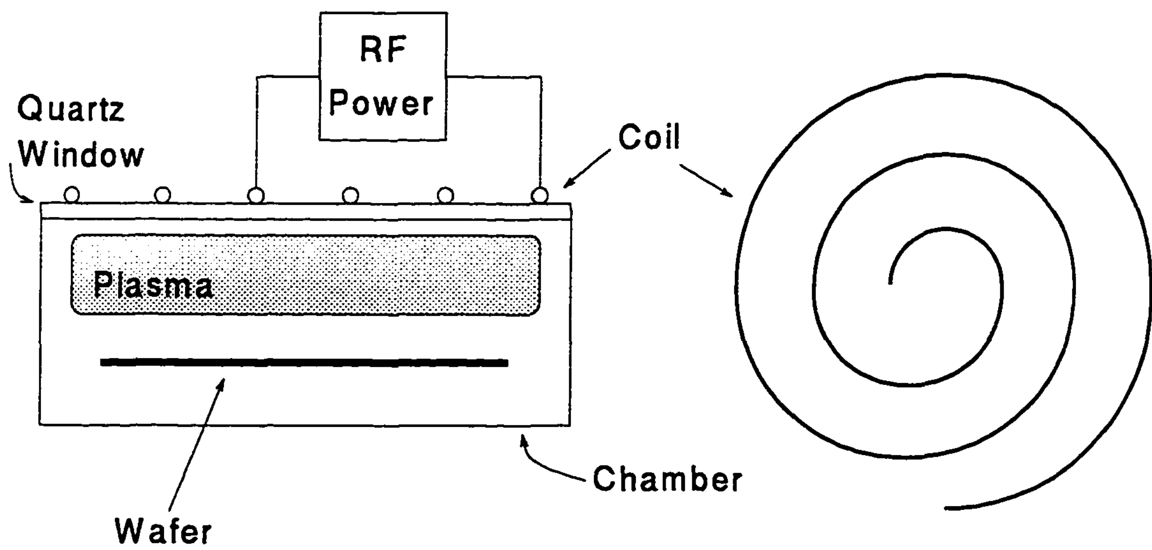

Figure 1.1: Typical ICP plasma source configuration.

Reproduced with permission of the copyright owner. Further reproduction prohibited without permission.

magnitude. Consequently, ion energies can be controlled via bias voltage at the wafer, which is generally not possible in a capacitively coupled plasma scheme.

The ion energy control allowed by the RFI is the key to controlling the final energy of the hyperthermal neutrals. As discussed later in this work, the production of high directed fluxes at very low impingement energies (1 to 5 eV) is beyond the current state of the art. However, the surface reflection neutralization scheme allows a wide range of control because the neutrals generally reflect with a kinetic energy of approximately 1/2 to 1/3 of the bias on the reflector plate.

In the sections that follow, a brief review of some of the issues relevant to the proposed work will be given. This will include a discussion of the charge-induced damage mechanisms for current ion-based etch schemes to motivate the need for such a source of neutrals as described here.

1.2 Devices and Charge-Induced Damage

A cross-sectional diagram of a simple MOSFET device appears in Fig. 1.2. In this diagram, n-doped silicon is the substrate . Ion-implantation or drive-in diffusion is used to create p-doped regions to fabricate the drain and source of the transistor. A thick insulating field oxide (FOX) is grown as a barrier to prevent inversion layer formation and cross-talk between devices. Conductive polycrystalline silicon (Poly-Si) is stacked on a thin insulating oxide layer. This gate oxide (GOX) contacts the n-doped silicon between the drain and source. As a negative voltage (with respect to the applied body voltage) is applied to the gate, an inversion layer forms just below the GOX that acts as a current channel between the drain and source. This behavior is the same as usually seen in macroscopic MOSFET devices. A variety of characteristics are attainable by changing the doping scheme.

Fig. 1.3 shows a highly simplified flowchart of the steps required to create such a device. The steps are general and apply to a variety of features. In Fig. 1.3(a), the various films necessary are deposited. The photoresist (PR) is patterned with optical lithography,

Reproduced with permission of the copyright owner. Further reproduction prohibited without permission.

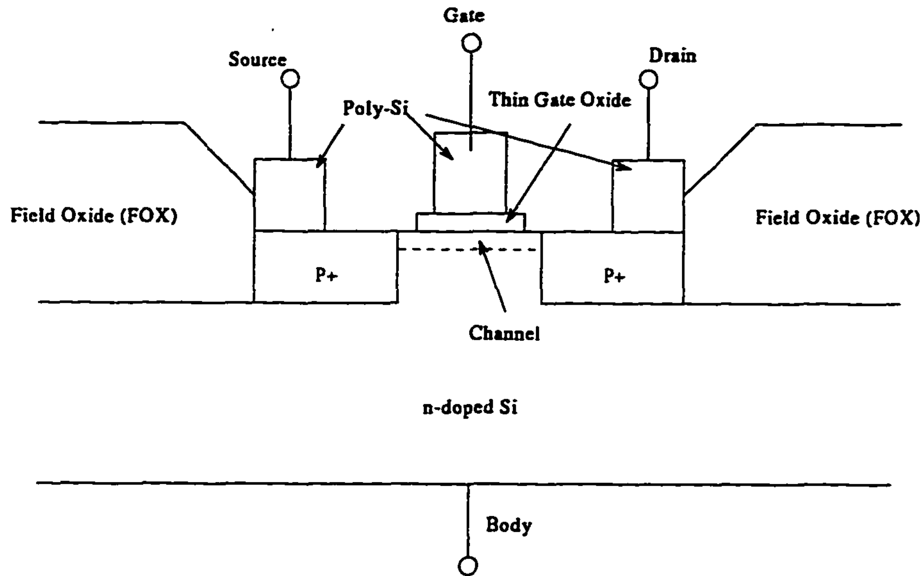

Figure 1.2: Cross-sectional diagram of typical MOSFET structure.

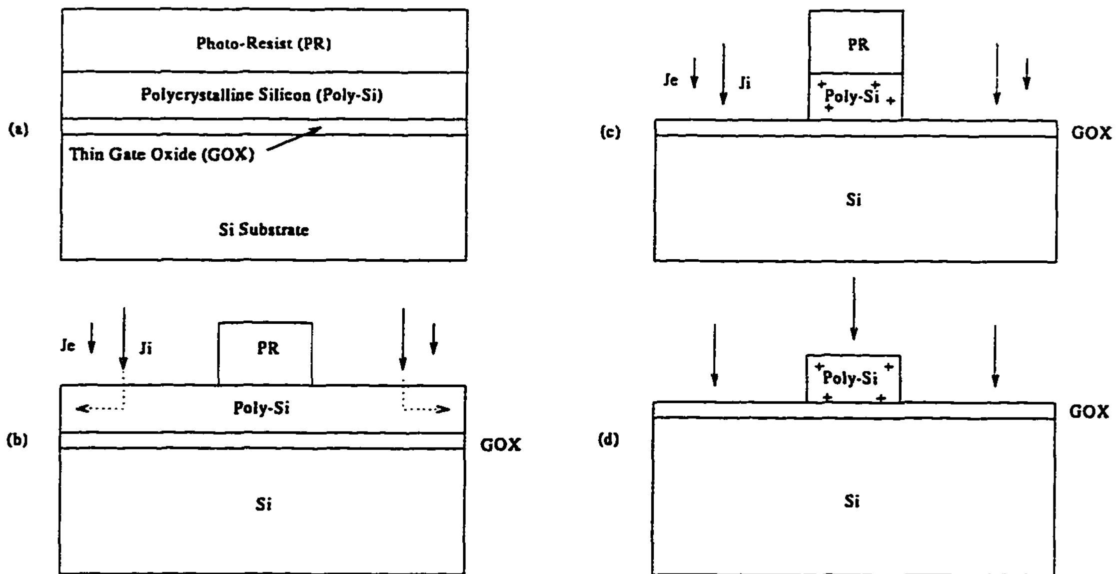

Figure 1.3: General progression of feature definition steps using plasma based etch techniques. The non-uniformity of the plasma potential across the wafer causes local imbalance of electron and ion currents, which leads to charging of insulated features.

Reproduced with permission of the copyright owner. Further reproduction prohibited without permission.

then "developed" via reactive ion etch (RIE), usually plasma based. For example, for the Poly-Si film shown here, a fluorine based chemistry is used to selectively etch the film over the photoresist. Molecular precursors of CF_4 and SF_6 mixed with O_2 are used as a source of reactive fluorine atoms. In addition, F-atom etching of Si is largely chemical based, as opposed to being driven by energetic ion bombardment, because of the high reactivity and volatility (high vapor pressure) of the products at room temperature.

For a perfectly uniform plasma, that is, one that varies little in density or plasma potential over the scale of the wafer, ion and electron currents must balance over one rf cycle. However, for a non-uniform plasma, while the global ion and electron currents balance, the local current densities need not balance. For a region of plasma with a high plasma potential, ion currents will be higher than that of electrons. Conversely, for the lower plasma potentials, electron currents will dominate. For a discussion of plasma physics and terms, see Chapter 2.

This current imbalance leads to charging of isolated conductors on the wafer surface. As seen in Fig. 1.3, when the Poly-Si etch step nears endpoint, the film becomes discontinuous, leaving no current paths to bleed off excess charge. This charge buildup leads to an ever increasing voltage. The polarity of this potential depends on the majority current flux species. The charge-induced potential build-up will continue until the local current densities balance, or the oxide begins to conduct [5].

The oxide begins to conduct at low voltage due to Fowler-Nordheim tunneling [4, 5]. This tunneling current leads to small stresses in the oxide that reduce the lifetime and reliability of the device. Fowler-Nordheim tunneling tends to occur at weaker regions of the gate oxide. This weakness may be caused by defects in the oxide, or may occur in locally thinner regions.

Fowler-Nordheim tunneling currents for a 10 nm thick gate oxide can be small, on the order of nA to μA, for induced biases of near 10 Volts [4]. While this does not by itself constitute catastrophic breakdown of the oxide, the associated current stress can lead to

Reproduced with permission of the copyright owner. Further reproduction prohibited without permission.

reduced device lifetime. Energetic ions and electrons can be trapped in the insulating oxide layer. These trapped charges promote modification of device thresholds as well as increased current flow across the oxide layer. 3.3 volts is the operating voltage in the current generation of devices, although this will decrease to $\approx$ 1.8 volts by the turn of the century, then down to $\approx$ 0.9 volts by the year 2010 [1] as oxide thickness is correspondingly reduced.

It is this charge-induced damage that we seek to reduce by removing the charge activated (acceleration of ions) reaction scheme, and replacing it with energetic neutral bombardment providing sufficient energy to promote wafer surface reactions.

1.3 Organization of this Thesis

The goal of the work will be to ascertain the etching and cleaning performance of this source. This will be accomplished by the following:

- Model the plasma ion source density profile of the ICP to understand its suitability as a neutral precursor source
- Characterize the operation of the ICP plasma as an upstream source by direct in-situ measurement of ion densities
- Compare the characteristics of the plasma source to the plasma model
- Simulate reflected neutral trajectories to predict flux and angular distributions at the wafer position based on the modeled plasma density profile
- Compare etch rates at the wafer to that predicted by the Monte Carlo simulation.

Chapter 2 of this work will describe the plasma physics relevant to processing of materials. Surface reflection and neutralization of ions incident on metal surfaces is also discussed. This includes the fundamental measurements of reflection parameters from previous work used in the modeling. Finally, a detailed description of the neutral stream apparatus developed for this work is presented.

Reproduced with permission of the copyright owner. Further reproduction prohibited without permission.

In Chapter 3, the modeling of this source will be discussed. This includes a 2-d and 3-d ray tracing model useful for estimating total fluxes and flux uniformity at the wafer following reflection from the biased metal plate. An analysis of vacuum system requirements is presented based on the Vacuum System Transient Simulator (VSTS) package from the Department of Energy.

A full 3-d Monte Carlo simulation of reflected neutral trajectories which considers elastic, inelastic and charge-exchange collisions is presented in Chapter 4. This model is particularly useful as it predicts reflected neutral energy and angular distributions at the wafer from input plasma and pressure parameters. That is, the Monte Carlo model simulates the entire neutral stream source from upstream plasma to the wafer parameters.

Chapter 5 shows the results from the experimental phase of the project. Langmuir probe measurements of the plasma source are presented. Densities profiles and ion flux to the reflector plate are compared to simulation results. Measurements of the charge reaching the wafer are also presented to show the possible damage reduction obtained by this source.

The description of this project and results concludes in Chapter 6 with a discussion of the results and their possible bearing on a production worthy neutral stream source. Further, a discussion of future directions in surface-reflection based neutral stream processing is presented, including outlines of possible improvements in design based on this work.

Appendix A presents a paper submitted and accepted for publication by the Journal of Vacuum Science and Technology. This paper describes work completed by the author and co-workers at IBM during a summer internship. This work involves the deposition of copper ionized by an ICP plasma source to improve directionality of damascene (embedded features) trenches and vias.

Reproduced with permission of the copyright owner. Further reproduction prohibited without permission.

Chapter 2

Theory of Operation

In this chapter, the relevant physics of the surface-reflection neutral stream source is discussed. This includes a discussion of the plasma state as it applies to processing of materials. A simple power deposition model for the plasma source will be presented. The general surface reflection neutralization mechanisms will also be discussed. Macroscopic measurements of the neutralization process as it applies to the design and scale-up of the source will be reviewed.

2.1 Plasma Concepts

In general, a plasma can be described as a gas composed of neutral (atomic or molecular) species, electrons and ions. On average, the plasma is electrically neutral, i. e. , the density of ions (n_i) and the density of electrons (n_e) are equal. This phenomena is referred to as "quasi-neutrality". For the plasmas of interest to the materials processing community, the fractional ionization defined by $\chi_i = \frac{n_i}{n_g+n_i}$ [12], where n_g is the neutral gas density, is small (approximately 1 to 5% for high density plasma sources). Further, the electrons are not in thermal equilibrium with the ions, neutrals, or the surrounding discharge chamber walls. This is due primarily to the fact that the electrons, by virtue of their smaller mass, are much more mobile than the ions. Thus the electrons are preferentially heated by the applied electric

Reproduced with permission of the copyright owner. Further reproduction prohibited without permission.

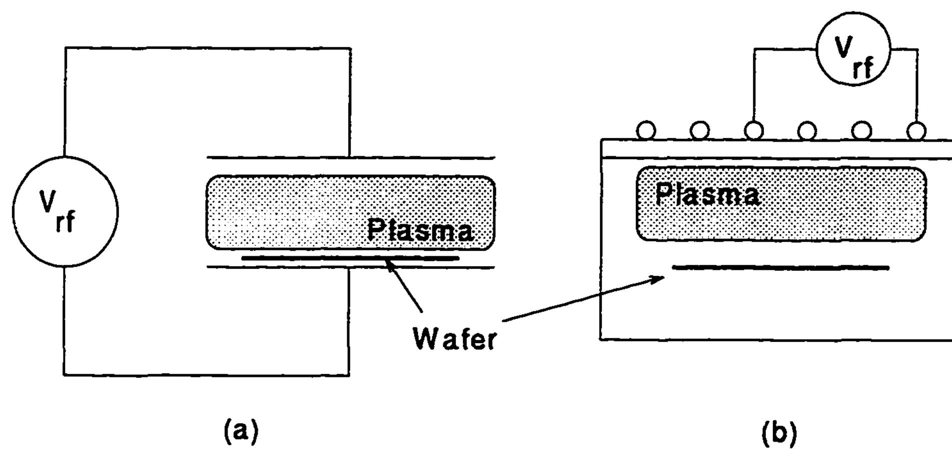

Figure 2.1: General plasma source configurations. (a) Capacitively coupled source: the potential applied between the two plates of the capacitor is the applied electric field. (b) Inductively coupled plasma (ICP) source: a high frequency current in the coil induces an azimuthal electric field, driving the plasma.

Reproduced with permission of the copyright owner. Further reproduction prohibited without permission.

field. The ions also exchange energy efficiently the the background gas through elastic and inelastic collisions. The net effect is that the electrons, ions, and neutrals of the discharge can be described by different temperatures, namely $T_e >> T_i \approx T_g$, where the subscripts e, i, and g refer to the electrons, ions and neutral background, respectively.

The discharge is driven by an applied electric field. General representations of plasma sources appear in Fig. 2.1. In Fig. 2.1(a), a capacitively coupled plasma source is shown. Here the driving electric field is applied between the plates of the capacitor where the plasma forms. In Fig. 2.1(b), an inductively coupled plasma (ICP) source in a flat spiral configuration is shown. A spiral coil is placed just above the discharge chamber on a dielectric (usually quartz) window. For the ICP, a high frequency current is applied to the spiral coil. This current induces an electric field via Faraday's law, which drives the plasma.

Although it is not true of all discharges, the energy distribution of the electrons can be approximately described by the Maxwellian distribution, shown in Fig. 2.2. We note that for the low-temperature (T_e < 10 eV) plasmas under consideration, the energies for molecular dissociation (ϵ_{dis}) and ionization (ϵ_{ion}) are generally higher than the bulk electron temperature. Thus, the bulk of the electrons play little role in dissociation and ionization, rather, it is the electrons of the high-energy "tail" that contribute most to these processes.

However, ionization and dissociation can proceed "stepwise", i. e. , electrons can bombard an atom (molecule) faster than the subsequent excited species can de-excite, such that multiple collisions lead to ionization (dissociation). This stepwise process, while important, is usually ignored when modeling plasma discharges. Instead, an "average" value for the required energy is used based on energy cost in creating a particular species. In fact, this is done in the plasma model presented in Chapter 3.

2.1.1 Sheaths

One of the most important concepts in the discussion of plasmas as they relate to materials processing is the "sheath". The sheath is a thin positively charged layer adjacent

Reproduced with permission of the copyright owner. Further reproduction prohibited without permission.

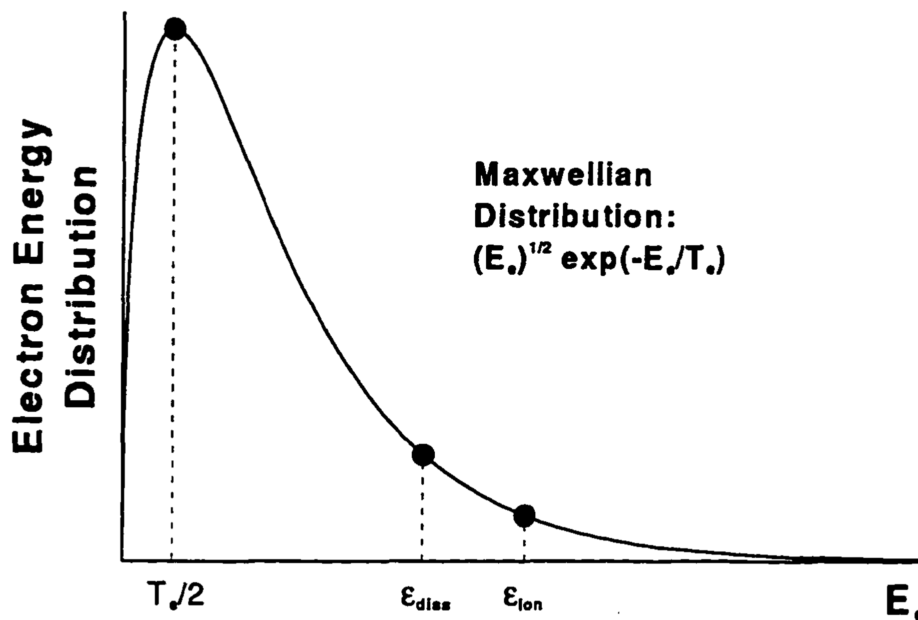

Figure 2.2: Maxwellian energy distribution for the plasma electrons. Note the position of the molecular dissociation energies, ϵ_{diss}, and ionization energies, ϵ_{ion}, with respect to the electron temperature, T_e.

Reproduced with permission of the copyright owner. Further reproduction prohibited without permission.

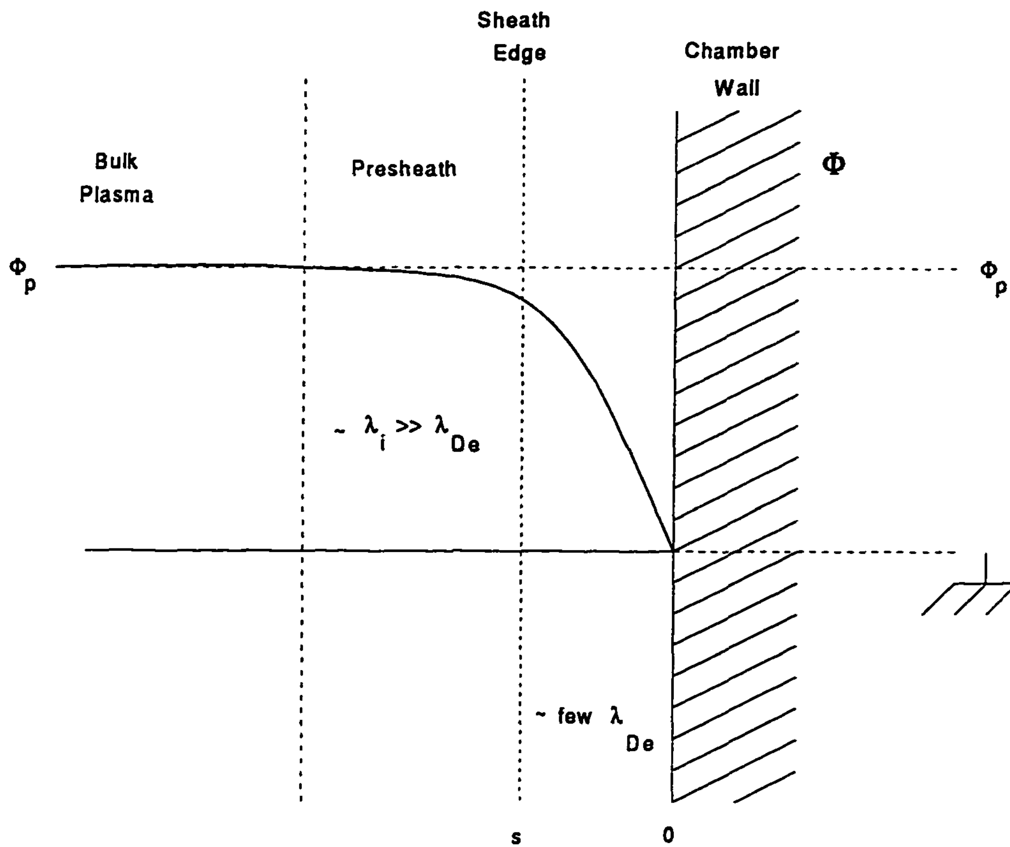

Figure 2.3: Generalized sheath formation. A thin, positively charged layer (see Fig. 2.4) forms near the chamber walls which acts as a potential barrier to electrons. Ions traversing the sheath have a kinetic energy approximately equal to eV_p.

Reproduced with permission of the copyright owner. Further reproduction prohibited without permission.

to all surfaces in contact with the plasma. Consider the relative thermal velocities of electrons, $V_{th_e} = (T_e/m_e)^{1/2}$, and ions ($V_{th_i} = (T_i/m_i)^{1/2}$) where the temperatures are given in units of electron volts (eV). We find the electron velocity to be 100's of times that of the ions, due to their higher temperature and lower mass. For a quasi-neutral plasma, the electric field, E, and the electric potential, Φ, would be zero everywhere, and the electrons would quickly be lost to the walls, extinguishing the plasma.

However, the situation appearing in Fig. 2.3 arises where the electrons near the wall are lost quickly, leaving behind a thin region rich in positively charged ions ($n_i >> n_e$) as shown in Fig. 2.4. The net positive charge density in the sheath leads to a potential profile that is positive (with respect to the walls) in the bulk of the plasma, and falls off quickly to the wall potential, normally ground. The electric field is directed from the plasma to the walls, so the net force on the electrons is into the plasma, and out of the plasma for ions. Thus the plasma potential (bulk plasma electric potential) comes to an equilibrium value such that the net loss from the plasma of the charged species (electrons and ions) is balanced with the creation of charged species via applied power.

When ions reach the sheath edge by diffusion or a potential gradient in the plasma, they are accelerated across the sheath of width s by the potential drop, V_p, where V_p is the positive plasma potential. The plasma potential is dependent on a number of factors including source geometry, pressure and method of plasma creation. For a capacitively coupled plasma, the potential can be very high, $V_p \approx 200$ Volts. So ions traversing the sheath will strike the wall or wafer with 200 eV of kinetic energy. However, for an ICP, we find that the plasma potential is on the order of 15 to 20 Volts.

The differences in plasma potential between the ICP and capacitively coupled cases arises from the method of coupling. In general, the plasma potential must rise at least a few volts higher than the most positively biased object in the discharge chamber. For capacitive coupling, the electrodes are in direct contact with the plasma. These electrodes can have on the order of 100's of volts on them during most of the rf cycle. Because the ions are much less

Reproduced with permission of the copyright owner. Further reproduction prohibited without permission.

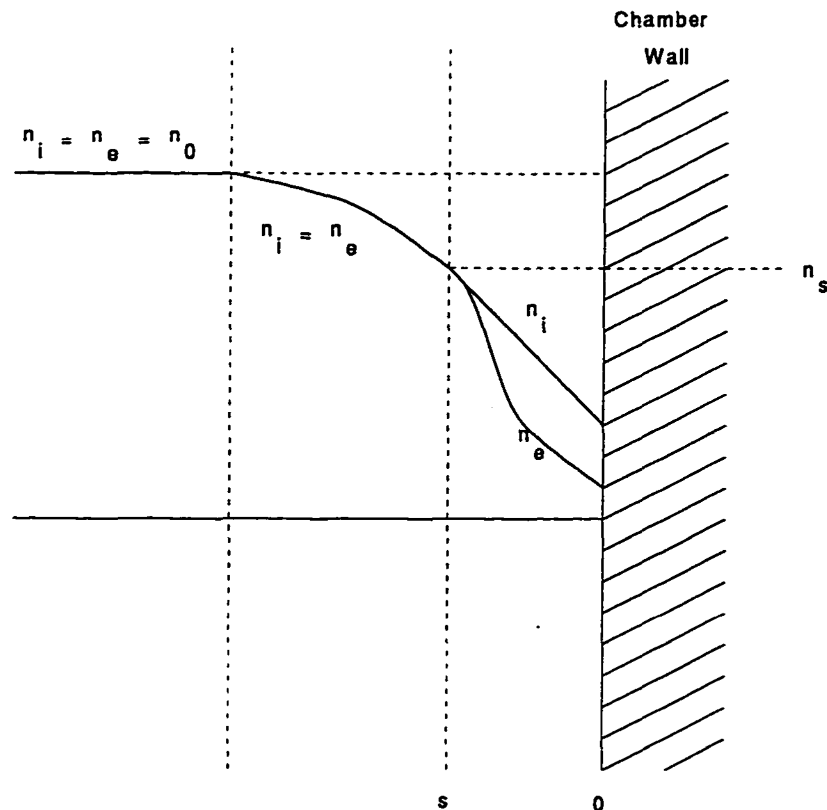

Figure 2.4: Generalized sheath density profiles for ions and electrons. Note that in the bulk plasma, the quasi-neutrality condition holds. At approximately λ_i (ion mean free path) from the chamber wall, in the presheath, the plasma density begins to fall from its bulk plasma value, but remains quasi-neutral. In the sheath, the densities of the ions and electrons begin to diverge such that the ion (positive) density is larger than the electron density.

Reproduced with permission of the copyright owner. Further reproduction prohibited without permission.

mobile than the electrons, the plasma potential is largely driven by the ion density. Thus, the plasma potential will also be on the order of 100's of volts. The time-averaged plasma potential compared to the driving electrode voltage depends on the type of gas used. Highly electronegative gases tend to track the voltage because they are a sink for electrons (e. g. , Cl_2) such that the discharge actually extinguishes during the rf cycle. For a grounded wafer chuck, the ion energy can be very high at the wafer, resulting in physical damage to the wafer. Similarly, sputtering from the grounded chamber walls can contaminate the wafer.

ICP power is coupled through a dielectric window, that is, no electrode is in contact with the plasma. There is still several hundred volts on the rf coil which can result in sputtering of the dielectric window, however, this can be minimized by the introduction of a "Faraday" shield which shorts radial and longitudinal electric fields. A Faraday shield was not used in this work, however.

2.1.2 Creation of Plasma Species

As mentioned above, electron impact on atoms and molecules in the plasma is responsible for creation of ions and dissociated reactive species. For a mono-atomic feedstock gas (Ar)

$$e^- + Ar \rightarrow Ar^+ + 2e^- \quad \text{Ionization} \tag{2.1}$$

$$e^- + Ar \rightarrow Ar^* + e^- \quad \text{Excitation} \tag{2.2}$$

are the important electron impact processes in the plasma. The first ionization potential (IP) for argon is 15.76 eV. There are several excited states for argon, but the energy lost per excitation collision can be modeled as an average process as noted above. The rate functions for these processes can be fit to exponential forms [13]:

$$k_{\text{ion}} = 1.23 \times 10^{-7} \exp(-18.68/T_e)[\text{cm}^3\text{s}^{-1}] \tag{2.3}$$

$$k_{\text{exc}} = 3.71 \times 10^{-8} \exp(-15.06/T_e)[\text{cm}^3\text{s}^{-1}] \tag{2.4}$$

Reproduced with permission of the copyright owner. Further reproduction prohibited without permission.

where $k_{ion} = <\sigma_{ion}(E)v(E)>$ is the first order rate coefficient for ionization, $\sigma_{ion}(E)$ is the energy-dependent ionization cross-section, and v(E) is the velocity of the electron of energy E. The brackets <> refer to averaging with respect to energy. The parameter k_{exc} is similarly defined for excitation.

For molecular species, such as O_2, in addition to the above processes, dissociation of the molecular species

$$e^- + O_2 \rightarrow O + O + e^- \tag{2.5}$$

is another important electron impact process. A rate coefficient function can also be defined for this process. Direct ionization and excitation of the molecular species, as well as the same processes for dissociation products, can occur.

Let's consider the example of an argon high-density (ICP) discharge. The ultimate electron temperature and charged particle densities are determined by a number of factors, namely, geometry, power applied, and pressure. Geometry effects usually are parameters such as radius and length of the discharge chamber, and total volume. Radius and length are important because they determine the distance over which ionic species must diffuse before reaching the chamber walls, possibly to be lost by recombination. Total volume comes into play when recombination in the gas phase represents a large ion loss component. This is much less important at lower pressures ($\leq$ 10 mTorr) where the ion/neutral mean free paths are larger.

We used a particle and power balance model for the plasma source outlined in Chapter 3. This model uses the power input to the plasma volume and geometry of the system to solve for steady state charged particle densities and electron temperatures.

Godyak [14] showed that for unmagnetized plasmas at low pressures ($\lambda_{ion} \leq R, L$), the ratio of the edge plasma density (at R, L) to the bulk plasma density (in center of discharge)

Reproduced with permission of the copyright owner. Further reproduction prohibited without permission.

could be described by

$$h_R \equiv \frac{n_{s_R}}{n_o} \approx 0.8\left(4+\frac{R}{\lambda_i}\right)^{-\frac{1}{2}}$$
$$h_L \equiv \frac{n_{s_L}}{n_o} \approx 0.86\left(3+\frac{L}{2\lambda_i}\right)^{-\frac{1}{2}} \tag{2.6}$$

where n_{s_R} and n_{s_L} are the radial and longitudinal plasma edge densities, n_o is the bulk plasma density, and λ_i is the ion mean-free-path. The characteristic radius and length of the cylindrical chamber are denoted by R and L, respectively. The values for h_L and h_R usually present values in the range 0.3 to 0.5. We can then relate the total volume ionization to diffusive losses at the chamber walls by

$$n_o u_B(2\pi R^2 h_L + 2\pi RLh_R) = k_{\text{ion}} n_g n_o \pi R^2 L \tag{2.7}$$

where k_{ion} is the ionization rate coefficient, given above for argon, n_g is the neutral background density, and u_B is the Bohm ion sheath velocity, $u_B = (T_e/M_{\text{ion}})^{1/2}$. Eqn. 2.7 can be rewritten

$$\frac{k_{\text{ion}}(T_e)}{u_B(T_e)} = \frac{1}{n_g}\frac{2Rh_L + Lh_R}{RL} = \frac{1}{n_g d_{\text{eff}}} \tag{2.8}$$

which can be solved directly for electron temperature. The parameter d_{eff} is the effective plasma size. Note that the temperature is independent of input power.

In order to find the plasma density, we must know the values for electron and ion energy losses due to collisions with the walls and other species in the plasma. The total energy lost to the plasma per ion lost can be written $\epsilon_T = \epsilon_c + 2T_e + \epsilon_i$, where ϵ_i is the mean kinetic energy loss per ion lost at the sheath, ϵ_c is the energy loss per electron impact collision event, namely ionization and excitation. The mean kinetic energy lost per electron lost is $2T_e$. Determination of these energy loss values is straightforward in a single-ion system. Power balance is given by

$$P_{\text{abs}} = en_o u_B A\epsilon_T \tag{2.9}$$

where A is the surface area of the plasma chamber and P_{abs} is the absorbed power.

Reproduced with permission of the copyright owner. Further reproduction prohibited without permission.

The collisional energy loss for electrons can be defined per ion-electron pair created by

$$k_{\text{ion}}\epsilon_c = k_{\text{ion}}\epsilon_{\text{ion}} + k_{\text{exc}}\epsilon_{\text{exc}} + k_{\text{elastic}}\frac{3m_e}{M_{\text{ion}}}T_e \tag{2.10}$$

where the first term on the right hand side (RHS) is the ionization energy lost per ionization event, the second term is the excitation energy lost, and the third term is due to energy lost per background-neutral/electron elastic collision. The sheath potential drop is approximately given by $V_s = \frac{T_e}{2}\ln\left(\frac{M_{\text{ion}}}{2\pi m_e}\right)$. From the Bohm velocity given above, the initial kinetic energy of an ion entering the sheath is $T_e/2$. Thus the directed energy of an ion leaving the plasma via the sheath is $\epsilon_i = V_s + T_e/2$. For an argon discharge, this is $\approx 5.2T_e$.

Accounting for the fact that the density at the edge (sheath) is different than the bulk value, we can solve for the bulk density by

$$n_o = \frac{P_{\text{abs}}}{eu_B A_{\text{eff}}\epsilon_T} \tag{2.11}$$

where $A_{\text{eff}} = 2\pi R(Rh_L + Lh_R)$ is the effective chamber surface area.

From this model, we can obtain T_e and n_o for input values of power, pressure and geometry. This model is used as the front-end of the Monte Carlo trajectory simulation presented in Chapter 3. Modifications of the model for the specific geometry in this work will be discussed then.

2.1.3 Inductive Coupling

The radio-frequency (rf) current applied to the coil in the plasma source produces an oscillating magnetic field as seen by Faraday's law (in Gaussian units)

$$\nabla \times \mathbf{E} = -\frac{1}{c}\frac{\partial \mathbf{B}}{\partial t} \tag{2.12}$$

where $\mathbf{E}$ and $\mathbf{B}$ are the electric field and magnetic induction, respectively. It is clear that the time-varying magnetic flux density induces an azimuthal electric field which accelerates free electrons in the chamber to sustain the plasma.

Reproduced with permission of the copyright owner. Further reproduction prohibited without permission.

We assume a form for the induced magnetic field of

$$\mathbf{B}(r,\theta,z,t) = \mathbf{B}(r)e^{-\frac{z}{\delta}}e^{-i\omega t} \tag{2.13}$$

where δ is the plasma skin depth, $\delta = c/\omega_{pe}$, where c is the speed of light and $\omega_{pe} = (e^2 n_e/\epsilon m_e)^{1/2} = 9000\sqrt{n_e[cm^{-3}]}$[Hz] is the electron plasma frequency. Note that we assumed cylindrical symmetry, removing the θ dependence.

For the densities normally found in ICP's, $n_e \approx 1 \times 10^{12}$ cm^{-3}, the skin depth is approximately 3.3 cm. Because the plasma is overdense, $\omega_{pe} >> \omega_{rf}$ ($\omega_{pe} = 9000\sqrt{n_e} =$ 9 GHz, $\omega_{rf} =$ 13.56 MHz), electromagnetic waves do not propagate in the discharge, and electron heating is limited to a depth of approximately δ from the dielectric window. This effect is analogous to high frequency fields in proximity to metals where currents only flow in a thin layer on the surface of the metal.

Using Ampere's law and eqn. 2.13, one can find the azimuthal electric field from measurements of the magnetic field,

$$\mathbf{E} \simeq \hat{\phi}\frac{B_r(r)\exp(-z/\delta)}{i\omega\epsilon\mu_o\delta}. \tag{2.14}$$

This was done by Hopwood, et. al. [15]. A schematic representation of magnetic field measurements in ICP's appear in Fig. 2.5. The validity of the form of eqn. 2.13 was also tested by Hopwood. The dependence of the field on skin depth was verified.

We note from eqn. 2.14 that the electric field dependence is essentially that of the radial component of the B-field. From Fig. 2.5 we see the absorbed power density, $P_{abs} = 1/2Re(\tilde{J}_\theta \tilde{E}_\theta^*)$, vanishes on the axis and edges, creating a toroidal absorbed power profile. Electric field magnitudes of $100 - 200$ V/m have been found at the peak of the profile [15].

Hopwood, et. al. [16], and Barnes, et. al. [17], have determined the density, temperature and plasma potential trends in ICP's at low pressure. These trends appear schematically in Fig. 2.6. Note that the plasma potential becomes large as the pressure is decreased. This is to compensate for loss of charged-particles due to diffusion and free fall as the ion mean-free-path increases. T_e falls with pressure increase because electrons experience fewer

Reproduced with permission of the copyright owner. Further reproduction prohibited without permission.

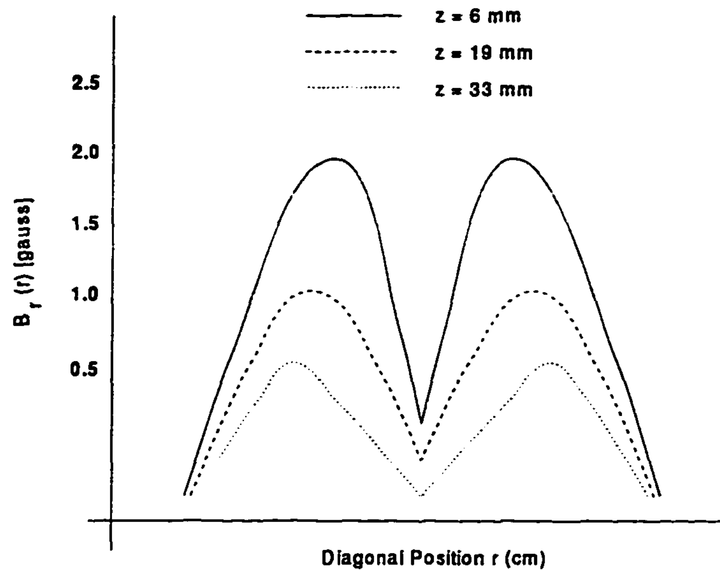

Figure 2.5: Measured magnetic field profiles [15] in an inductively coupled plasma sources at various distances below the dielectric window. These values represent the radial component of magnetic field, which is directly responsible for the azimuthal electric field heating the plasma.

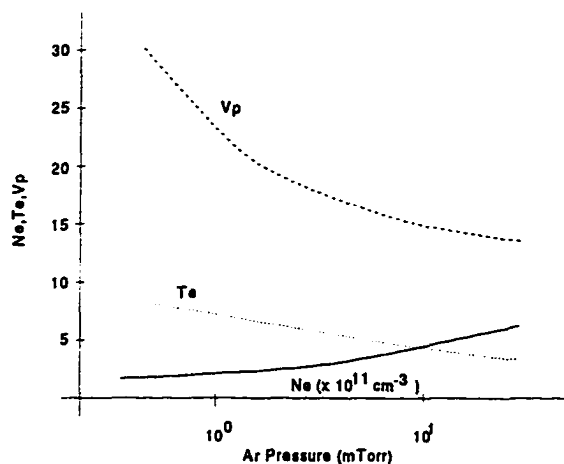

Figure 2.6: Hopwood, et. al. [16], and Barnes, et. al. [17], have determined the general behavior of ICP's at low pressure. Note that the plasma potential becomes large as the pressure is decreased. This is to compensate for loss of charged-particles due to diffusion and free fall as the mean-free-path increases. T_e falls with pressure increase because electrons experience fewer "cooling" collisions at lower pressure. Density increase with pressure is largely due to increased electron/background-gas collision frequency.

Reproduced with permission of the copyright owner. Further reproduction prohibited without permission.

"cooling" collisions at lower pressure. Density increase with pressure is largely due to increased electron/background-gas collision frequency. Similar trends are found for the ICP source of the surface-reflection neutralization source and are described in detail in Chapter 4.

The results obtained by Hopwood have important implications for the currently described neutral source. Recall that delivery of neutrals is dependent on two factors: plasma density and background pressure. The density must be high enough to create large fluxes of neutrals, but they must be unhindered as they traverse the background gas. While low pressure assures that a larger fraction of the reflected neutrals will survive to the wafer, the density of ions for neutralization falls as pressure decreases.

Another important parameter of interest is the plasma potential. At lower pressures, the plasma potential increases dramatically as we see in Fig. 2.6. This directly affects the energy of the ions that reach the reflector plate, and thus the energy of the reflected neutrals. Ion kinetic energies reaching the reflector plate are given by $E = e(V_p - V_{plate})$, where V_{plate} is the applied plate bias. While the ion kinetic energy at the plate shows little effect on the final etching characteristics of the reflected neutrals, uncontrollable high kinetic energies could lead to reflector plate sputtering which could contaminate the sample. However, these energies are still an order of magnitude smaller than those seen in capacitively coupled plasma sources.

In a general ICP, the plasma density is centrally peaked, as seen in Fig. 2.8. This profile is very poor when applied to an etch application where uniformity of etch rate across an 8″ wafer is important. However, the profile can be improved dramatically with the introduction of a magnetic-cusp confinement scheme. A ring of alternating north-south permanent magnets are placed around the discharge chamber, producing a field structure like that in Fig. 2.7. The magnetic field lines confine electrons near the edges of the discharge, increasing the probability of ionization at the edges. This increases the plasma density at the edges creating a more uniform density profile as seen in Fig. 2.8.

Reproduced with permission of the copyright owner. Further reproduction prohibited without permission.

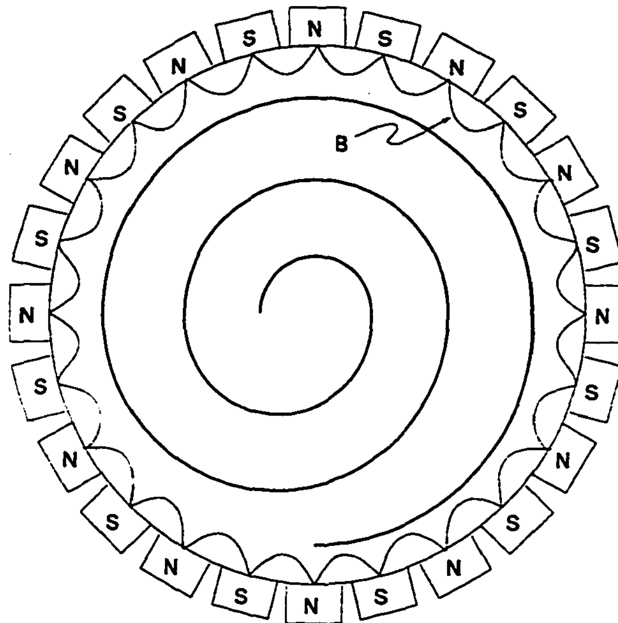

Figure 2.7: A ring of permanent magnets arrayed about the discharge chamber below the quartz window in an alternating N-S configuration can improve plasma density uniformity. The magnets generally have a surface-field on the order of 1 to 2 kG. The general placement of the ICP coil is shown.

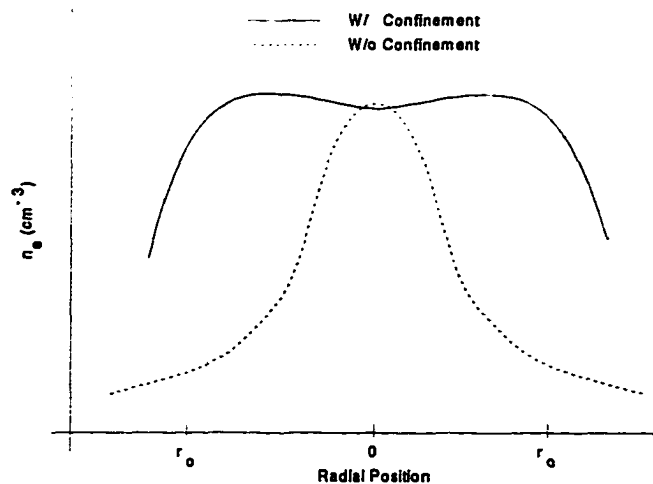

Figure 2.8: Magnetic multipole confinement greatly improves the radial uniformity of ICP reactors. Without multipole confinement, the density is strongly peaked in the center of the discharge. However, with magnetic confinement, the plasma density on the edges increases with respect to the center, improving overall density and uniformity.

Reproduced with permission of the copyright owner. Further reproduction prohibited without permission.

2.2 Surface Reflection

There are three channels by which an ion in proximity with a metal surface could be neutralized. They are radiative, resonance, and Auger neutralization. The first of these, where the neutralization energy is given off as a photon, is unlikely because the initial state lifetime is approximately 10^6 times longer than the other two processes [10].

Resonance neutralization occurs when a electron from below the Fermi level of the metal tunnels to an excited level of equal energy in the incoming ion. This process is illustrated in Fig. 2.9, appearing as transition 1. The opposite resonance process (resonance ionization) is also shown, where an electron from an excited neutral tunnels to an unfilled level above the Fermi level of the metal.

The importance of this process in neutralization depends on the relative ionization energy ($E_i^{\prime} - E_x^{\prime}$ defined in Fig. 2.9) of the excited state. Process "1" can only occur if the effective ionization energy is greater than the work function of the metal, ϕ. One can also note that the process cannot occur if the ionization energy of the excited state is less than $\epsilon_o = \epsilon_F + \phi$, the bottom of the conduction band relative to the vacuum level. Similarly, the opposite process ("2" in Fig. 2.9) may occur if this ionization energy is less than the work function.

Auger neutralization and de-excitation release the required energy through electron emission from the metal to the vacuum. These processes appear in Fig. 2.10. For Auger neutralization, an electron in the conduction band of the metal tunnels to the ground state of the incoming ion while a second electron is excited from another level, labelled "2" in Fig. 2.10(a). The energy lost in transition "1" is gained by the electron in transition "2". This energy could be high enough to expel the electron from the surface. In the de-excitation process, an excited state electron (labelled "1" in Fig. 2.10(b)) either falls to a ground state level or is ejected, while another electron (transition "2") performs the opposite transition.

The four processes described above (two resonance and two Auger) form a set of processes that are important for surface neutralization. If an incoming ion undergoes reson-

Reproduced with permission of the copyright owner. Further reproduction prohibited without permission.

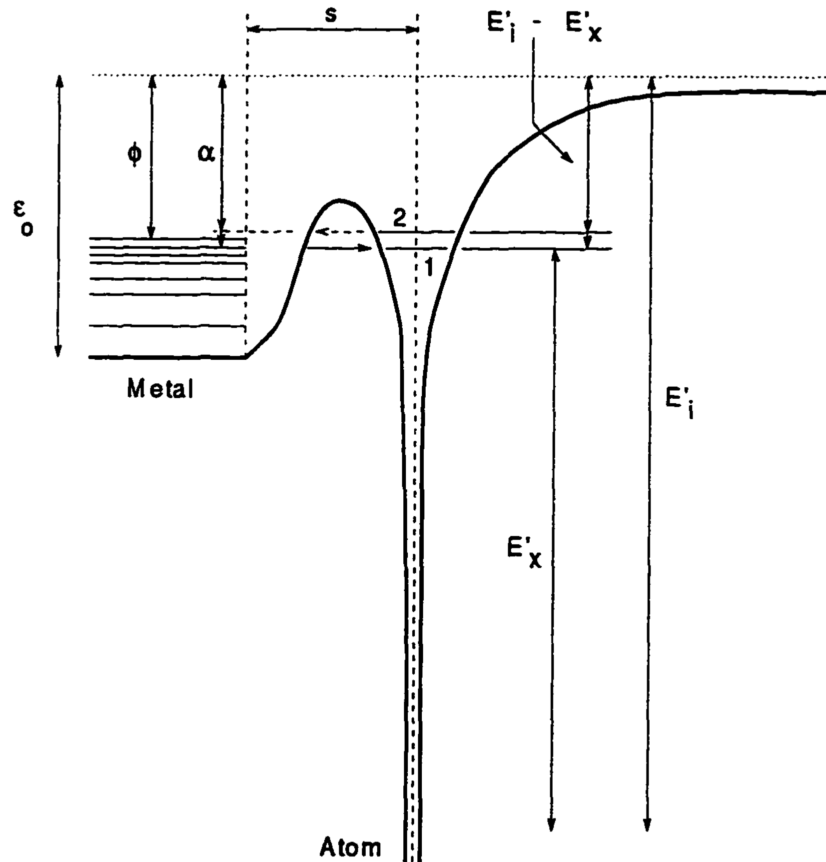

Figure 2.9: Resonance surface neutralization process. An electron from below the Fermi level of the metal tunnels to an excited level of the incoming ion (transition 1). The opposite occurs for an excited neutral, where an electron from the excited level tunnels to an unfilled level in the metal above the Fermi level. The work function of the metal is ϕ, and s is the atom/surface separation.

Reproduced with permission of the copyright owner. Further reproduction prohibited without permission.

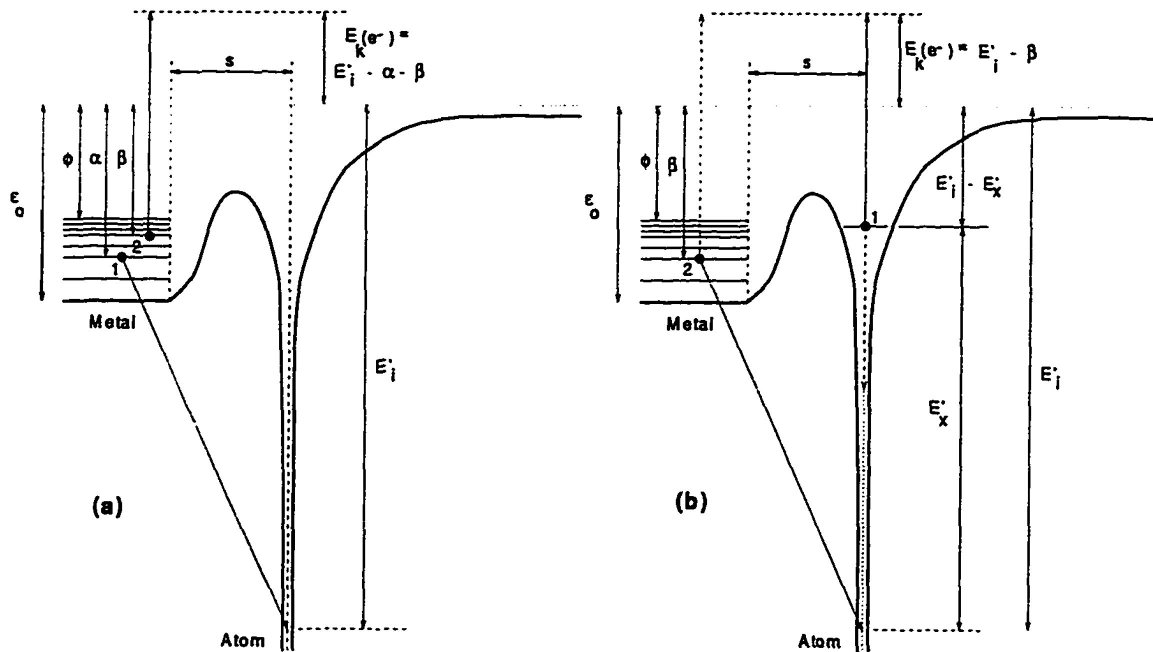

Figure 2.10: Auger neutralization and de-excitation processes. (a) An electron from the metal level labelled "1" tunnels to a ground state level of the incoming atom, while an electron from level "2" is excited to a higher level, or is ejected altogether. (b) For de-excitation, an electron in the excited state "1" either is ejected, or falls to the ground state, while an electron in the metal ("2") performs the opposite transition.

Reproduced with permission of the copyright owner. Further reproduction prohibited without permission.

ance neutralization, the system could be returned to its original state, if the energetics are right, via resonance ionization. An incoming ion could also undergo resonance neutralization to an excited state, then decay via Auger de-excitation. Further, there is the direct Auger neutralization process, which also results in electron emission. Two of the above processes result in neutralization with an accompanying electron emission. Thus, collection and analysis of the ejected electrons have been the focus of much research which has been reviewed by Hagstrum [10].

Probability functions can be defined for each process based on the position-dependent rate functions, $R_t(s)$, where s is the atom/surface separation distance. If one assumes an exponential rate function, $R_t(s) = A\exp(-as)$, we can write the probability functions for incoming and outgoing particles undergoing some transition (neutralization or de-excitation) at a position s in an element ds as

$$P_t^i(s,v) = (A/v)P_o^i(s,v)\exp(-as) \quad (2.15)$$

$$P_t^o(s,v) = (A/v)P_o^o(s,v)\exp(-as) \quad (2.16)$$

where P_o^i and P_o^o are the probabilities an incoming and outgoing particle will survive to reach a position, s, while in its original ionization or excitation state, and v is the normal velocity of the incoming or outgoing atom. These values are

$$P_o^i = \exp\left(-\int_S^\infty (R_t/v)ds\right) \quad (2.17)$$

$$P_o^o = \exp\left(-\int_0^S (R_t/v)ds\right) \quad (2.18)$$

The incoming transition probability of eqn. 2.15 has a peak at $s_m = (1/a)\ln(A/av)$, so this transition is most likely to occur in a small region centered about s_m from the surface.

Evidence for energy level variation can be found in the energy distributions of the ejected electrons from Auger processes [10]. The image-charge interaction between a singly charged ion and the surface is given by -3.6(eV)/s(Å). For the case of 10 eV He^+ ions incident on tungsten, the ions had undergone a potential energy shift of $\approx$ 2 eV, which was attributed to the image-charge potential. If we assume the transition occurs at a distance

Reproduced with permission of the copyright owner. Further reproduction prohibited without permission.

near s_m, and equating the 2 eV shift to the image-charge potential, we find that the value of s_m is on the order of ≈ 1.8Å. Hagstrum has calculated values for 40 eV Ne^+(2.4 Å), Ar^+(3.0 Å) and Kr^+(3.2 Å). Of the processes described above, it should be noted that direct Auger neutralization appears to be the dominant process [10] by about an order of magnitude.

2.2.1 Reflection Characteristics

The ion/neutral reflection efficiency is defined as the ratio of the flux of reflected hyperthermal neutrals to the flux of ions incident to the metal surface. Very little experimental determination of ion reflection efficiency exists. Roslyakov and Fiksel [18] determined a reflection efficiency of $R_N \approx 60\%$ for 100 to 600 eV H^+ ions incident on stainless steel and niobium surfaces. They also determined that the reflected neutrals retained approximately 30% of the incident ion energy. These values compare favorably with the work of Cuthbertson [11, 19] where energy reflection efficiencies of 30 to 50% were obtained depending on the incident ion species and reflector material.

2.2.2 Effect of Applied Magnetic Field

Chodura [20] has studied the effect of an oblique magnetic field on a plasma sheath. For very large magnetic fields (ion cyclotron frequency equals electron plasma frequency), it was found that substantial deviations from normal incidence could be found. That is, ions incident on a surface with normal at an angle Φ with respect to a magnetic field would strike the surface at non-normal angles. This is in contrast to the case in the absence of a magnetic field where the ion would be electrostatically collimated by the surface-normal electric field represented by the sheath.

Although this work utilizes a small magnetic field to assist in plasma stream collimation, the ions are still expected to strike the reflector surface near-normal. For a plasma density of 1×10^{11} cm^{-3} at the reflector plate and an electron temperature of 3 eV, the sheath width is approximately $d \approx 5\lambda_{de} = (5)(743)(\sqrt{T_e/n_e})$ [cm] $= 0.02$ cm (where λ_{de} is the Debye

Reproduced with permission of the copyright owner. Further reproduction prohibited without permission.

shielding length of a plasma of density n_e and temperature T_e). The argon ion gyroradius for an ion temperature of 0.5 eV and a magnetic field of 60 gauss is $r_{Li} = 7.6$ cm. So the ion is expected to undergo only a fraction of a revolution in the space of the electrostatic sheath. Thus, the ions are assumed to have normal incidence at the reflector plate.

2.3 Hyperthermal Neutral Stream Source Description

A schematic view of the neutral stream source appears in Fig. 2.11. In general, it consists of a plasma source to provide adequate ionized and dissociated reactive species, a biased reflector plate, and a chuck designed to hold the wafer to be processed. An external view of the apparatus appears in Fig. 2.12.

The plasma source is a 3 1/2 turn copper coil incorporated with a rf matching network (called a "matchbox"). The matchbox is capable of 1000 W operation at 13.56 MHz. Water cooling is provided through the matchbox to the ICP coil.

The vacuum chamber is an 8″ Conflat, 6-way cross. A 450 l/s turbo-molecular pump is used to reach a base pressure of approximately 10^{-8} Torr. Feedstock gas (Ar, O_2, Ne, CF_4, etc.) is introduced through 20 sccm (full range) adjustable mass flow controllers, which allow precise control over molecular gas mixtures. Pressure is controlled by an 8″ variable conductance gate valve.

The reflector plate is a 5 1/2″ 304 series Stainless Steel disc, brazed to a copper coil The copper coil acts as the mount for the plate, as well as allowing water cooling during operation in the plasma. Water cooling of the plate has been very successful; the plate temperature has been determined to stay in the range of 26 to 30 C° even after 30 minutes at 800 Watt operation. The tungsten plate is clamped directly to the stainless steel plate when tungsten reflection experiments are required.

A dc bias in the range of −60 to +60 volts can be applied to the plate. In general, however, the useful bias range is 0 to -30 volts to avoid sputtering of the plate or sinking electrons from the plasma. This results in an overall incident ion kinetic energy range of 15

Reproduced with permission of the copyright owner. Further reproduction prohibited without permission.

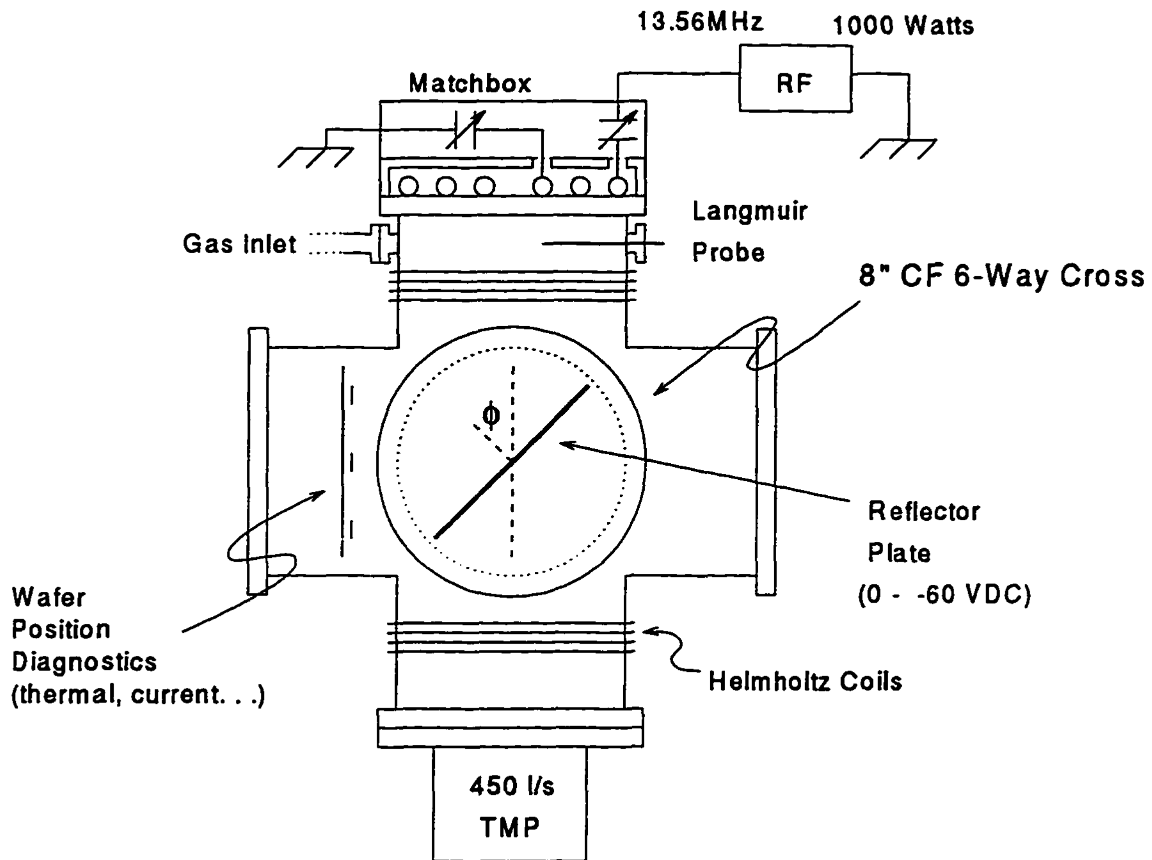

Figure 2.11: Schematic of the surface reflection neutral stream source.

Reproduced with permission of the copyright owner. Further reproduction prohibited without permission.

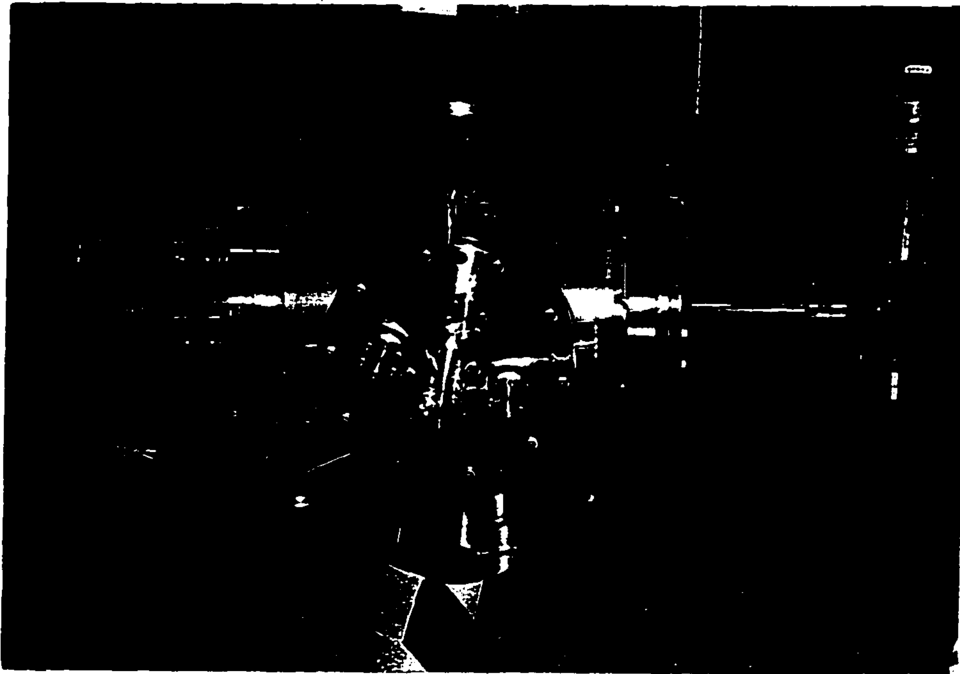

Figure 2.12: A photo of the surface reflection neutral stream source. The matchbox/coil is mounted on top of the 6-way cross above the top Helmholtz coil (multi-colored annulus). The 3 1/2 turn ICP coil is constructed of 1/4″ copper tubing. The coil is incorporated into a 1000 W, 13.56 MHz matching network. This configuration allows easy installation on any 8″ vacuum flange.

Reproduced with permission of the copyright owner. Further reproduction prohibited without permission.

to 45 eV, assuming a plasma potential on the order of 15 volts.

A tungsten plate, fabricated from a high-purity magnetron sputter target, can be clamped to the stainless steel plate. The clamps are set such that the tungsten plate is in good thermal contact with the stainless steel backing plate. Because the tungsten plate is much thicker than the steel plate, it is expected that its temperature is somewhat higher, although this has not been measured. In any case, the elevated temperature has not been shown in other experiments [18] to affect the final reflection properties.

The wafer stand is designed to hold five etch samples to allow study of the etch rate and angular distribution uniformities. Plasma densities are also measured at these five positions via Langmuir probes. This is important because plasma leakage to the wafer position and its effect on etch rate is an important parameter to be determined by this experiment. The wafer position sample holder can be replaced by a Quartz Crystal Monitor (QCM) which allows *in situ* etch rate measurements.

A collimator can be installed to assist in removal of plasma while allowing free flow of neutrals to the wafer position. Plasma rejection using this technique is accomplished by aligning the collimator apertures such that the applied B-field is perpendicular to the openings. While the ion gyroradius at the expected magnitude of the B-field of 60 gauss is approximately 7.6 cm, the electron gyroradius is 0.02 cm. This results in rejecting pure plasma from the wafer position, although the ions can still stream through the apertures with appreciable energy.

Reproduced with permission of the copyright owner. Further reproduction prohibited without permission.

Chapter 3

Neutral Stream Source Modeling

3.1 Introduction

In general, the neutral stream source discussed in this work consists of three important stages: the plasma source of ions, the ion diffusion region, and the wafer region. In order to maximize the delivery of hyperthermal neutrals to the wafer region, three conditions must be met.

First, the plasma source must provide a high density of ions for reflection. The inductively-coupled-plasma (ICP) source described in Chapter 2 has been shown to provide a high ion density at a low plasma potential. This source can also be made radially uniform by the introduction of a magnetic multipole confinement scheme (discussed below). This source is finding increasing use in the semiconductor processing industry as a plasma based etch reactor.

Once the ions are created, they must then traverse the distance from the localized plasma creation region to the reflector plate with minimal loss due to recombination and elastic scattering. Due to the low-pressures required by the ICP, the mean free path for the ions is large, leading to a large ion flux at the reflector plate.

Finally, the neutrals reflecting from the biased metal plate must traverse the background gas and the plasma without substantial loss due to collisions and charge exchange.

Reproduced with permission of the copyright owner. Further reproduction prohibited without permission.

The dominant loss channel for these neutrals is elastic scattering, which will be described below. Thus, lower background pressures in the diffusion and wafer stages are desirable.

In order to understand the effects of background pressure and plasma density on the reflected neutral flux, a number of modeling efforts were undertaken. First, a simulation of possible vacuum system geometries was completed using the Vacuum System Transient Simulator (VSTS) written by Grumman Aerospace for the Department of Energy. This simulation assessed the possibility of using pulsed gas and plasma to assist in delivering the maximum flux of reflected neutrals to the wafer.

A 2-dimensional and 3-dimensional ray tracing model was used to simulate the reflected neutral flux profiles at the wafer. These models led to an understanding of many of the issues relevant to uniformity of the profiles. However, these models did not allow evaluation of the angular or energy distributions at the wafer, which are very important to etch characteristics of the source.

Finally, a full 3-D Monte Carlo simulation of the neutral trajectories from the reflector plate was completed. This model considered the plasma creation stage, ion diffusion to the reflector, and reflection of the neutrals. The neutrals were followed through collisions with the background and interactions with the plasma. Energy and angular distributions, as well as 3-D reflected neutral flux profiles at the wafer, were obtained from this simulation.

This Chapter and the next describe each of these models in detail. The results from each model are presented and discussed. Comparison of the experimental results and the simulations will be discussed in Chapter 5.

3.2 Vacuum System Modeling

For the vacuum system modeling, we took our geometry to be the most likely configuration for a production device. A schematic of the modeled device appears in Fig. 3.1. The plasma source dimensions (D_s and L_s) will be discussed below. The diameter of the processing stage is D_p = 30 cm, with a length of L_p = 30 cm. This gives an approximate

Reproduced with permission of the copyright owner. Further reproduction prohibited without permission.

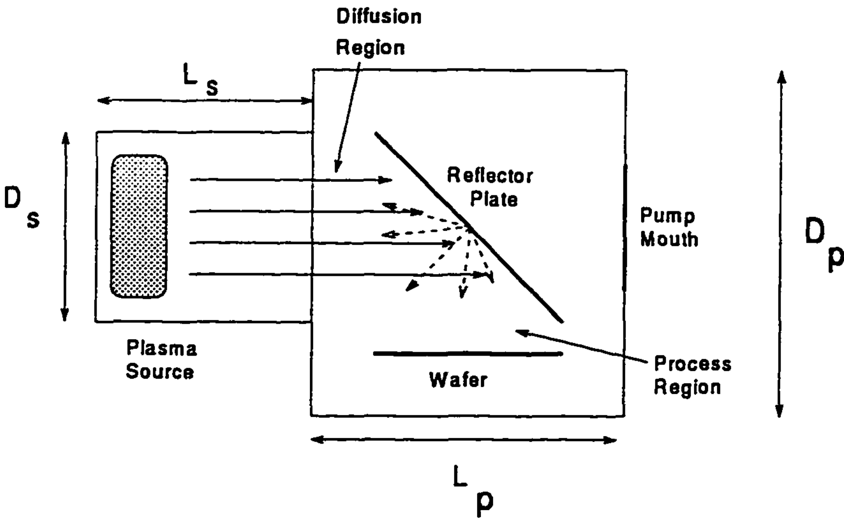

Figure 3.1: Generalized vacuum system modeled by VSTS.

Reproduced with permission of the copyright owner. Further reproduction prohibited without permission.

characteristic dimension of 45 cm (diagonal of a right-circular cylinder with $D = L$).

3.2.1 Vacuum System Transient Simulator

VSTS calculates pressures at various points in a vacuum chamber using the dimensions of each part of the system to calculate conductances. A gas pulse rate is specified and the pressures calculated as the gas traverses the system to the vacuum pump of the specified size.

For VSTS simulation of a continuous or pulsed source gas load, we calculate conductances from analytical expressions when available [21,22] including correction factors determined analytically or through Monte Carlo simulations for a number of possible geometries. Following conductance determinations, "ducts" of equivalent conductance are inserted into the VSTS model. In this way, we are able to determine the effect of conductance limits on pumpdown during processing.

The calculated conductances assume that flow is molecular. Roth [22] shows that the lower limit of the transitional flow region is found based on the condition

$$P * D = 10\left(\frac{T}{M}\right)^{1/2} \eta \text{ [Torr} - \text{cm]} \tag{3.1}$$

where P[Torr] = lower pressure limit to the transition region, D = characteristic dimension of the process chamber (which could be radius or length, or some diagonal), T = neutral background temperature [K], M = mass [amu], η = viscosity [poise]. For oxygen at T = 293 K, $\eta = 2.05 \times 10^{-4}$ poise. The condition of eqn. 3.1 then gives PD = 6.2×10^{-3} Torr-cm. For our case, where P in the process chamber is desired to be $< 10^{-4}$ Torr, and D = 45 cm, then PD = 4.5×10^{-3} Torr-cm. Our molecular flow assumption is then justified if the pressure stays below 1.4×10^{-3} Torr. It is unnecessary to make assumptions about the plasma source geometry conductances because VSTS considers all regimes of flow. A conductance analysis presented later will show if the required pressure gradient is obtained with the geometry.

All of the VSTS simulations begin with an N_2 partial pressure of 1 mTorr, which is pumped away and replaced by the O_2 pulsed into the system. The pumps are generic pump types of variable pump speed with an assumed 0.1 second start-up time. The simulations do

Reproduced with permission of the copyright owner. Further reproduction prohibited without permission.

not consider the entire range of pumpdown from atmosphere because we are interested in the operational behavior of the source, not the start-up characteristics. This is justified by the generally fast roughing speeds available and the small volumes discussed here. Although our neutral source may operate with a number of feed gases, we have used oxygen as the pulsed gas in our simulations. The temperature generally remains at 293 K.

We can estimate a period and duty cycle for pulsed operation based on effective (conductance limited) pumping speed S_{eff}, volume V, and desired final pressure, P_f and initial pressure, P_i, through [22]

$$t = \tau = -2\frac{V}{S_{eff}} \ln \frac{P_f}{P_i}. \tag{3.2}$$

This estimate is a starting point for determining pulsed mode operations and can be fine tuned between simulations. An initial estimate of source load is determined by $Q_{flow} = S_{eff}P$, where P is the desired operating pressure of the source and Q_{flow} is the feed gas flow rate. This value is also fine tuned between simulations to give the desired pressure in the source region. As an example, for the dimensions described above, V = 21.2 Liters, S_{eff} = 3500 Liters/sec is the pump speed used for this simulation, P_f and P_i are 10^{-4} and 10^{-3} Torr, respectively. We then get an approximate pumpdown time of 30 msecs. Thus we could expect to pulse gas at 30 Hz and still reach our pressure goals.

To simulate the contribution to the conductance limit of the reflector plate, we assume that the conductance of the plate at an angle to the plasma stream, as shown in Fig. 3.1, is not appreciably different from that of an elbow with an aperture equal to that of the reflector/plasma stream cross section (Fig. 3.2). The validity of this assumption is probably poor, and highly dependent on the type of reflection assumed. For diffuse reflection the conductance will probably be higher than that calculated for the elbow case, and for specular reflection, higher still. Thus we can take our calculation to be a worst case conductance limit.

In a pulsed system, it is possible that etching will proceed in a stepwise fashion, wherein some fraction of the reagent stream adsorbs to the surface where it undergoes subsequent formation of intermediates on the way to forming desorbable products. These reac-

Reproduced with permission of the copyright owner. Further reproduction prohibited without permission.

tions may be synergistically enhanced by particle or photon bombardment from the source. Presently, detailed rates for such intermediate steps are unknown in general. This gas load model does not consider desorption of reactants due to vapor pressure effects, except that we only require the pressure following source gas pulses to fall to 10^{-4} from approximately 10^{-3} Torr. We do include gas load due to desorption of etch products in the model as a leak of the expected magnitude.

The required gas load on the system will be highly dependent on the operating characteristics of the plasma source. For these calculations, the geometry is assumed to be that of the flat-spiral coil inductively coupled plasma (ICP) source described in Chapter 2. However, the dimensions of the plasma source region are varied to ascertain their effect on the overall performance of the vacuum system.

A number of Monte Carlo parameterizations that have been done on geometries interesting to the vacuum community have been reviewed by Roth and O'Hanlon [21,22]. We begin here with a possible analytical solution.

In order to maintain beam integrity following reflection, we require that less that 10% of the reflected neutral stream be lost by scattering or reionization in the plasma zone. This 10% collisional beam loss requires the background pressure in the process region should be low compared to the dimension of this region

$$\lambda_{\mathrm{mfp}} = 2.33 \times 10^{-20} \frac{T}{\xi^2 P} > 10D \tag{3.3}$$

where T[K] is the background temperature (approximately 293 K), P[Torr] is the background pressure, ξ is the effective diameter of the oxygen molecule in cm (approximately 3.65×10^{-8} cm), and D is the characteristic dimension of the process region ($d_{\mathrm{avg}} \approx 12$ cm). At $T =$ 300 K, $D = 12$ cm, this requirement gives $P = 4.3 \times 10^{-5}$ Torr. For a loss coefficient of 1%, $P = 4.3 \times 10^{-6}$ Torr. This requirement is of the utmost importance for production of a uniform, high flux neutral stream. However, very large pumping speeds are required to keep up with the source gas load for low etch rate or low reflected-neutral creation efficiency. Thus for a source to be viable, very high ion source densities and high dissociation fractions

Reproduced with permission of the copyright owner. Further reproduction prohibited without permission.

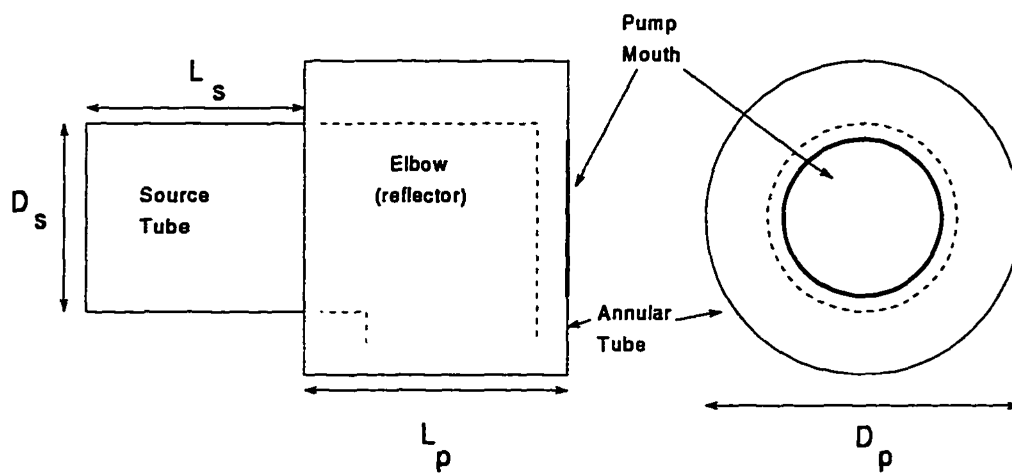

Figure 3.2: Decomposition of process chamber geometry into model components.

Reproduced with permission of the copyright owner. Further reproduction prohibited without permission.

for molecular reagents are required.

The ICP source discussed in Chapter 2 is capable of providing a high ion density. Barnes, et al. [17], have characterized the planar-coil inductively coupled plasma source for oxygen discharges. It was found that at 2 mTorr and an rf power input of 1000 W, $n_i = 9.5 \times 10^{11}$ cm^{-3}. At this power, the electron density decreases slightly with further increase in pressure.

The pressure in the source to attain the above ion density is 2 mTorr as identified by Barnes, et al. [17]. We can estimate a flow rate to achieve this pressure based on the conductance limited pump speed. Below we detail a model of the conductance limit imposed by the source geometry. We will break the vacuum system into three main parts: the plasma source, the neutral-reflection region, and the pump mouth. A conductance for each region will be calculated, then each part will be put together in the appropriate combination of series and parallel for the VSTS model.

While previous studies of this planar-coil ICP have involved low aspect ratio sources (AR = depth of source/diameter), some modeling suggests that a high aspect ratio source may improve uniformity [23]. Our source for this model is a tube as shown in Fig. 3.1 (25 cm D x 25 cm L). Gas is puffed in the upstream region by a distributed ring structure to assure uniformity in the power deposition region.

For the plasma source tube, the conductance can be taken to be that of a "short" tube, for which the conductance is [22]

$$C_{shorttube} = 3.81\left(\frac{T}{M}\right)^{\frac{1}{2}}\frac{D^3}{L}K_c \tag{3.4}$$

where D is the diameter of the tube, $L =$ is the length of the tube, T is the gas temperature [K], M is the mass of the flowing gas [amu], and K_c is Clausing's factor

$$K_c = \frac{15(\frac{L}{D}) + 12(\frac{L}{D})^2}{20 + 38(\frac{L}{D}) + 12(\frac{L}{D})^2} \tag{3.5}$$

which is an empirically derived correction to the standard short tube conductance expression in eqn. 3.4. This correction factor agrees well with Monte Carlo simulations. Using eqns. 3.4

Reproduced with permission of the copyright owner. Further reproduction prohibited without permission.

and 3.5 with particular choices of source dimensions we get the conductances in Table 3.1.

D (cm)	L (cm)	C (L/sec)
25.4	25.4	2900
25.4	20.4	3183
20.4	25.4	1692

Table 3.1: Dimensions (D, L) of the plasma source region and the associated conductances (C).

The process chamber is modeled as an annular tube of length L_o and outer diameter D_o in parallel with an elbow of aperture D (D = diameter of wafer = 20.32 cm). This assumption is shown in Fig. 3.2. The pump mouth is placed behind the reflector plate and has dimensions L_{Pump} and D_{Pump}. We use the definition [22] of transmission probability, p_r, as $C = p_r C_o$, where C_o is the "black hole" conductance of the entrance aperture, and C is the "real" conductance found by Monte Carlo techniques reported by Roth [22].

The black hole conductance is given by

$$C_{\text{blackhole}} = 3.67\left(\frac{T(\text{K})}{M(\text{amu})}\right)^{\frac{1}{2}} A_{\text{ap}}[L/sec] \tag{3.6}$$

where $A_{ap}[\text{cm}^2]$ = area of entrance aperture. Fig. 3.3 shows the transmission probability as a function of L/D for an elbow. We take $L = 2 \times$ (elbow diameter) (from examination of Fig. 3.2) and find $p_r \approx 0.37$. The area of the aperture can be calculated from dimensions $A_{\text{ap}} = \pi D^2/4 = \pi(20.32)^2/4 = 324.3$ cm^2. At $T = 293$ K for oxygen, $C = C_{\text{elbow}} p_r = 1332.5$ L/sec.

Similarly for the annular tube in parallel, $A_{ap} = \pi(D_p^2 - D^2)/4 = 377.4$ cm^2, $C_{\text{blackhole}_{\text{ann}}} = 4400$ L/sec. From Fig. 3.3(b), we find $p_r \approx 0.5$ for our assumption of $L_p = 30$ cm, and $D_p = 30$ cm. Using eqn. 3.6 then, $C_{\text{ann}} = C_{\text{blackhole}_{\text{ann}}} p_r = 2200$ L/sec.

In our model, these conductances are in parallel, so the conductance of the process chamber is given by

$$C_{\text{process}} = C_{\text{ann}} + C_{\text{elbow}} = 3532[L/sec] \tag{3.7}$$

Reproduced with permission of the copyright owner. Further reproduction prohibited without permission.

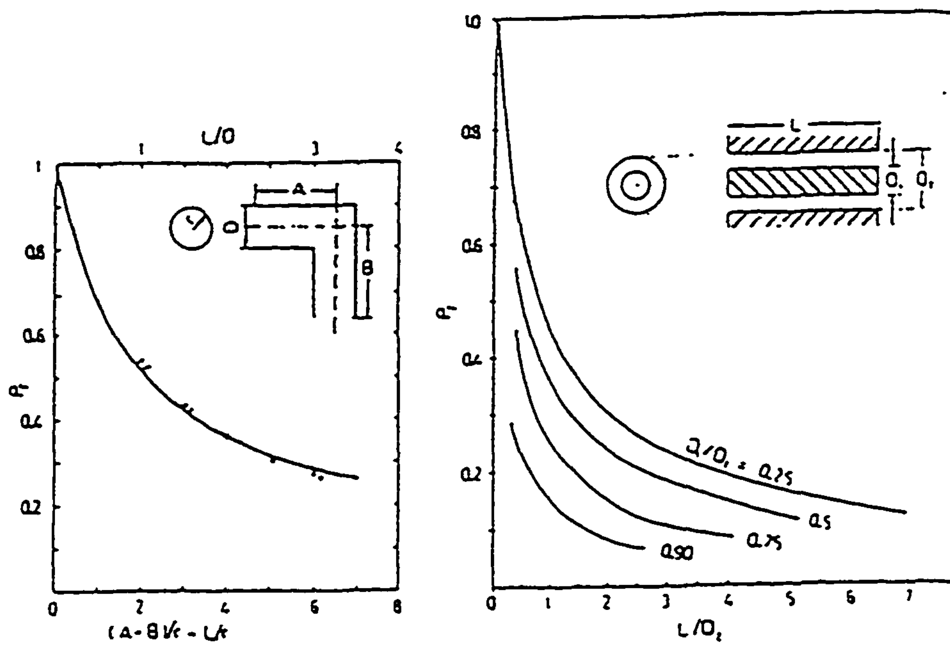

Figure 3.3: Transmission probabilities for (a) elbow and (b) annular tube as reviewed by Roth [22].

Reproduced with permission of the copyright owner. Further reproduction prohibited without permission.

The pump mouth is modeled as a 40 cm diameter tube 5 cm in length. Using eqns. 3.4 and 3.5 for the pump mouth, $C_{\text{pumpmouth}} = 12,200$ L/sec. The total conductance following the source then is given by conductances in series

$$C_{\text{tot}} = \frac{C_{\text{pumpmouth}} C_{\text{process}}}{C_{\text{pumpmouth}} + C_{\text{process}}} = 2740\ [L/sec] \tag{3.8}$$

To simulate this conductance in the VSTS calculation, the short tube equation, eqn. 3.4, is used. Taking $L = 10$ cm (arbitrarily) and setting the conductance to that of eqn. 3.8, we can solve for the required diameter of the tube used to simulate the process chamber geometry. The above assumptions give $D = 13.3$ cm. The dimensions $D = 13.3$ cm and $L = 10$ cm are then given to the VSTS model.

Fig. 3.4 shows the vacuum system as it is represented in VSTS. Gas is introduced at node 1 (plasma source), traverses a tube of the dimensions given for the source tube above, then connects at node 2 to the tube simulating the process geometry. Following, at node 3, appears the pump mouth, turbo-molecular pump and backing pump. The pumps described for use in VSTS use speed curves for commercially available units; *i. e.*, the pumping speeds and characteristics are realistic.

3.2.2 VSTS Results

Fig. 3.5 shows the ideal behavior of the proposed pumping system. The pressure in the source should maintain 10^{-3} Torr during a plasma pulse and return to approximately 0.1 mTorr before the next pulse to prevent gas buildup. In the process region, the pressure should stay below the 0.1 mTorr required for 10% beam loss as detailed previously. This can be accomplished with appropriate conductance limits on the plasma source that allow maintenance of high ion density on the reflector plate.

Fig. 3.6 shows the results of a VSTS simulation using the above geometry. Gas is pulsed into the system from a 5 Torr-Liter/sec valve with a duty cycle of 0.05 and pulse widths of 2 msec. We note the pressure separation between the source region (Node 1) and process region (Node 3). However, the behavior exhibited in Fig. 3.6 is not the ideal shown

Reproduced with permission of the copyright owner. Further reproduction prohibited without permission.

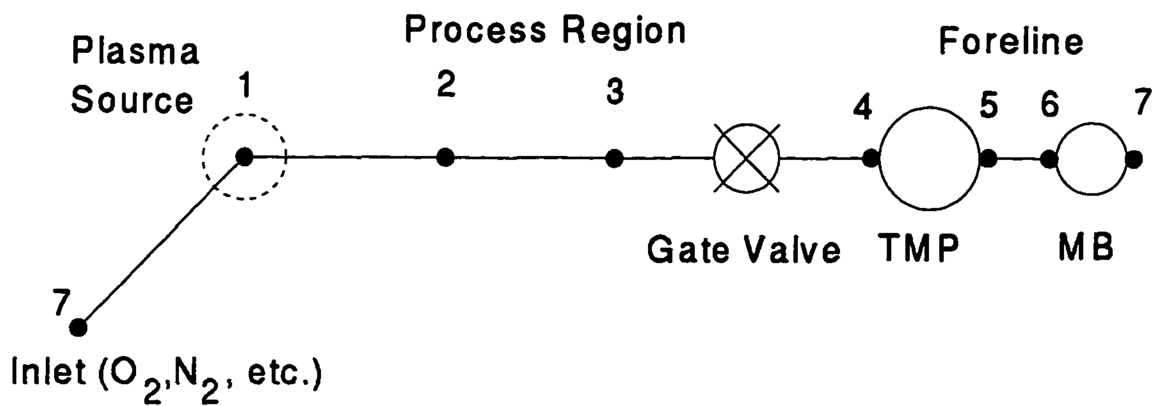

Figure 3.4: Model components for VSTS simulation. Each node is labelled where pressure and flow rate data is taken. Each component in the source as described in the text appear as nodes. The gas inlet node and backing pump outlet node are set equal to ambient pressure.

Reproduced with permission of the copyright owner. Further reproduction prohibited without permission.

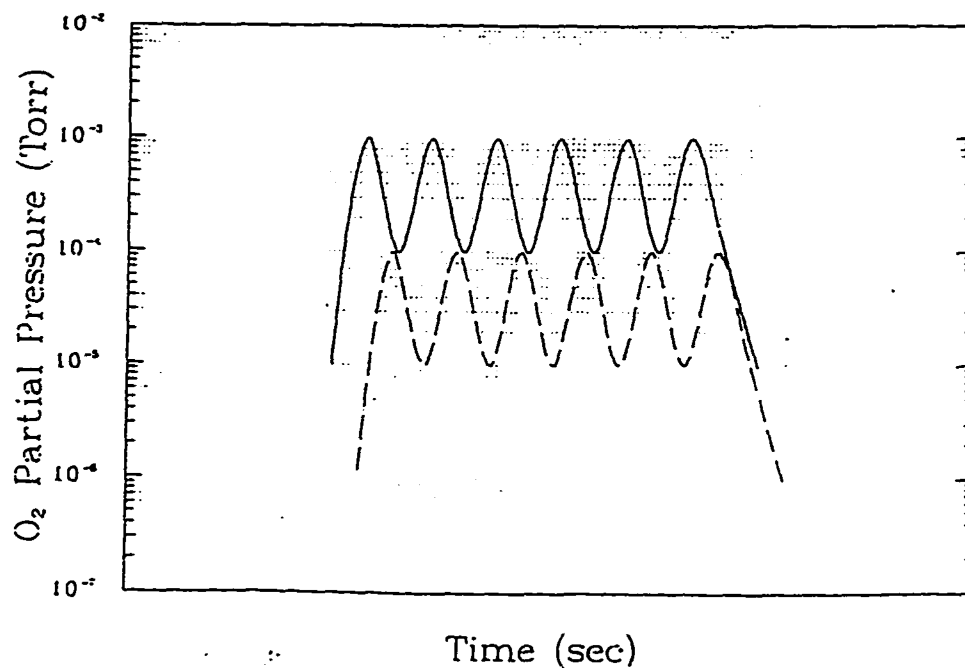

Figure 3.5: The ideal pulsed pressure behavior of the VSTS simulated system. We require that the peak of the pressure in the plasma source reach 10^{-3} Torr, while the pressure in the neutral reflection region stay below 10^{-4} Torr.

Reproduced with permission of the copyright owner. Further reproduction prohibited without permission.

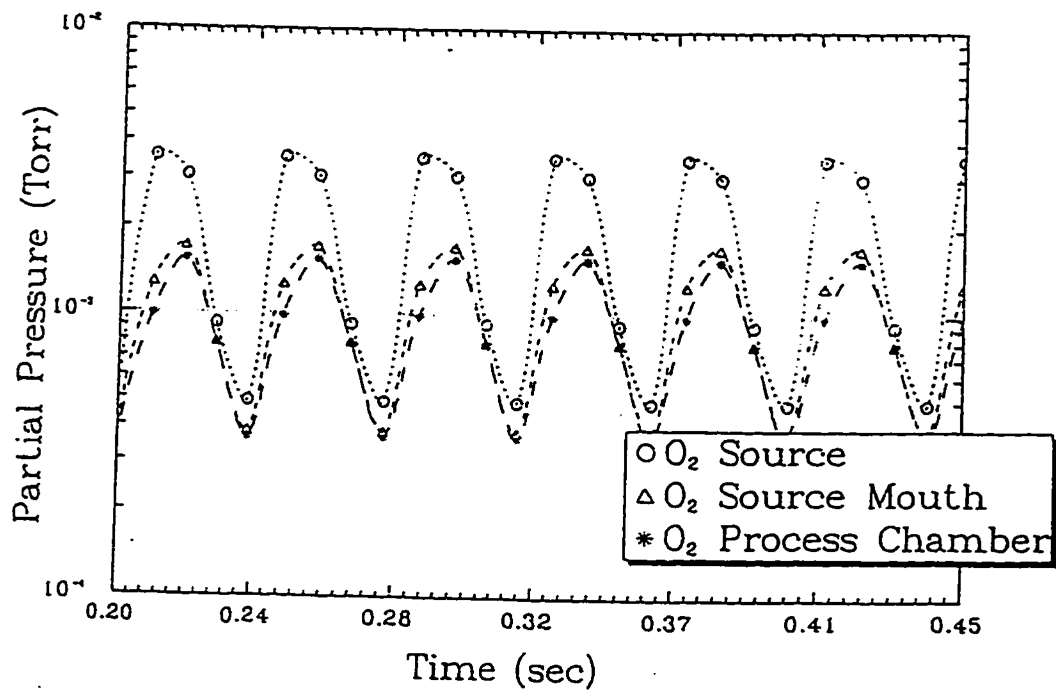

Figure 3.6: Results of a VSTS simulation with current geometry. Oxygen (0_2) is pulsed with a duty cycle of 0.05 with 2 msec pulses. The valve flow rate is 5 Torr-liter/sec.

Reproduced with permission of the copyright owner. Further reproduction prohibited without permission.

in Fig. 3.5, but it does suggest a possible solution. Further conductance limits can be placed on the source tube, providing that ion delivery to the reflector plate is not reduced below the point of viability.

We reduce the flow rate to 0.5 Torr-Liter/sec so that the peak pressure reached is the desired 10^{-3} Torr. For a flow rate of 0.5 Torr-Liter/sec we can estimate the required conductance limit suggested above from $Q = C(P_2 - P_1)$, where $P_2 - P_1$ is the required pressure drop, and Q is the throughput (flow rate). Taking $P_2 = 10^{-3}$ and $P_1 = 10^{-4}$, we get $C = 555$ L/sec. This seems quite small (compared to other conductances in the system) considering that the plasma stream will probably be affected adversely by such a small conductance. A tube of 11 cm in diameter and 20 cm in length is used to simulate the conductance following the same procedure as for the process chamber. When a conductance of this magnitude is given to the VSTS model, the profile of Fig. 3.7 is produced. Fig. 3.7 shows that we do indeed get the desired pressure gradient. However, the conductance limit placed on the tube in order to reach the desired results becomes unpractical when applying to plasma source design.

It is expected that an additional pressure gradient between the source and reflector can be achieved with an alternative pump placement. In Fig. 3.8 the pump mouth is placed on the wall perpendicular to the wafer and the plasma source. This should increase the conductance of the process chamber providing a further decrease in pressure. We model the conductance as that of the pump mouth only, previously calculated to be 12200 L/sec, in series with the aperture conductance from eqn. 3.6 where $D = 40$ cm. This gives $C = 6667.5$ L/sec. Using this value in VSTS gives the profile of Fig. 3.9. Note the further decrease in process chamber pressure compared to Fig. 3.7. The source is still required to be conductance limited as done for the profile of Fig. 3.7, however. Thus the alternate pump placement does not present enough improvement to remove the conductance limit. For the pump placement as in Fig. 3.8, the length of the process chamber is increased accordingly.

Reproduced with permission of the copyright owner. Further reproduction prohibited without permission.

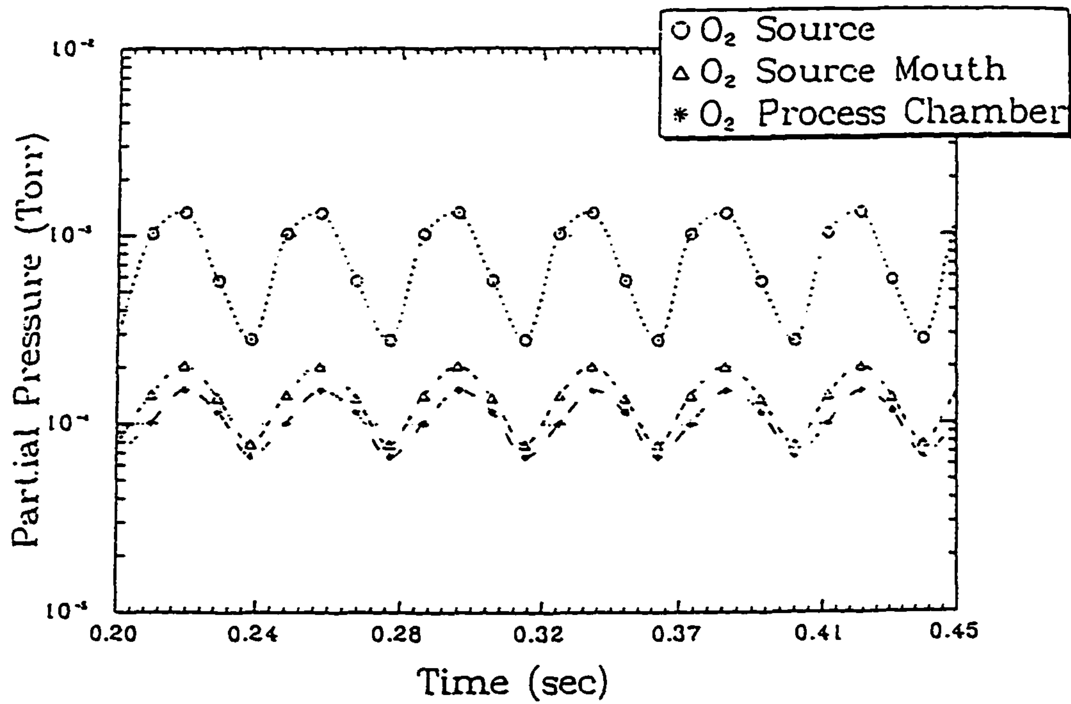

Figure 3.7: VSTS simulation with reduced flow rate and conductance. These values are closer to the ideal behavior suggested in Fig. 3.5. However, the necessary conductance limit would impose too much of a hindrance to plasma flow to be viable.

Reproduced with permission of the copyright owner. Further reproduction prohibited without permission.

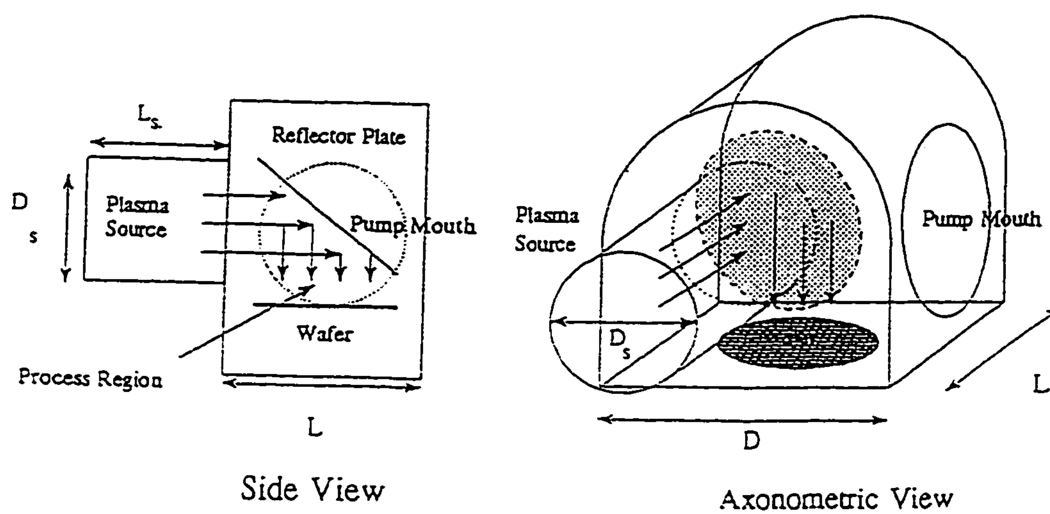

Figure 3.8: Alternate pump placement for VSTS simulation.

Reproduced with permission of the copyright owner. Further reproduction prohibited without permission.

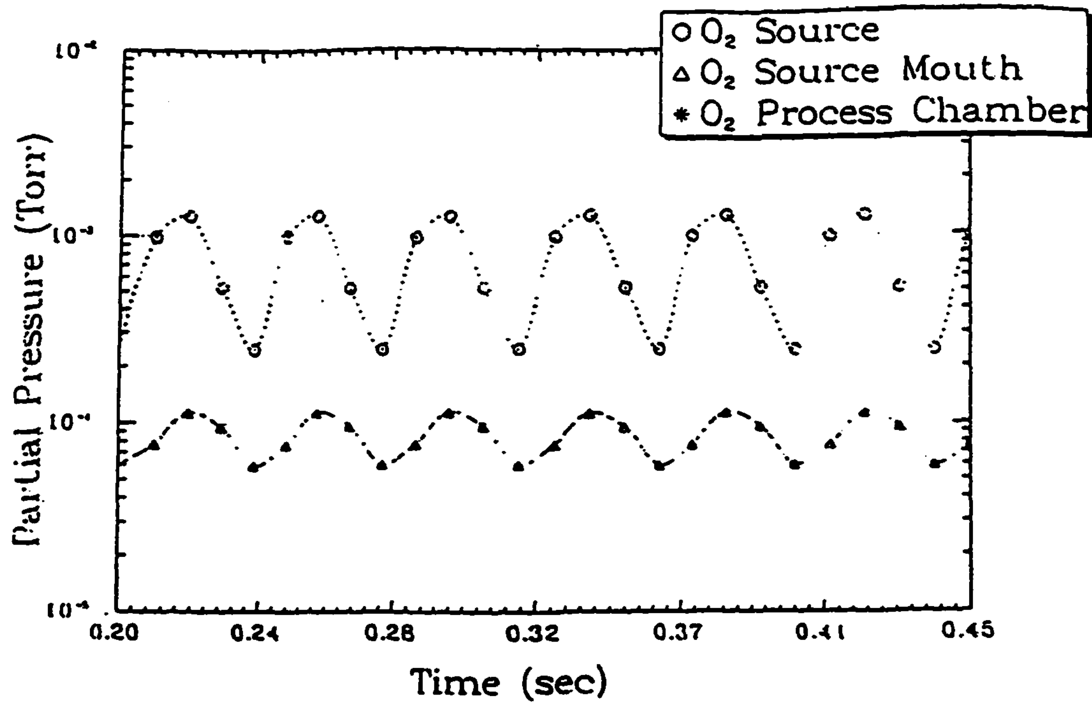

Figure 3.9: Simulation results for alternate pump placement. There is notable improvement in the downstream pressure, but the conductance limit is still required.

Reproduced with permission of the copyright owner. Further reproduction prohibited without permission.

3.2.3 VSTS Conclusions

Pulsed operation of the plasma and vacuum system were considered as a method for increasing the mean free path of reflected neutrals. However, it was found that in order for this to be effective, impractical geometrical constraints on the plasma source region were required. Further, it should be noted that assuming that the plasma source is on at the same duty cycle as the pressure pulses, the etch rate found due to reflected neutrals will be reduced by that amount. For a 5% duty cycle, the material removal rate will be 5% of the constant plasma source value. For the remainder of this Chapter, the source will be assumed to operate in constant plasma/pressure mode.

3.3 3-D Ray-Tracing Model

A 3-D ray tracing model was used to determine the effects of reflector angle and pressure on the reflected neutral flux uniformity at the wafer. This model does not include shaping of the reflector plate or non-symmetrical plasma density profiles. Collisions are only considered with the introduction of an exponential flux attenuation factor dependent on pressure through the mean free path. The plasma density profile is assumed based on profiles found for similar plasma sources in the literature.

3.3.1 3-D Model Description

The plasma density profile is given by

$$n(r,z) = n_o \left(1 - \frac{r^2}{r_o^2}\right) \exp\left(\frac{-z}{25\text{cm}}\right)) \tag{3.9}$$

where r is the distance from the center of the plasma source in the plane of the source, r_o is the radius of the plasma source and wafer, and 25 cm is the exponential falloff distance found in the literature for an electron cyclotron resonance (ECR) plasma source [24] which is similar to the ICP in the sense that it has a very localized ionization region.

Reproduced with permission of the copyright owner. Further reproduction prohibited without permission.

Given the above plasma density profile, the ion flux to a unit area on the reflector plate at position (r, z) is given by

$$\Gamma_i = \frac{1}{2}n(r,z)c_s = \frac{J_i}{e} \tag{3.10}$$

where c_s is the ion sound speed and J_e is the ion current density.

The ions are then reflected from the plate as neutrals. Each unit area is assumed to be a point source with a $1/r^2$ dependence. The flux to each unit area of the wafer from each unit area of the reflector plate is

$$\Gamma_{rn} = \frac{J_i A_n r_n}{e 2\pi r^2} f(\theta) \tag{3.11}$$

where A_n is the unit area of the reflector plate, r_n is the reflection efficiency, assumed 0.5 in this work (although it could vary from 30 to 50%), r is the distance between the reflector point source and the unit area of the wafer receiving the flux. $f(\theta)$ is the angular dispersion of the reflected neutral flux, $f(\theta) \propto \cos^n(\theta)$. The exponent n is taken from the literature and varies depending on neutral/reflector-plate material combination [11] ($n = 0.8 - 2.1$).

The flux is further attenuated by an exponential factor

$$f(r, E, P) = \exp\left(\frac{-r}{\lambda(E,P)}\right) \tag{3.12}$$

where λ(E,P) is the energy and pressure dependent mean free path for reflected neutral/background neutral collisions. The function λ is inversely dependent on pressure, and the energy dependence is shown in Fig. 3.10. The energy dependence is due to the decrease in collision frequency for hyperthermal neutrals over cold thermal neutrals.

3.3.2 3-D Ray-Trace Results

This simple model gives a picture of which parameter settings are best for improving flux uniformity. We primarily vary pressure, reflector plate angle, and the degree, n, of the reflection dispersion function. Fig. 3.11 shows the effect of varying the reflector plate angle, ϕ from 45° (a) to 55° (b) at a pressure of 0.3 mTorr. The density profile is assumed to

Reproduced with permission of the copyright owner. Further reproduction prohibited without permission.

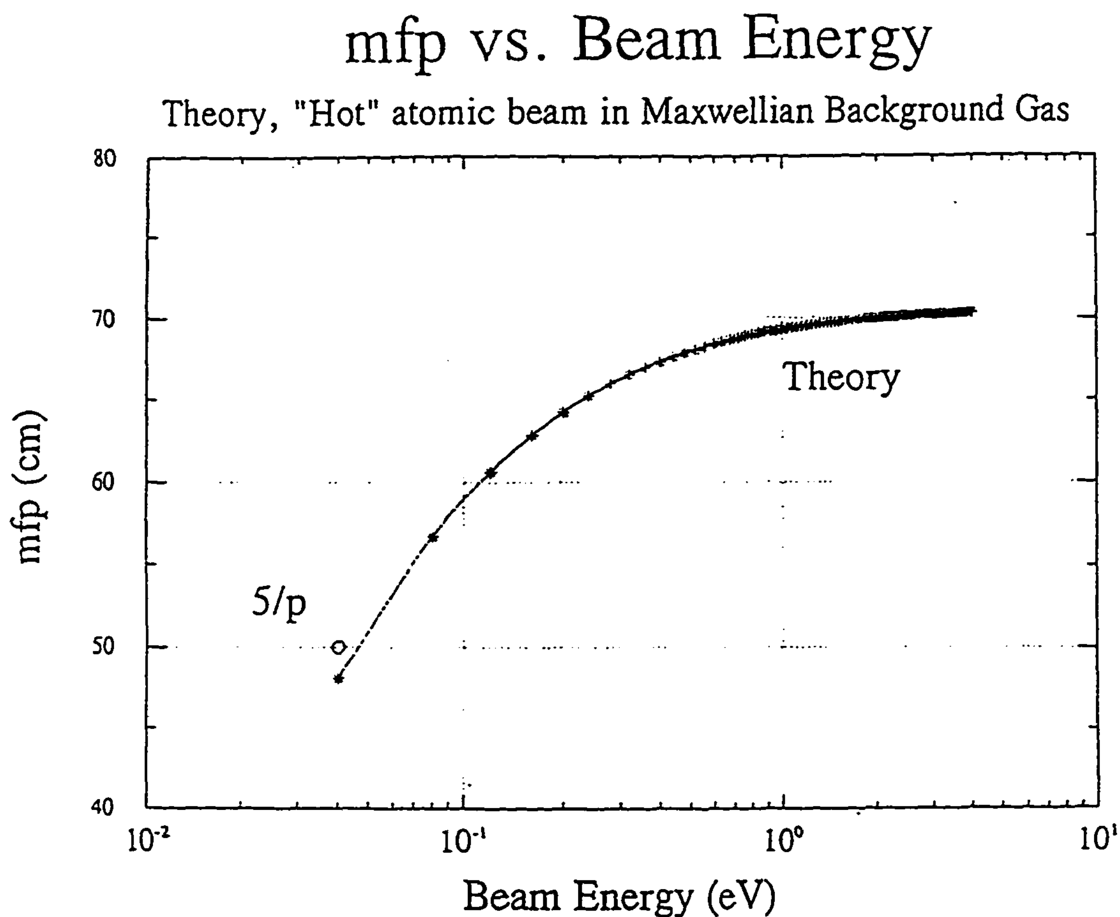

Figure 3.10: The variation of global mean free path with atom energy. These values are for a hot oxygen atom traveling through a cold oxygen background. The canonical value of mean free path for cold atoms, 5/p(mTorr) [cm], is shown for comparison. These values represent the energy dependence of neutral mean free paths in the 3-D ray trace model.

Reproduced with permission of the copyright owner. Further reproduction prohibited without permission.

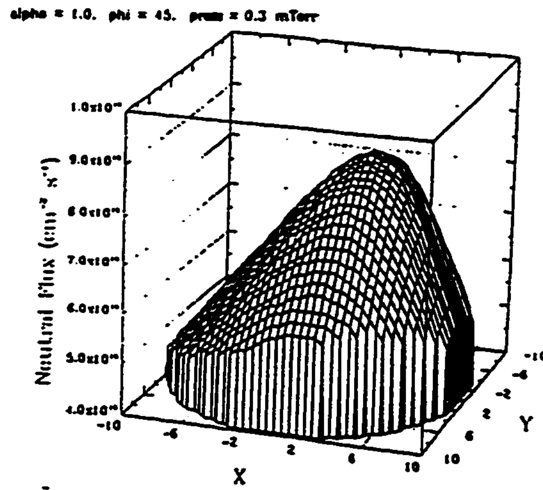

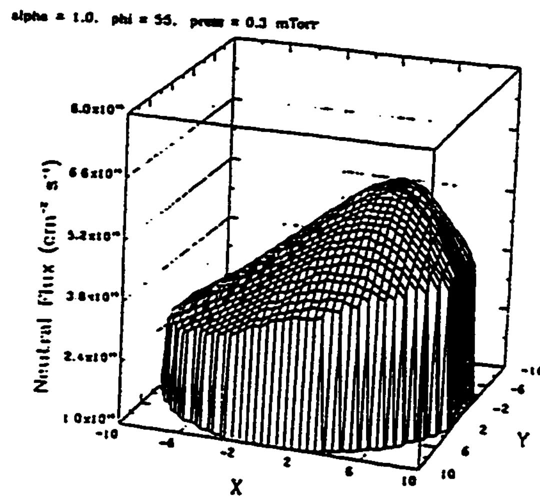

Figure 3.11: 3-D ray trace results for (a) 45° and (b) 55°. Note the shift in the peak towards the reflector.

Reproduced with permission of the copyright owner. Further reproduction prohibited without permission.

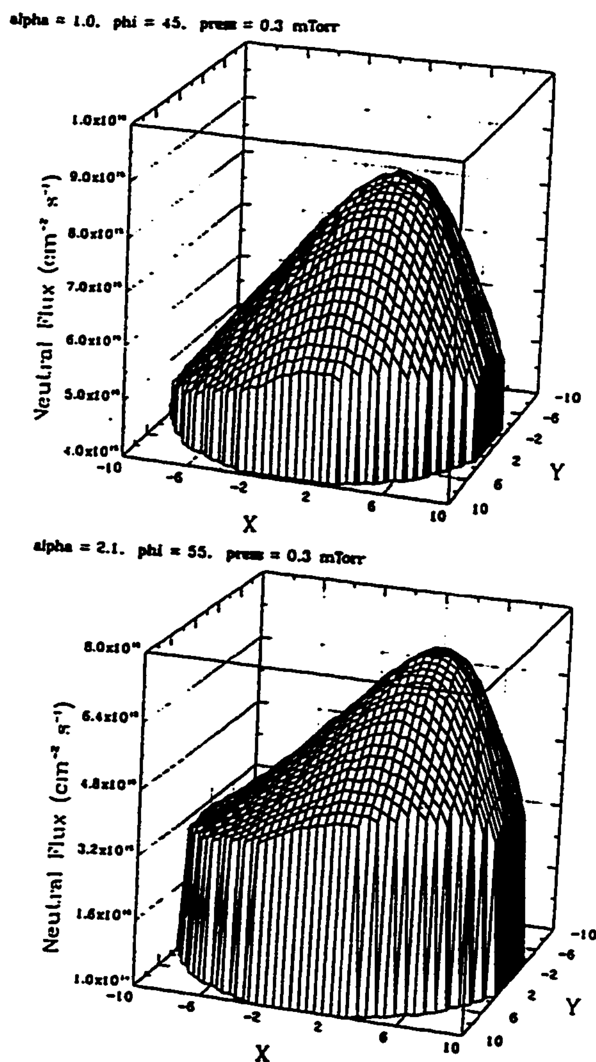

Figure 3.12: 3-D ray trace results for (a) n = 1.0 and (b) n = 2.1 at 55°, where n is the exponent of the cosine emission distribution, $\cos^n(\theta)$.

Reproduced with permission of the copyright owner. Further reproduction prohibited without permission.

be of the form in eqn. 3.9, with a reflection dispersion degree value of n = 1.0. While the uniformity (= std. dev./mean) in Fig. 3.11(b) is still higher than 50%, it does show improved uniformity over the 45° case of Fig. 3.11(a). The more realistic case of $n = 2.1$ is shown in Fig. 3.12(b). The uniformity does not show the same improvement as in Fig. 3.11. This is due to the slightly more directed flux represented by a larger n.

The effect of plasma density profile variation is shown in Fig. 3.13 (a) and (b). In Fig. 3.13(a) the profile is given by eqn. 3.9. In Fig. 3.13(b), the profile is assumed to be radially flat, but it maintains the exponential falloff with z as in eqn. 3.9. We note that a more radially uniform profile produces a more uniform reflected neutral flux at the wafer. This is important because the ICP source used for the experimental portion of this work is quite uniform, but not completely flat, as will be described in Chapter 4.

In Fig. 3.14(a) and (b), we see the effect of varying pressure on the reflected flux. In going from 0.3 mTorr to 3 mTorr, the flux uniformity and magnitude is attenuated drastically. This shows the adverse effect of failing to maintain a low pressure in the reflection region. However, it should be noted that the exponential attenuation factor defined previously does not properly account for high energy elastic collisions. The assumption in this model is that after a single collision, the reflected neutral is lost by thermalization or randomization. However, in reality, a reflected neutral could suffer several small angle collisions while losing very little energy in the process. A more accurate picture could be obtained from a full 3-D Monte Carlo trajectory simulation.

3.4 2-D Ray-Tracing Model

3.4.1 Model Descriptions

Multi-Source Model

We have approximated the multi-source 3-d surface reflection neutral beam source using the 2-dimensional geometry appearing in Fig. 3.15. Although a direct comparison

Reproduced with permission of the copyright owner. Further reproduction prohibited without permission.

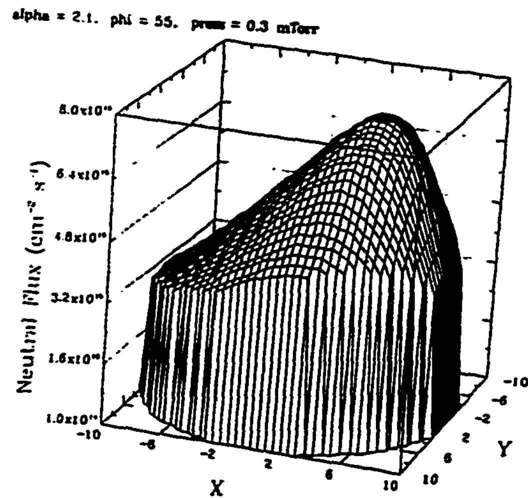

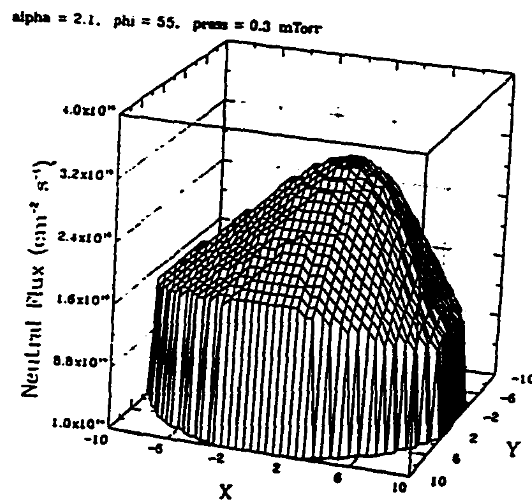

Figure 3.13: Effect of Variation of the plasma density radial profile on the 3-D flux wafer maps. (a) is the profile obtained by using eqn. 3.9, while (b) is obtained with a constant (flat) radial distribution and an exponential falloff in z as in (a).

Reproduced with permission of the copyright owner. Further reproduction prohibited without permission.

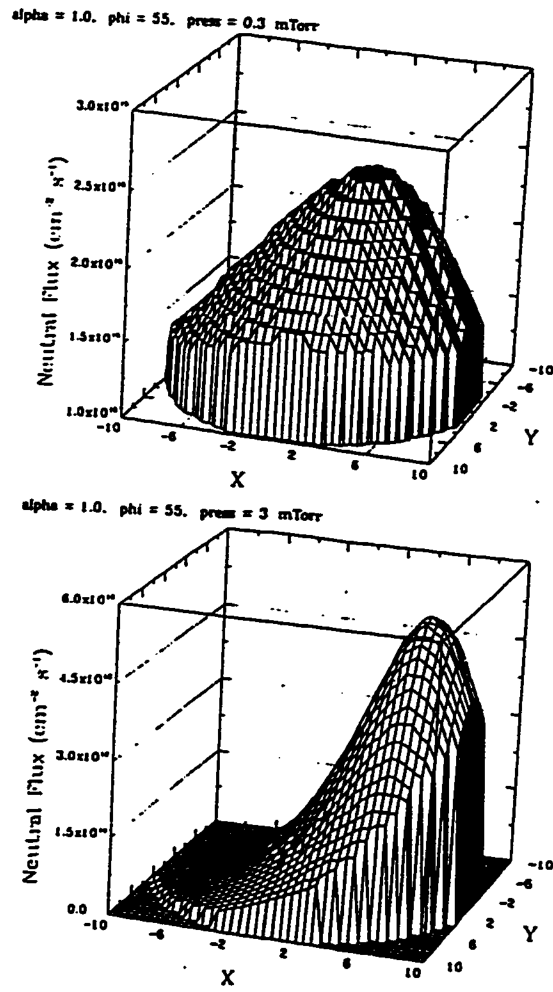

Figure 3.14: Pressure effects on reflected neutral flux.

Reproduced with permission of the copyright owner. Further reproduction prohibited without permission.

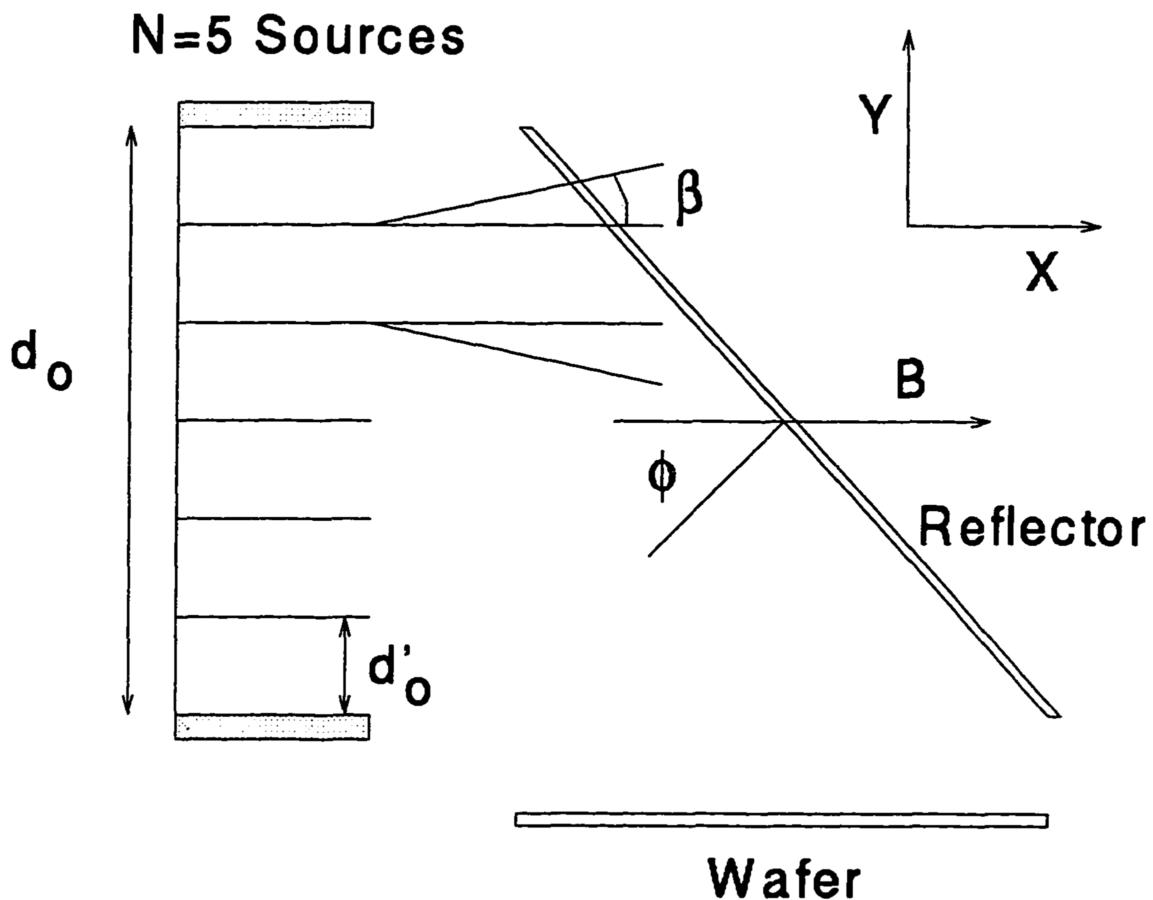

Figure 3.15: Schematic representation of the 2-D multi-source geometry. d_o is the diameter of the source array, d'_o is the diameter of each individual source ($d'_o = d_o/N$), N is the number of individual sources. β is the plasma dispersion parameter of eqn. 3.14. The coordinate system used in text discussion is shown. The reflector shown is a flat, non-shaped plate.

Reproduced with permission of the copyright owner. Further reproduction prohibited without permission.

between this 2-d and the later 3-d model is not attempted, the 2-d model is useful for elucidating the important geometrical aspects of the reflector plate.

In this model, we define a characteristic diameter, d_o, equal to the wafer diameter, $2r_o$. The diameter of each individual source is then $d'_o = d_o/N$, where N is the number of sources. Each source is represented by a 'parabolic' plasma density profile given by

$$n_k = n_{o_k}\left(1 - \left(\frac{\rho}{d'_o/2}\right)^2\right)^m \tag{3.13}$$

where n_{o_k} is the peak density for source k, k = 1,2,. . .,N, and ρ is the radial distance from center point of source k, and m = the degree of the profile ($m < 1$ gives a flatter profile, m > 1 gives a more sharply peaked profile). The peak density of each source can be selected independently to increase uniformity at the wafer, which is the ultimate goal. A schematic representation of the 2-dimensional multi-source plasma generator appears in Fig. 3.15. Reflection from the reflector plate for shaped and planar geometries is described below.

As the plasma ions and electrons diffuse along a collimating magnetic field, B, to the reflector, the density profile is allowed to disperse with connection length (distance from emitter to receiver of flux) described by

$$R = \frac{d'_o}{2} + x\sin\beta \tag{3.14}$$

where R is the radius of plasma column at connection length x, β is a constant parameter denoting the slope of the dispersion (see Fig. 3.15).

Shaped Reflector Model

We consider two general shapes for the reflector plate. A multi-faceted plate with variable dihedral angles between the facets, and a machined plate with a stair-step shape. Both shapes appear in Fig. 3.16. For the multi-faceted reflector, the shape is constrained so that the end of one section of reflector corresponds to the beginning of another, and that the 2-d projection of the reflector on the wafer plane is approximately d_o, the wafer diameter.

Reproduced with permission of the copyright owner. Further reproduction prohibited without permission.

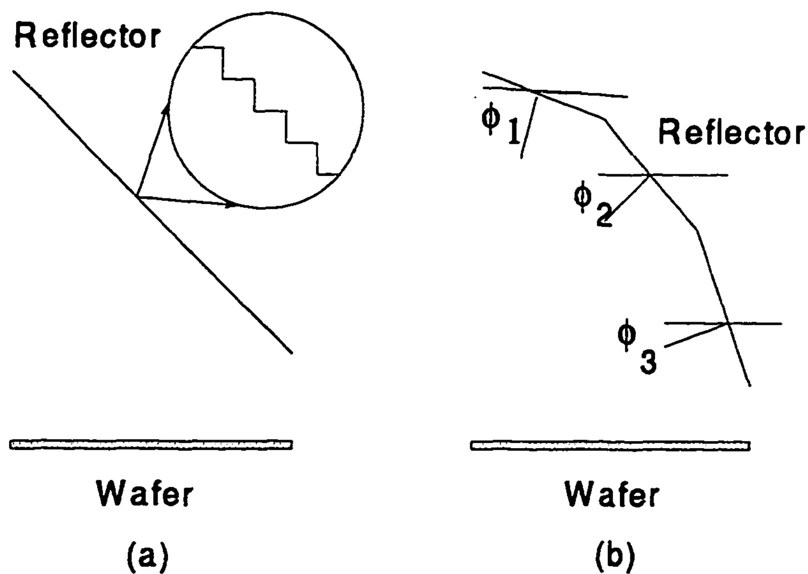

Figure 3.16: Two possible shapes for a reflector plate. (a) 'stair-step' and (b) multi-faceted reflector. In (a), the angles shown, and used in the simulations, are 0° and 90° with respect to the collimating B-field. Note that any set of angles could be chosen, including a set such that the plate locally resembles (b). In (b), the angle ϕ_i (i = 1, 2, . . .,N) are the angles between each facet normal and the collimating B-field.

Reproduced with permission of the copyright owner. Further reproduction prohibited without permission.

This leads to the approximate constraint

$$\sum_{m=1}^{M} \tan\phi_m \approx M \qquad (3.15)$$

where M is the number of reflector sections and ϕ_m is the angle of reflector segment m with respect to the applied B-field. The center angle is chosen and the other angles are then found by satisfying eqn. 3.15. If eqn. 3.15 is satisfied, the projection of the 2-d reflector on the wafer plane has a length approximately d_o. The above model is only valid in the low M limit, $1 \leq$ M ≤ 5. For M larger than 5, the sum in eqn. 3.15 becomes increasingly larger than M. Thus the geometry gets too large and complex for the required distribution of angles to be practical. Other geometric considerations must be included for M > 5.

The stair step model of the reflector consists of steps machined in the surface of a flat plate (see Fig. 3.16). Although any distribution of angles is possible, for the simulations shown below, the angles chosen are $\pi/2$ and 0 with respect to *wafer* normal (not the reflector normal).

Model of Reflection Characteristics

As in the single source 3-d model, reflection is assumed to be diffusive and of the form

$$f(\theta) = \frac{\cos^n(\theta)}{N(n)} \qquad (3.16)$$

where θ is the angle of flux from reflector with respect to reflector normal, n is the degree of diffusivity ($n \approx 2.1$ in some cases [11]), and $N(n)$ is the normalization constant. The flux from a point on the surface of the reflector to a point on the wafer is then given by

$$\Gamma = \frac{j_+ l}{r} r_n f(\theta) f(r) \qquad (3.17)$$

where j_+ is the current density delivered to a unit length l, r is the distance to wafer position, r_n is the reflection coefficient (although r_n is not known in general, some work [11,19] suggests it falls in the range of 30 - 50%, for this work we take a value of approximately 0.5). To

Reproduced with permission of the copyright owner. Further reproduction prohibited without permission.

determine the effect of pressure on the wafer flux, an elastic attenuation factor of

$$f(r) = e^{-r/\lambda} \tag{3.18}$$

is included, where r is the distance to wafer point from reflector emission point and $\lambda = (1.4)(5/P)$ [cm] where P is pressure in mTorr. The use of $5/P$ is the canonical mean free path for air [25], which, for thermal neutrals, will not be much different than the value for Ar. The factor of 1.4 comes from the decrease in the elastic collision cross section when hyperthermal atoms interact with a cold Maxwellian background gas (see Fig. 3.10), increasing the directed flux surviving to impact the wafer [26, 27].

In the 2-d model, we resolve the angular distributions at selected points on the wafer. The resulting distributions, shown in a later section, only represent transport from the source to the wafer without being randomized by elastic collisions with the background gas. In reality, collisions must be treated with a Monte Carlo method to accurately account for randomization of the stream by elastic collisions. This is done in the 3-d Monte Carlo simulation discussed later in this Chapter.

3.4.2 Results of 2-D Modeling

Simulations are carried out with the goal of high uniformity in neutral flux over the diameter of the wafer. To this end, a variety of multi-source, shaped reflector combinations were studied. For each geometry simulated, the uniformity parameter = standard deviation/mean was calculated and is reported for each case. This parameter is used to determine the relative quality of each run and thus guides the parametric design of the model. Angular distributions for each are also shown in order to understand the effects of each geometry on isotropy.

2-D Uniformity

It was clear for a multi-source case that the peak density of each source should be varied independently to adjust the neutral fluxes at the wafer. Fig. 3.17 shows the flux results from a three plasma source, planar reflector at 45° and 55° to the B-axis (see Fig. 3.15 for

Reproduced with permission of the copyright owner. Further reproduction prohibited without permission.

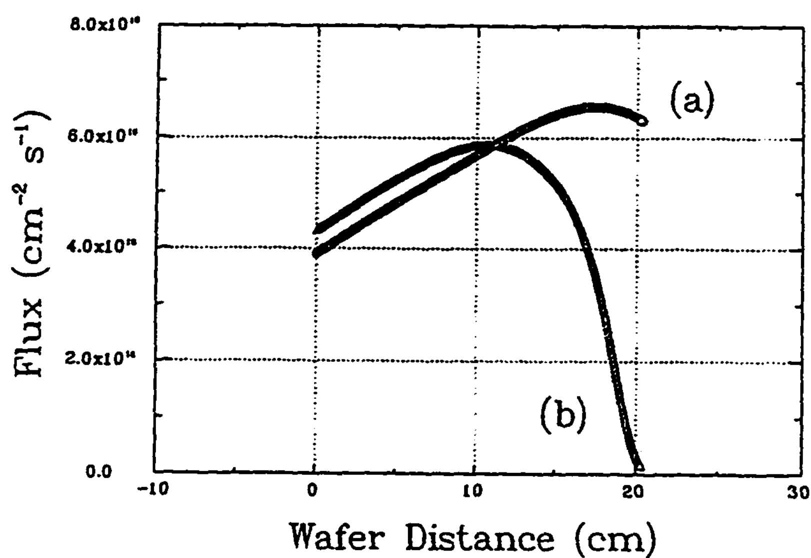

Figure 3.17: 2-D flux results for 3 sources (all with the same density, $n_o = 2.5 \times 10^{13} cm^{-3}$) illuminating a single, planar reflector plate. Distance along wafer is with respect to origin along the y-axis (see Fig. 3.15). (a) $\phi = 55°$, uniformity = 15.3%. (b) $\phi = 45°$, uniformity = 29.2%.

Reproduced with permission of the copyright owner. Further reproduction prohibited without permission.

geometry), where the peak density and radial profile of each source were chosen to be the same at $n_o = 2.5 \times 10^{13} cm^{-3}$, m = 1.0 (see eqn. 3.13).

The apparent uniformity increase shown for the 55° case over 45° is due to the reflector normal being directed more towards the wafer. $\phi = 55°$ has been found experimentally to be approximately the optimal angle for maximizing flux in a single source design [11]. However, as discussed later, the 3-d Monte Carlo simulation suggests that the minimum in uniformity occurs at 45° (for one large source). This discrepancy is easy to understand when one considers that the single source experiments were much smaller in scale, where only the central portion of the flux was sampled.

The flux has a more wafer-normal component in accordance with eqn. 3.16. Since the average flux seems to also increase, the next step is to vary the density distribution at the sources. As a test, the source closest to the wafer was turned off. It was found that the effect of this source is minimal for the 55° case. Fig. 3.18 shows the three source, planar reflector system at 55° with central densities 2.5, 1.0 and 1.0×10^{13} cm^{-3} and m = 1.0 for each, highest to lowest (see Fig. 3.15). The uniformity of this flux across the wafer is 2.2% with a peak at 2.76×10^{16}cm^{-2}s^{-1} (4.5 mA/cm^2).

The analysis leading to Fig. 3.18 shows the possibility of controlling plasma density profiles in the source region to control wafer neutral flux uniformity. If the discretized multi-source analysis above is extended to the continuum case, *i. e.*, a non-uniform single plasma source, wafer flux uniformity should be similarly affected. This assumption is tested below.

Next, the effect of shaping the reflector is considered. In what follows, we assume that the sheath follows the contour of the shaped reflector. The well-known sheath thickness variation with applied B-field is ignored in the analysis. As stated in Chapter 2, we assume the flux to be electrostatically collimated by the sheath potential drop. Recall the two particular shapes under consideration from Fig. 3.16. Fig. 3.19(a) shows a wafer flux profile from a single parabolic source, with parabolic degree $m = 1.0$, and a multi-faceted ($M = 5$) reflector plate. The particular angles chosen are 55°, 55°, 45°, 35° and 25° from top to bottom. For

Reproduced with permission of the copyright owner. Further reproduction prohibited without permission.

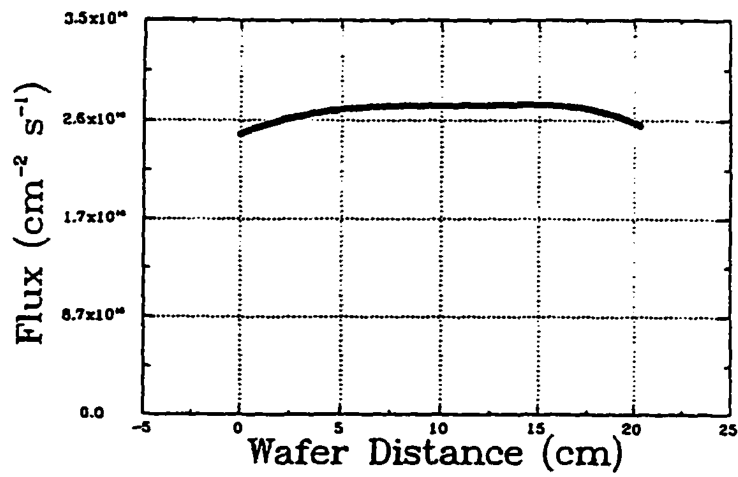

Figure 3.18: 2-D flux results for 3 sources with densities of 2.5, 1.0 and 1.0 × $10^{13} cm^{-3}$ (top to bottom). Uniformity = 2.2%.

Reproduced with permission of the copyright owner. Further reproduction prohibited without permission.

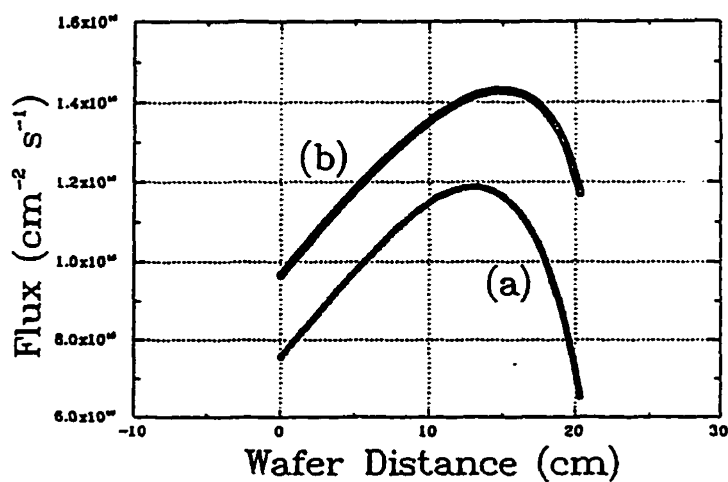

Figure 3.19: 2-D simulation results for multi-facet ($M = 5$) plate with single plasma source. (a) parabolic source density profile ($m = 1.0$) and (b) flat density profile. Uniformities: (a) 12.5%, (b) 10.7%

Reproduced with permission of the copyright owner. Further reproduction prohibited without permission.

this set of angles, $\sum_{m=1}^{M=5}\tan(\phi_m) \approx$M= 5. The same set of angles are used for the profile of Fig. 3.19(b) where the source parabolic degree is set to $m = 0.1$, *i. e.*, a flat source density profile. We see in Fig. 3.19 that the flatter source profile has little effect on shape or uniformity over the wafer but does increase the total flux since the integral of flux over the source dimension is larger. Indeed, when skewed parabolic profiles are used, *i. e.*, peaked on one side of the source, the shape and uniformity (not shown) are virtually unaffected. Selective power deposition in a single plasma source system would be effective in shaping the plasma profile. However, the tunability of a single source is not as selective as an array of several source tuned individually as we do in this analysis. This does not mean that some single source profile could not be found to satisfy the uniformity criterion, more detailed analysis will be needed to determine this shape.

To determine the effect of a combination of multiple sources and the multi-faceted plate, we turn to Fig. 3.20. Here we have a multi-faceted plate (M = 3) at angles 55°, 45°, and 35°, and 3 plasma sources. In Fig. 3.20, an attempt is made to find some combination of source densities that results in a uniformity of 5% or less. Fig. 3.20(c) shows an array of densities as in the profile of Fig. 3.18. Noting the difference between Fig. 3.20(c) and Fig. 3.18 we see the importance of having the reflector surface normal closer to that of the wafer. In Fig. 3.20, as in all multi-faceted reflector plates, the surface normal of the lower plates is far from that of the wafer, *i. e.*, the angle in the distribution of eqn. 3.16 is small, thus the flux is small on one end of the wafer. At the same time, the near normal flux from the lower plates illuminates the far side of the wafer creating a large peak in neutral flux there. Thus the multi-faceted reflector plates produce non-uniform profiles as well as very off-axis angular profiles, as we shall see below.

The problem associated with high angle reflections can possibly be avoided by the use of the stair step plate as shown in Fig. 3.16. Here the surface normal of each position is directed at the wafer, or, according to eqn. 3.16, a higher fraction of flux in the direction of the wafer. There will be considerable flux from the reflector normals parallel to the B-field

Reproduced with permission of the copyright owner. Further reproduction prohibited without permission.

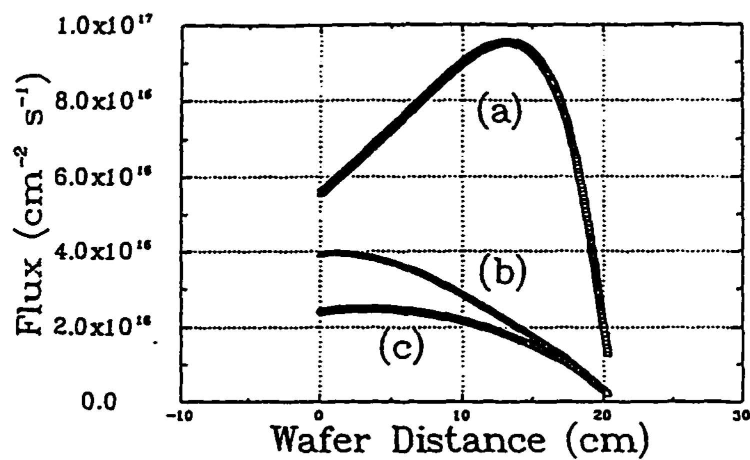

Figure 3.20: Combination of multiple sources ($N = 3$) and multi-faceted ($M = 3$) reflector plate with angles of 55°, 45°, 35°. (a) Source densities of 2.5, 3.0 and 5.0 $\times$ 10^{13}cm^{-3} from top to bottom (b) 5.0, 1.0, and 1.0 $\times$ 10^{13}cm^{-3}, and (c) 2.5, 1.0, and 0.5 $\times$ 10^{13}cm^{-3}.

Reproduced with permission of the copyright owner. Further reproduction prohibited without permission.

(see Fig. 3.16) but will also be at very high angles as suggested about the multi-faceted reflector. The angular distributions will be discussed in the next section.

Fig. 3.21(a) shows the calculation of a seven-source, single-facet reflector using the stair step reflector shape compared to the same case with a flat reflector under the same conditions in Fig. 3.21(b). The plate is at 55° with source densities of $5.0, 3.0, 1.0, 0.95, 0.7, 0.5$, and $0.3 \times 10^{13} cm^{-3}$, with $m = 1.0$. The stair step reflector gives a uniformity of 5.4%, while the non-shaped, planar reflector gives 18.2%. The loss of flux apparent in the shaped case is due to the fact that approximately 1/2 of the flux is directed along the B-axis from the step face normal parallel to B. This shows that there is a favorable effect on uniformity from the use of a stair step reflector plate rather than a simple flat reflector.

To see the effect of tuning the source densities we calculated the flux profile using a step reflector under the same conditions as in Fig. 3.18 ($M = 1$, $N = 3$ sources). The results are shown in Fig. 3.22. The same tuning used to get Fig. 3.22(b) with uniformity = 2.2% does not give a similarly uniform profile for the stepped case in Fig. 3.22(a) with a uniformity of 18%. The comparison does suggest that a different tuning may give desired results. Fig. 3.22(c) shows results from the same stepped reflector as in (a) but with a different set of source densities. The densities are $2.5, 0.5$, and 0.5×10^{13} cm^{-3}, top to bottom, and $m = 1.0$ which gives a uniformity of 4.8%. We noted previously that changing the source density profile to $m = 0.1$, which is flatter than $m = 1.0$, has little effect on the shape or uniformity at the wafer, but it does tend to increase the flux. Thus, sources with flatter density profiles would be desirable for a flux critical process.

Angular Distributions

We now investigate the angular distributions at three positions on the wafer. The positions are: 2 cm from source end (designated as Left), the center point, and 2 cm from the far end of the wafer (called Right). Fig. 3.23 shows these positions in relation to the plasma source and reflector plate.

Reproduced with permission of the copyright owner. Further reproduction prohibited without permission.

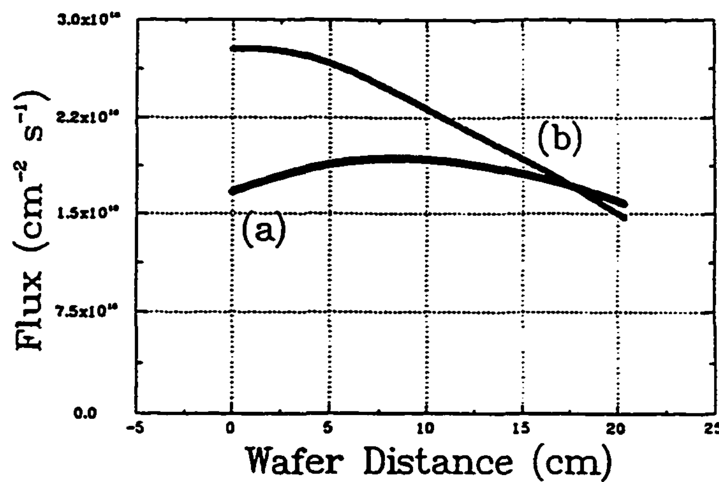

Figure 3.21: Seven source. single reflector configuration. (a) shows the stair step reflector shaped reflector and (b) shows the flat, non-shaped reflector. In both cases, the plate is at 55° with source densities described in the text. Uniformity in (a) is 5.4% while (b) gives 18.2%.

Reproduced with permission of the copyright owner. Further reproduction prohibited without permission.

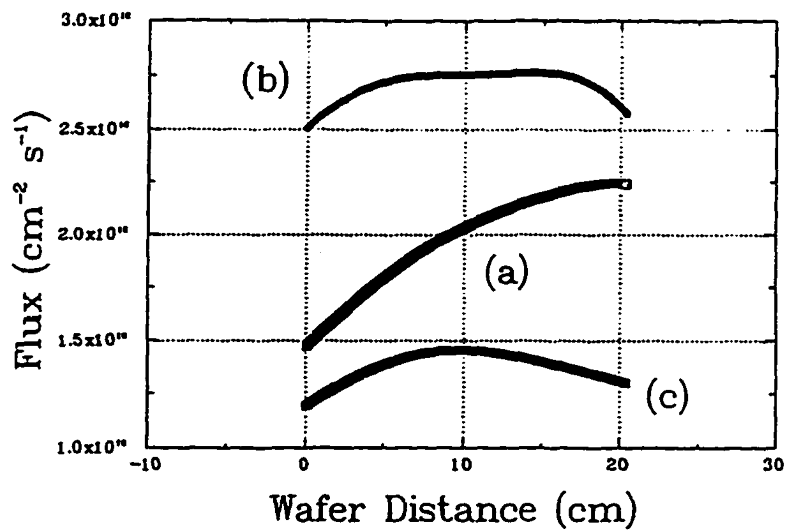

Figure 3.22: Effect of tuning sources on stair step uniformity. (a) shows results with stair step under same density conditions used to obtain Fig. 3.18, shown again in (b). (c) gives results for the same reflector in (a) with different densities ($2.5, 0.5$, and 0.5×10^{13} cm^{-3})

Reproduced with permission of the copyright owner. Further reproduction prohibited without permission.

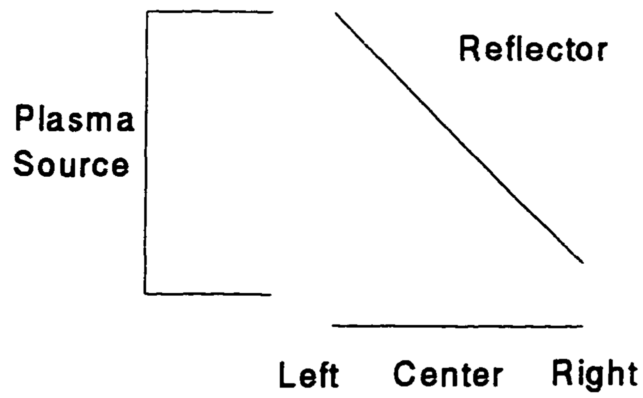

Figure 3.23: Positions on wafer for 2-D determination of angular distributions.

Reproduced with permission of the copyright owner. Further reproduction prohibited without permission.

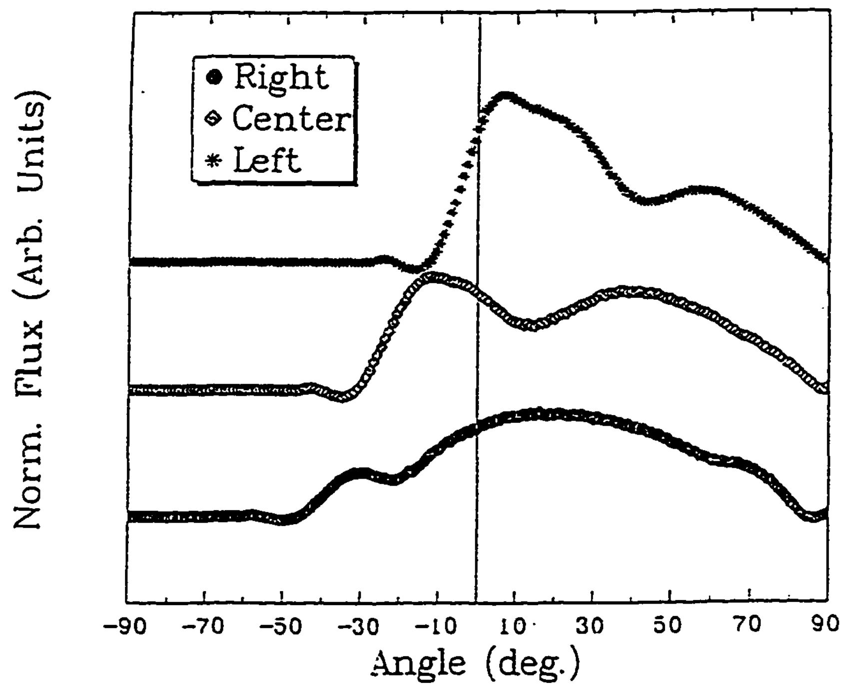

Figure 3.24: Angular distributions for the case of Fig. 3.18. Positions are denoted Left, Center, and Right in accordance with Fig. 3.23. Note the apparent trade-off between distance from the wafer and source density in determining wafer uniformity.

Reproduced with permission of the copyright owner. Further reproduction prohibited without permission.

The angular distributions will be shown for the uniform cases above. The angular distribution for the case of Fig. 3.18 is shown in Fig. 3.24. The distributions are normalized and smoothed by a 4th order Savitsky method. The negative going peaks on the negative angle side are artifacts of the smoothing and should be ignored. In Fig. 3.24 we see the effect of tuning the source densities for better uniformity. At the leftmost position, denoted by Left in the figure, the distribution is heavily biased to the right, which is the position of the reflector plate. The contribution to the distribution from the higher density in the top source is apparent. There are two peaks due to the difference in average distances from each position to a position on the limiter. The dip in each distribution shows the trade off between proximity to reflector points and density in the source. On the rightmost position, which is very close to the reflector plate, a large broad peak forms at positive angles. At the leftmost position, far from the limiter, the higher source density on the reflector directly above this point dominates the distribution.

In Fig. 3.25 we can see the effect of using the stair step reflector by looking at the angular distributions associated with Fig. 3.22(c). As expected, the distribution is strongly peaked toward the center of the reflector weighted by distance from wafer point and source densities. This is also what one would expect from a point source or a single spatially small, very high density plasma source on a small reflector. Experiments with such a neutral beam source, described by Cuthbertson [11], and in the introduction have been reported [7] which show feature evolution under such a bombardment. In the case of that work, features in the center of the wafer were etched anisotropically, while edge positions showed features sloped due to shadowing of the neutral beam.

Next, the distribution for multi-faceted reflector plates are considered. We show in Fig. 3.26 the angular distributions for the case of Fig. 3.19(b). Here there is one source and 5 facets at various angles (See Fig. 3.19(b) for description). The angular distributions shown in Fig. 3.26 indicate the effect of reflector facets at large angles. A large fraction of the flux is incident at angles of 45° or greater. Nearly all of the flux at the rightmost position

Reproduced with permission of the copyright owner. Further reproduction prohibited without permission.

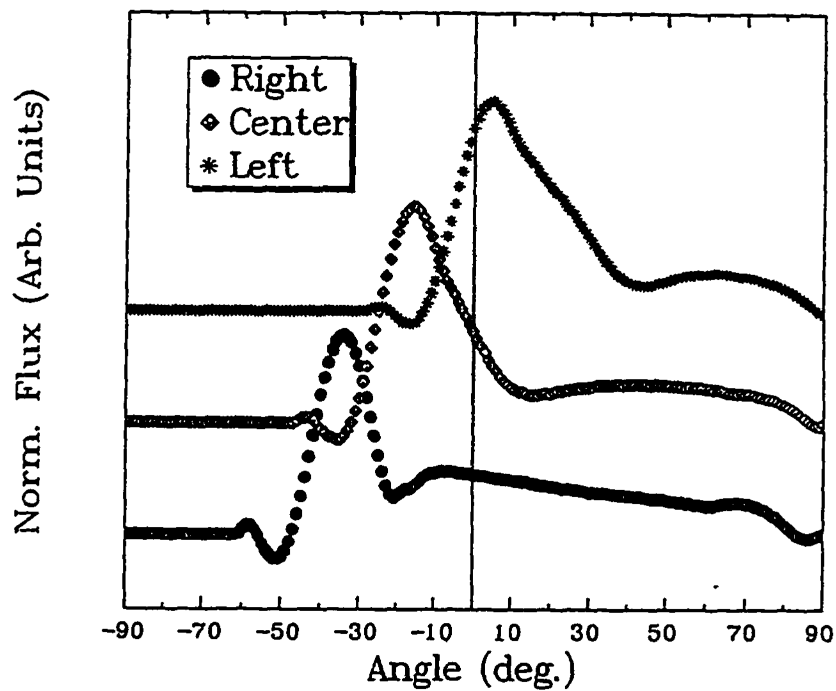

Figure 3.25: Angular distributions for the stair step reflector case of Fig. 3.22(c). The flux is highly directional but weighted towards the center of the reflector.

Reproduced with permission of the copyright owner. Further reproduction prohibited without permission.

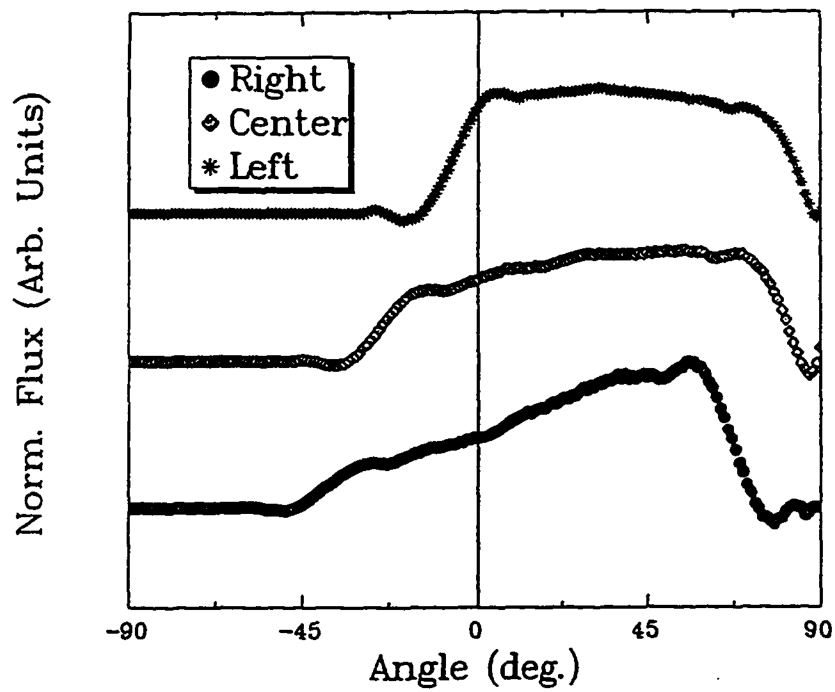

Figure 3.26: Angular distributions for multi-faceted reflector case of Fig. 3.19(b). Note the flux at large angles showing that large reflector angle flux can dominate the isotropy.

Reproduced with permission of the copyright owner. Further reproduction prohibited without permission.

is at a very large angle. The lower reflector facets seem to dominate this distribution. At the leftmost position, the distribution appears isotropic at angles positive with respect to the wafer normal. This effect is due to the near normal emission from the lower, large angle facets and the higher, small angle facets. This can be understood if one considers that the leftmost position is close to the focal point of the limiting quarter-circle formed by the reflector.

2-D Model Conclusions

A 2-d ray-trace model was used to determine the effect of various shapes and source configurations on wafer uniformity and isotropy. It has been shown that multi-source configurations can be tuned to increase uniformity of neutral flux at the wafer surface. The best uniformity achieved by tuning source densities was 2.2% in this section, but even better uniformity may be possible. However, in spite of the 2.2% uniformity, great for a wafer cleaning step, the angular distributions were too non-directional for feature etching.

Two types of reflector plate shaping were considered. The stair step reflector plate shows promise, as it produces a more uniform reflected neutral flux. Angular distributions from such a source show highly directional flux distributions. However, the distributions are not normal to the wafer surface at all points. For the multi-facet case, angular distributions are fairly isotropic on the right side of the wafer normal, but show near-zero fluxes to the left of the wafer normal. Multi-facet reflectors also show poor uniformity compared to the stair step case.

A manifestation of the multi-source technique could be an array of high density sources arranged in either a honeycomb or square configuration as appears in Fig. 3.27.

Reproduced with permission of the copyright owner. Further reproduction prohibited without permission.

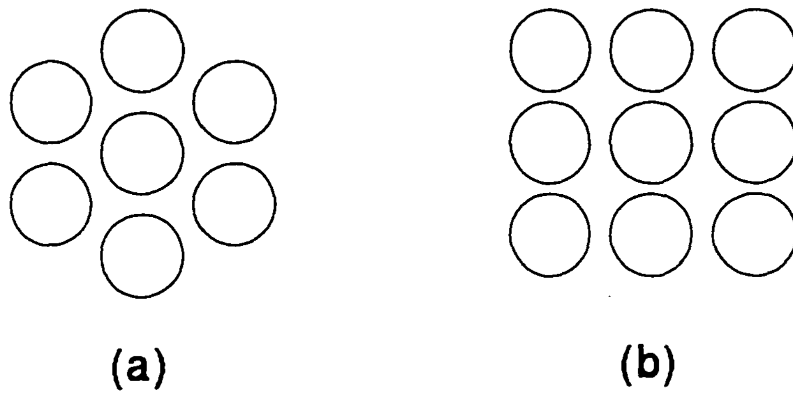

Figure 3.27: Possible 3-D configurations for multiple plasma sources. (a) "Honeycomb" and (b) planar square.

Reproduced with permission of the copyright owner. Further reproduction prohibited without permission.

Chapter 4

Monte Carlo Simulation

4.1 3-D Monte Carlo Simulation

This chapter presents a Monte Carlo simulation of the surface-reflection neutral stream source potentially capable of providing a directed flux of hyperthermal neutrals at tunable energies. This source is based on the surface reflection neutralization [9] of ions which has been used in previous work in studies of low earth orbit atomic oxygen bombardment of spacecraft materials [28] and to etch silylated photoresists with hyperthermal oxygen atoms [7,11]. In this previous work, a high density, lower-hybrid plasma source [29] was used as a source of plasma ions. This source of hyperthermal neutrals was small (plasma radius $\approx$ 2 cm) and was not optimized for large diameter wafer processing. Deployment of the surface neutralization technique to larger wafer sizes ($\geq$ 8″diameter) requires a larger profile plasma source (or a group of small sources).

Fig. 4.1 shows a schematic of the wide aperture neutral stream source. Any high density plasma source, such as an electron cyclotron resonance (ECR) source or transformer coupled plasma (TCP) source, may serve as a source of ions for neutralization. The plasma flows along a weak collimating magnetic field (B $\leq$ 50 Gauss). The ions accelerate across the thin dc sheath at the biased metal reflector plate, where they are neutralized by electron tunneling from the surface and reflect as neutrals. For modeling purposes, the kinetic energy

Reproduced with permission of the copyright owner. Further reproduction prohibited without permission.

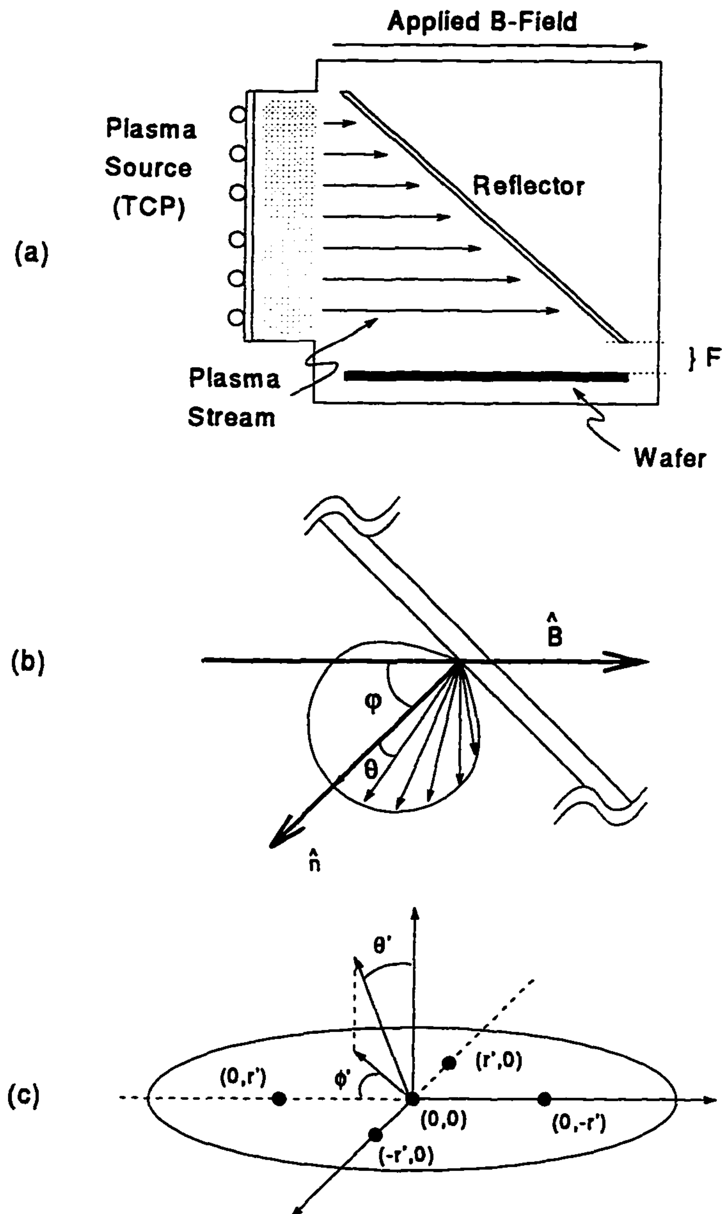

Figure 4.1: (a) Schematic representation of the wide aperture surface reflection neutral stream source. Ions from the plasma flow along collimating B-field lines and reflect from the biased metal plate. (b) Blow up of the angular definitions with respect to the reflector plate normal. (c) Wafer sites used for collection of energy and angular distribution information where $r' = r_o/2 = 5$ cm.

Reproduced with permission of the copyright owner. Further reproduction prohibited without permission.

and angular distributions of the reflected neutrals are represented by parabolic and $\cos^n$ functions, respectively, with a mean reflected kinetic energy $\approx \frac{1}{2}$ to $\frac{1}{3}$ of the bias voltage on the reflector plate. These choices are made in accord with earlier fundamental studies of these processes [11].

The resulting neutral atom stream traverses chamber distances up to 20 cm or more through the background neutral gas and plasma, subjected to loss by elastic scattering, charge exchange and ionization. Electron impact on the molecular background can give rise to Frank-Condon production of low energy ($E \leq 10$ eV) atoms with random angular orientation, diminishing beam directionality.

Processing characteristics of such a neutral stream source are very dependent on the energy and angular distribution striking the wafer. Though creating a uniform total fluence is highly desirable for low energy processes, the degree of uniformity need not be as high as that required by high energy ion processing. For the projected applications of low energy, neutral stream etching, long overetch times are made possible by the diminution of damage to underlying layers.

A discussion of the particular modeling methods used and the parameter space of the model appears below. The goal is to simulate a number of possible combinations of materials, plasma profiles and pressures that may be necessary to provide the required neutral stream in such a reactor.

4.2 Description of Model

We use a Monte Carlo method to simulate the transport of hyperthermal neutrals in the surface reflection source. The model assumes time-independent plasma density spatial profiles. The plasma density at the biased metal reflector plate is used to determine the relative probability for launching a neutral. Energy and angular distributions are input parameters of the model based on experimental observations [11]. In this section we describe the assumptions and the Monte Carlo method used in the simulation.

Reproduced with permission of the copyright owner. Further reproduction prohibited without permission.

Particles are launched from the reflector plate using a sampling procedure meant to reproduce the true density distribution at the reflector. The 2-d density matrix at a position just outside of the reflector sheath is given by the full 3-d plasma density matrix assumed in our description of the transport of the plasma along the collimating magnetic field. The model plasma density profiles are discussed below. The density matrix at the reflector is denoted by $D'(x', y')$ where x' and y' are local coordinates on the reflector. We define a matrix of integers

$$k(x', y') = \mathrm{int}\left(\frac{D'(x', y')}{\min(D'(x', y'))}\right) \tag{4.1}$$

where $\min(D'(x', y'))$ is the minimum density at the reflector plate and "int" represents the integer rounding function. The coordinates of successive launch locations, x', y', are selected at random on the reflector plate. A number of particles equal to $k(x', y')$ are launched from that position with angles and energies selected as described below. This procedure insures that the distribution of launched particles is consistent with the ion density distribution at the reflector.

The angular distribution of launched particles is assumed to be of the form $f(\theta) = N_\theta \cos^{n_\theta}(\theta)$ where N_θ is a normalization constant, n_θ is the degree of the angular distribution, and θ is the launch angle with respect to the reflector normal. Fig. 4.1(b) shows the definitions of θ, and ϕ, the angles between the reflector normal and the applied B-field.

Fig. 4.2 shows the angular emission profiles used in this work. The angular distributions of reflected neutrals vary depending on the material of the reflector and the particular ion used as the neutral precursor. These values of n_θ (0.8, 1.3, and 2.1) have been determined through surface reflection experiments by Cuthbertson [11]. In general, we use the value of 1.3 for most simulations, although the effect of variations are discussed later in this Chapter.

Reflected neutral energies are sampled from an energy distribution of the form

$$f(E) = N_E\left[1 - \left(\frac{E - E_c}{E_w}\right)^2\right]^{n_E} \tag{4.2}$$

where E is the neutral energy in eV, N_E is a normalization constant, E_c is the mean launch energy, E_w is the width of the energy distribution at the base, and n_E is the degree of the

Reproduced with permission of the copyright owner. Further reproduction prohibited without permission.

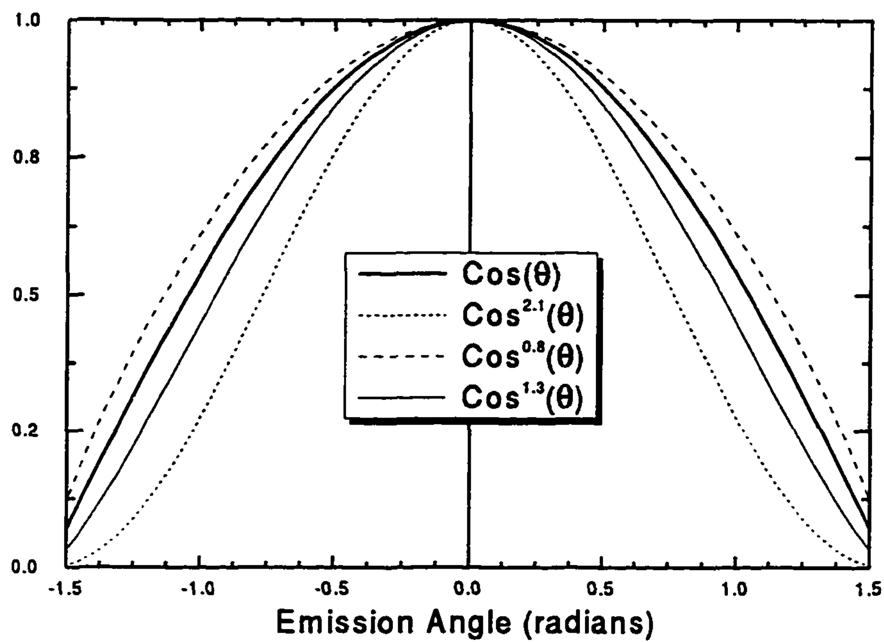

Figure 4.2: Cosine emission distributions used in this work.

Reproduced with permission of the copyright owner. Further reproduction prohibited without permission.

energy distribution. This functional form is chosen for its ability to represent a wide range of experimentally observed distributions. E_c is determined from the applied reflector bias and the neutral energy reflection coefficient r_b, which varies depending on the particular reflector material/feedstock gas combination used. Cuthbertson [11] has measured the parameters r_b and n_θ for a variety of material combinations of interest. Those measurements also include resulting energy distributions allowing determination of representative n_E values. The angle and energy of each launched particle is determined from the above distributions using importance sampling [30, 31].

E_{bias} (eV)	r_b	FWHM (eV)
47	0.319	6
35	0.375	7
23	0.435	8

Table 4.1: Energy reflection data used in the simulations. $E_{\rm bias} = -e(V_{\rm plate} - V_{\rm plasma})$ represents the kinetic energy of ions incident on reflector plate. The energy reflection coefficient, $r_b = E_{\rm inc}/E_{\rm bias}$, where $E_{\rm inc}$ = energy retained by neutral following reflection. Data for $E_{\rm bias} = 35$ eV was used for simulation shown in Fig. 4.9. Taken from Cuthbertson [11].

A primary motivation for the plasma model is to simulate the effect of the plasma density and temperature profiles on the hyperthermal neutral transport. Ionization of the fast neutrals and charge exchange losses to the plasma stream can be important for high plasma density. Thus there is a trade-off between a sufficient density at the reflector plate to provide substantial neutral flux and the ability of the reflected neutral stream to traverse the plasma.

The cross sections for charge exchange and elastic collisions in argon were obtained from Cramer [32], fitted by the forms:

$$\sigma_{\rm c-x} = 51.9E^{-0.152} \tag{4.3}$$

$$\sigma_{\rm elas} = 41.9E^{-0.138} \tag{4.4}$$

where E is the neutral energy and the cross sections are in units of 10^{-16} cm^2. In order to remove the singularity at E=0 for these particular fits, we approximate for $E \leq 1$ eV,

Reproduced with permission of the copyright owner. Further reproduction prohibited without permission.

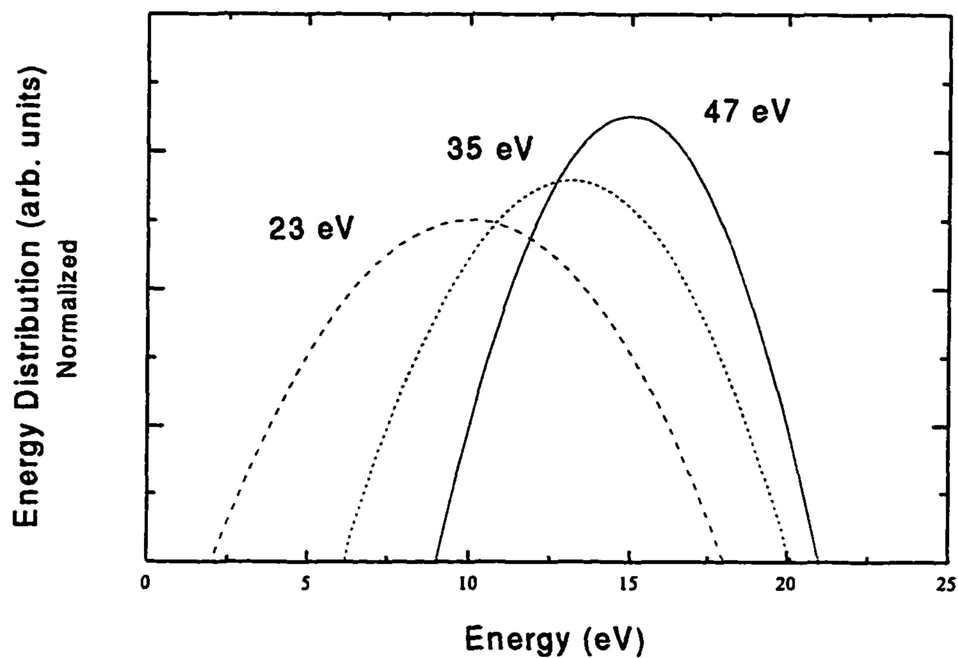

Figure 4.3: Energy distributions as launched from the reflector plate. The quoted energies are the kinetic energy of the ions as they strike the plate. This value is related to the plate bias by $E_{bias} = -e(V_{plate} - V_{plasma})$. See Table 4.1 for the parameters used to determine these distributions.

Reproduced with permission of the copyright owner. Further reproduction prohibited without permission.

$\sigma_{c-x} = 51.9 \times 10^{-16}$ cm^2 and $\sigma_{elas} = 41.9 \times 10^{-16}$ cm^2. While such a constant low energy cross-section for argon modeling is justifiable, extension to free-radical atoms which undergo fast recombination at low energy, or electronegative species which capture electrons to form negative ions, require different treatment below 1 eV.

The probability array is constructed from the relative collision frequencies of each process under consideration (elastic, charge-exchange, ionization) as a function of energy [33, 34]

$$P_{i,j} = \sum_{j}^{N} \frac{\nu_{i,j}}{\nu_{max}} + \frac{\nu_{max} - \nu_{i_{max}}}{\nu_{max}} \tag{4.5}$$

where i = energy index, j = process index, N = number of processes, $\nu_{i,j}$ is the collision frequency for the jth process at energy i, $\nu_{i_{max}}$ is the maximum collision frequency at energy i, $\nu_{i_{max}} = \sum_{j=1}^{N} \nu_{i,j}$ and ν_{max} is the maximum collision frequency over the entire energy range. The added term, $(\nu_{max} - \nu_{i_{max}})/\nu_{max}$, is meant to allow for the possibility of a "null" collision, that is, an "event" which does not alter the identity, position, or momentum of the reflected neutral, by normalizing with respect to the maximum collision frequency such that $P_{i,N'} = 1$ where N' includes the "null" collision process.

To compute the probability for ionization, we use a procedure previously used by Weng and Kushner [33] that eliminates the need to calculate ionization frequencies at each computational cell in the plasma volume. In this procedure, the probability array is calculated from the relative collision frequencies of each process under consideration (elastic, charge-exchange, ionization) as a function of energy [33, 34]. The constant array element for ionizing collisions is calculated from the maximum energy and temperature in the plasma stream. If a random collision event leads to an ionizing collision, a second random number is compared to the ratio of density at the current position and the maximum density, $n(x, y, z)/n_{max}$. If this ratio is less than the selected random number, no ionization occurs, otherwise, the neutral is lost to the plasma by ionization.

Ionization probabilities are calculated from the second order ionization rate constant

Reproduced with permission of the copyright owner. Further reproduction prohibited without permission.

of argon [13]

$$\nu_{ion} = 1.2 \times 10^{-7}[\mathrm{cm}^3/\mathrm{s}]n_{\mathrm{max}}[cm^{-3}]e^{-\frac{18.6}{T_{\mathrm{max}}[eV]}} \tag{4.6}$$

where ν_{ion} is the ionization collision frequency in units of s^{-1}, and n_{max} is the maximum electron density which the neutral may encounter. T_{max} is the temperature of the plasma at the maximum density position.

The general plasma profile has the form

$$n(r,z) = n_o\Big(1 - (\frac{z}{L(x,y)})^2\Big)^{n_l}\Big(1 - (\frac{r-r'}{r_o})^2\Big)^{n_r} \tag{4.7}$$

where n_o is the maximum density defined at $z = 0$ (see Fig. 4.1), n_r and n_l are radial and axial shape parameters, which are sensitive to the balance between volume ionization and the volume and surface losses from the source to the reflector, and r' is the radius of the power deposition toroid from a confined TCP ($r' = 0$ for ECR) [24]. R and $L(x,y)$ are the radius and length of the plasma column, where the dependence of L on the x, y projection into the plasma source plane, $z = 0$, is shown. This dependence arises from the reflector/applied B-field angle. A similar form is used for the electron temperature profile, although the temperature profile shows little effect on the resulting energetic neutral flux at the wafer. The flexibility of this form permits representation of a wide range of possible sources. For simplicity, the magnetic field is assumed uniform in the z direction, throughout the plasma volume. Electrons can be confined to flow along field lines readily; however, radial ion losses known to exist in magnetized plasmas [35] may contribute a substantial charge flux to the wafer.

The parameters n_r and n_l are determined based on power and particle balance similar to the prescription described by Lee and Lieberman [13] and Lieberman and Gottscho [35]. In these works, power deposited in the volume is balanced by surface recombination and excitation losses and is related to the bulk plasma density and geometry by

$$P_{\mathrm{abs}} = en_o u_B A_{\mathrm{eff}} \epsilon_L \tag{4.8}$$

Reproduced with permission of the copyright owner. Further reproduction prohibited without permission.

where n_o is the bulk plasma density, u_B is the Bohm velocity, ϵ_L is the energy lost from the plasma due to bulk ionization and wall ion/electron recombination. $A_{\text{eff}} = \pi {r_o}^2(1+\sec\phi)h_L$, where ϕ is the angle between the reflector normal and the applied B-field, and $h_L = n_s/n_o$ is the ratio of sheath edge density and bulk plasma density. The effective loss area is constrained to the ends of the plasma column by the applied B-field. The loss area consists of the circular area at the source end of the column and the ellipse formed by the reflector plate (approximately 50 Gauss). In order to prevent the major-axis of the reflector plate becoming excessively large, it is constrained to a maximum length of $r_o \sec(45^o)$.

In the pressure regime of interest, the ion mean free path, $\xi_i \leq r_o, L$, so the profile parameters can be determined by relating the sheath edge density to the bulk density via [14]

$$h_r \equiv \frac{n_{sR}}{n_o} \approx 0.8\left(4+\frac{R}{\xi_i}\right)^{-\frac{1}{2}} \tag{4.9}$$

$$h_L \equiv \frac{n_{sL}}{n_o} \approx 0.86\left(3+\frac{L(x,y)}{2\xi_i}\right)^{-\frac{1}{2}} \tag{4.10}$$

where ξ_i is the ion mean free path. The values for n_r and n_l are then found by matching the condition of eqns. 4.9 and 4.10 to that of eqn. 4.7.

From the above plasma model, densities of approximately 10^{12} cm^{-3} are found at 1000 W. Densities at the reflector plate at the same power are on the order of 1×10^{11} cm^{-3}. Langmuir probe measurements of the experimental device show behavior consistent with the model. A detailed comparison of the model to experimental results will be given in Chapter 4.

The simulation flowchart is shown in Fig. 4.4. Input parameters are given, including input power, pressure, and reflection parameters such as the degree of reflected angular and energy distributions. From these, the angular and energy distributions, plasma profile, reflector plate matrix (see eqn. 4.1), and probability matrix (see eqn. 4.5) are constructed.

Once all relevant distributions are computed, the simulation begins by selecting a site on the reflector plate and determining the number of particles to launch from that position. After launching a particle, with initial velocity, $\vec{V} = \vec{V}_{in}$, chosen at random, consistent with

Reproduced with permission of the copyright owner. Further reproduction prohibited without permission.

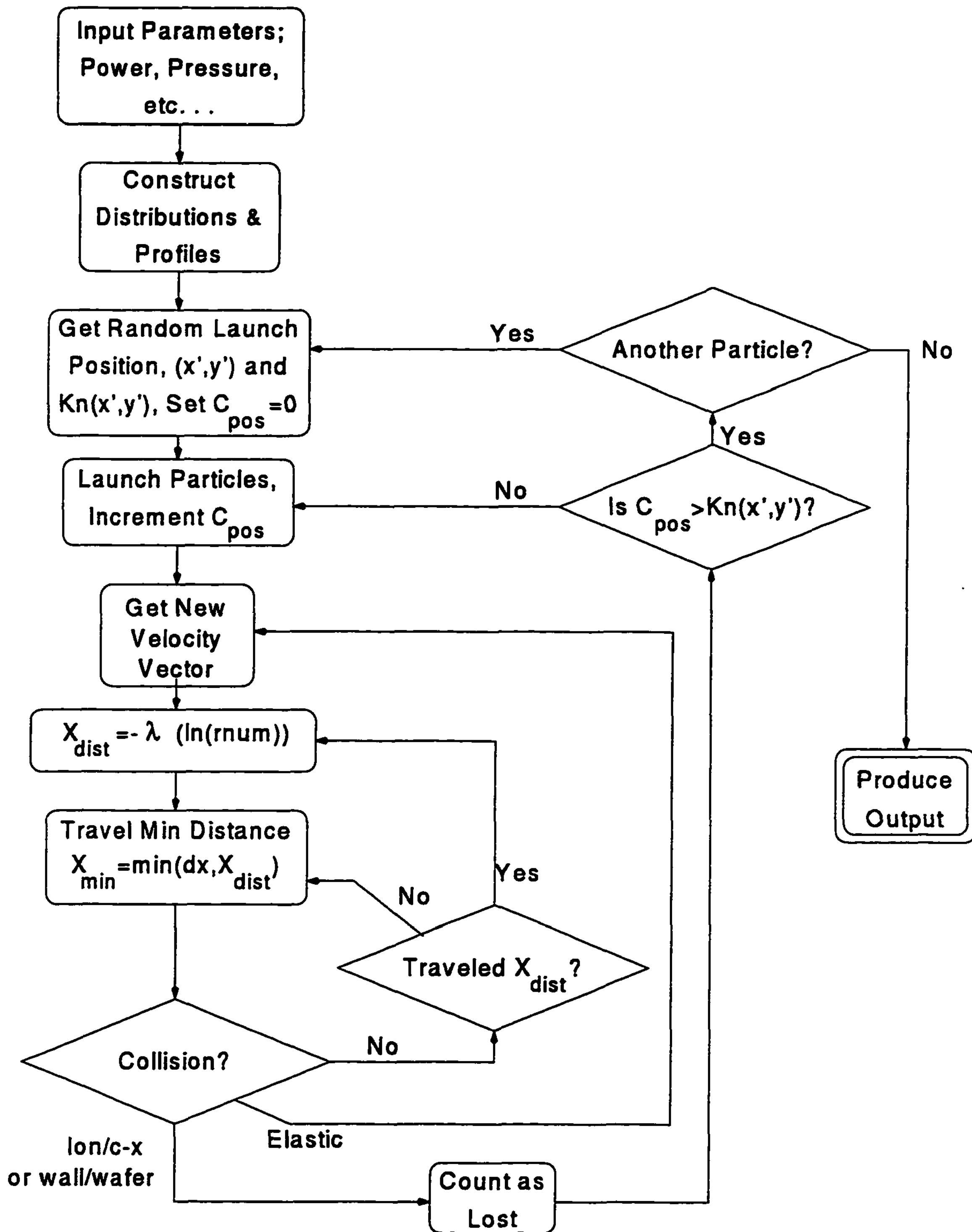

Figure 4.4: Flowchart of Monte Carlo simulation

Reproduced with permission of the copyright owner. Further reproduction prohibited without permission.

the angular and energy distributions constructed earlier, the distance to the next collision is computed from

$$x_{\text{dist}} = -\lambda \ln(rnum) \tag{4.11}$$

where λ is the mean free path for the neutral determined from eqns. 4.3 and 4.6 , and $rnum$ is a random number. The particle is allowed to traverse a minimum distance, $\mathrm{x_{min}} = \min(\mathrm{dx}, \mathrm{x_{dist}})$, in the direction defined by $\hat{V} = \vec{V} / |\vec{V}|$, where dx is the width of one computational cell.

The simulation then determines if there is to be a collision at the new position by comparing a new random number, $rnum$, to the probability matrix defined by eqn. 4.5, assigning a collision of type j according to $P_{i,j} < \mathrm{rnum} \leq P_{i,j+1}$. If no collision occurs, the particle continues at its original velocity in increments of x_{min} until it has traversed x_{dist}.

When an elastic collision is selected, a new velocity vector is chosen based on conservation of energy and momentum. For the energy dependent hard-sphere approximation used in this model, the distribution of center-of-mass scattering angles can be sampled using

$$\psi_{\text{cm}} = \arccos(1 - 2(rnum)) \tag{4.12}$$

where ψ_{cm} is the center-of-mass scattering angle and $rnum$ is a new random number [36].

The corresponding scattering angle in the lab frame is given by

$$\cos\psi_{\text{lab}} = \frac{1 + (m_{\text{bk}}/m_{\text{inc}})\cos\psi_{\text{cm}}}{(1 + (m_{\text{bk}}/m_{\text{inc}})^2 + 2(m_{\text{bk}}/m_{\text{inc}})\cos\psi_{\text{cm}})^{1/2}} \tag{4.13}$$

where m_{inc} and m_{bk} are the masses of the neutral and background species, respectively. The azimuthal angle is distributed isotropically and found by $\Phi = 2\pi(rnum2)$, where $rnum2$ is a random number. The degree of incident energy loss is given by

$$\frac{E_o - E_f}{E_o} = \frac{2m_{\text{inc}}m_{\text{bk}}}{(m_{\text{inc}} + m_{\text{bk}})^2}(1 - \cos\psi_{\text{cm}}) \tag{4.14}$$

where E_f is the final energy and E_o is the incident energy [31]. In this argon model, $m_{\text{inc}} = m_{\text{bk}}$, so eqns. 4.12, 4.13, and 4.14 reduce to the simple forms $\cos\psi_{\text{lab}} = (rnum)^{1/2}$ and $E_f = (1 - rnum)E_o$, where rnum is the same random number for both.

Reproduced with permission of the copyright owner. Further reproduction prohibited without permission.

Instead of elastic collisions, other possible interactions are wafer strikes, ionization or charge exchange, or collision with walls. For ionization or charge-exchange, the neutral is assumed lost to the plasma. Particles are assumed lost at wall surfaces due to molecular recombination or thermalization. Recycling of recombined, thermalized gas has not been included in these calculations. For a wafer strike, statistics are kept at every position on total number of particle strikes. Angular and energy distributions are kept at five locations (shown in Fig. 4.1(c)) on the wafer to determine the spatial variation of these distributions. After a "loss" collision, the simulation launches another particle, continuing the above cycle until the required number of particles are completed.

The pressure, plasma density, and ion/neutral reflection parameters are the primary parameters varied here to assess the performance of this source design.

4.3 Results and Discussion

Table 4.2 gives the ranges of the parameter space explored in this source. Pressure variation will have a strong effect on reflected neutral stream loss and cooling due to elastic scattering. However, lowering the pressure to assure the highest possible reflected neutral transmission also lowers the plasma density, which can result in a net reduction of reflected neutral flux at the wafer. This trade off is explored below.

Parameter	Value(s)
Wafer Radius	10 cm
Reflector Angle	$35^o - 55^o$
Pressure [mTorr]	1.0 - 10.0
Cosine Emission (n_θ)	0.8 - 2.1
Reflector Bias [Volts]	-10 - -30

Table 4.2: General parameter space of device. Reflection degree, n_θ, defines the angular distribution ($\cos^n(\theta)$) of neutrals reflected from the plate. Reflector bias determines the incoming ion energy, $E = -e(V_{\text{plate}} - V_{\text{plasma}})$. Reflector angle is the angle between the plate surface normal and applied B-field.

Reproduced with permission of the copyright owner. Further reproduction prohibited without permission.

Plate Angle Variation

In Fig. 4.5 we see the general peaked structure of the neutral flux at the wafer. All of the simulations showed this behavior to some degree. Varying the reflector angle, ϕ, allows control over the peak position, but has little effect on overall uniformity, which tends to vary only in the range 42% to 70% although a uniformity minimum appears to be obtained at a reflector angle of 45° as discussed below. The "peakedness" of the profile is a direct result of the trade-off between plasma flux at the reflector and elastic losses to the background. Generally the peak is at the wafer position closest to the reflector plate. Flux originating at the "high" end of the reflector (closest to the plasma) must traverse a greater connection length to make a contribution at the wafer. So, while the position of the peak is somewhat controllable, the peak flux originates at points nearest the wafer.

Angular statistics were kept for each of the positions shown in Fig. 4.1(c), including angles of incidence, θ' and ϕ', and the energy-averaged angles of incidence, $< \theta' >$ and $< \phi' >$. Of primary importance in anisotropy control is the θ' distribution, a representative example of which appears in Fig. 4.6(a). Due to gas scattering effects the θ' distributions are not sharply peaked, but do show a strong dependence on the reflector/B-field angle, ϕ, discussed earlier. The azimuthal angle of incidence, ϕ', shows (Fig. 4.6(b)) that the majority of neutrals are incident from the general direction of the reflector plate, falling between 90° and 270° with a strong peak at 180° due to the symmetry of the system.

The energy-averaged angle of incidence, $< \theta' >$, as a function of reflector angle, ϕ appears in Fig. 4.7. This behavior can be understood by comparing to Fig. 4.5. As ϕ decreases ($\phi \approx 35^o$), the near-reflector wafer positions (site (0,-r') in Fig. 4.1(c)) see near-normal reflected neutral flux. This behavior is consistent, but not as profound, for the other wafer positions. As ϕ is increased, the angular distributions converge to complementary behavior. The uniformity is also plotted in Fig. 4.7 to show the effect of varying ϕ. A minimum in uniformity appears near 45°.

Further comparison between the uniformity of Fig. 4.7 and the wafer flux map of

Reproduced with permission of the copyright owner. Further reproduction prohibited without permission.

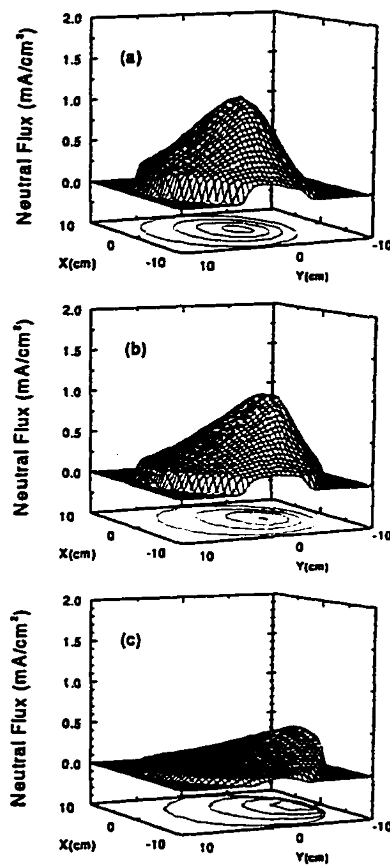

Figure 4.5: 3-D flux maps at various reflector/B-field angles. (a) 35°, (b) 45°, (c) 55°. Parameters: power = 1000 watts, pressure = 1.0 mTorr, reflector-wafer distance F = 3 cm.

Reproduced with permission of the copyright owner. Further reproduction prohibited without permission.

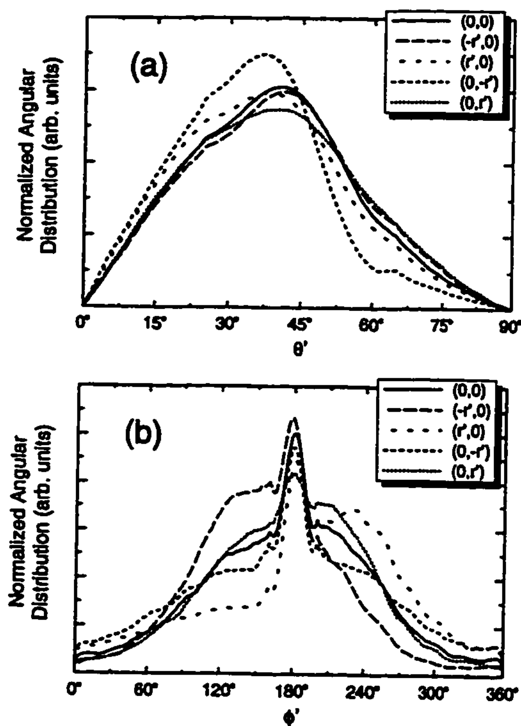

Figure 4.6: Representative angular distributions. (a) θ', (b) φ'. See Fig. 4.1(c) for angular definitions. Parameters are pressure = 1 mTorr, power = 1000 watts, ϕ = 45°, distance = 3 cm.

Reproduced with permission of the copyright owner. Further reproduction prohibited without permission.

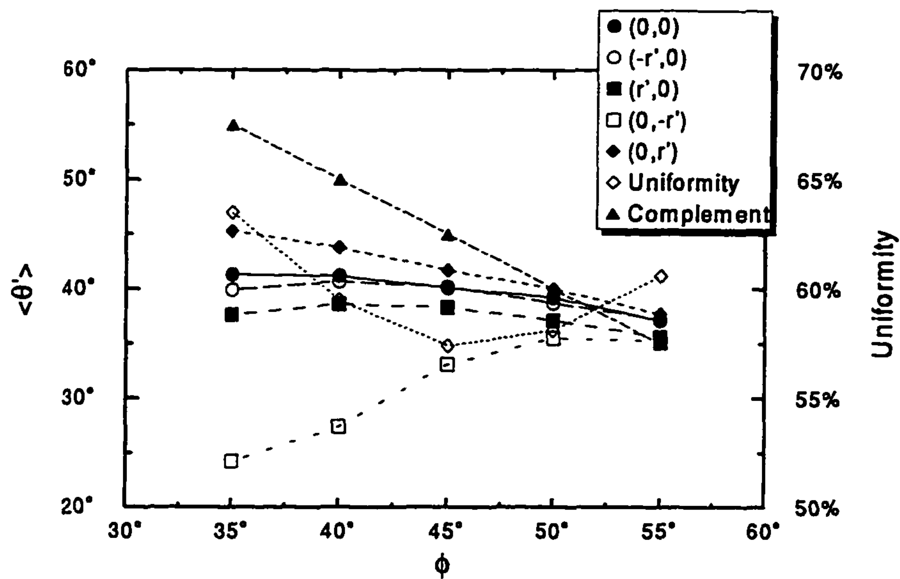

Figure 4.7: Energy-averaged θ' as a function of reflector angle, ϕ. The complement of ϕ is plotted for comparison. Uniformity of total wafer flux is also shown. Note the minimum in uniformity at 45°.

Reproduced with permission of the copyright owner. Further reproduction prohibited without permission.

Fig. 4.5(b) suggests that for the geometry currently under consideration, a reflector angle of 45° appears best for maximizing flux and uniformity. Although the flux is strongly peaked, this angle shows a uniform average background component of flux over the 8″ wafer. This behavior is important in deciding potential cleaning or etching applications.

The non-directionality of the reflected neutral flux is apparent from the angular distributions in Fig. 4.6. For a feature delineation step in semiconductor processing, the flux must be highly directional to prevent undercutting. It is clear that the current geometry studied here will be unable to provide the necessary directionality for such a step. However, much of the charge-induced damage that we are trying to minimize occurs at the endpoint of the etch. At this point, much of the feature has already been formed. Thus a neutral-based etch step could complete the process in the last 10%, while not requiring a highly directional flux. This proposed process may add a few steps to the production process, but if high improvements in yield are realized, the added cost will be minimal.

Pressure Effects

We know from the 3-D ray-trace model that keeping the pressure low is very important for reflected neutral delivery to the wafer. The effect of increased pressure (from the Monte Carlo model) on the wafer flux appears in Fig. 4.8. Fig. 4.8(a) shows the 45° case of 1.0 mTorr from Fig. 4.5(b). All the simulations of Fig. 4.8 are at a reflector angle of 45°. We note that in going from 1.0 mTorr to 5.0 mTorr (Fig. 4.8(b), the reflected neutral flux is reduced by more than a factor of two. A further reduction by a factor of two is presented at 10 mTorr, shown in Fig 4.8(c). The effect of higher pressure on the energy distribution of reflected neutrals at the wafer will be discussed below.

The fluxes realized in this model highlight the differences in the ray-trace model and the Monte Carlo model. In the ray-trace model, fluxes are assumed reduced by the exponential factor of eqn. 3.12. This assumption is poor because it does not account for low energy, small angle elastic collisions between reflected neutrals and the background gas. In the Monte Carlo

Reproduced with permission of the copyright owner. Further reproduction prohibited without permission.

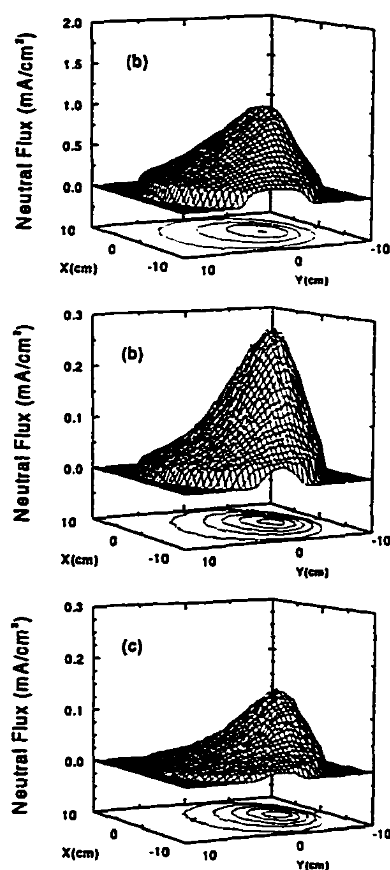

Figure 4.8: Pressure effects on neutral flux. (a) 1.0 mTorr, (b) 5.0 mTorr, (c) 10 mTorr. As pressure is increased, the neutral flux is attenuated by thermalization and randomization. (b) and (c) are not to the same scale as (a) for easy of viewing.

Reproduced with permission of the copyright owner. Further reproduction prohibited without permission.

model, particles are followed through many collisions until they are thermalized, strike the walls, or strike the wafer. Because many of these interactions will be at small angles, where little kinetic energy is lost, the fluxes will be much higher than those of the simple ray-trace model.

The ability of high energy neutrals (10 to 100 eV) to drive through the background gas has been known for some time. It presents a particular problem in the deposition of metal films by magnetron sputtering. These neutrals bombarding a growing film can cause stress and microstructure variations that are detrimental to desired film properties [37–40].

Energy Distributions - Pressure Effects

For the etching or cleaning of semiconductor materials with energetic neutrals, tunability of the energy spectrum is a primary consideration. Table 4.1 shows the values used for energy reflection coefficient, $r_b = E_{\text{inc}}/E_{\text{bias}}$ where $E_{\text{bias}} = -e(V_{\text{bias}} - V_{\text{plasma}})$ is the energy gained in acceleration across the plate sheath and E_{inc} is the peak energy of the launched distribution as in eqn. 4.2. These values were taken from Cuthbertson [11] for argon ions incident upon tantalum.

Energy distributions at several positions on the wafer are recorded for each simulation. Fig. 4.9 shows normalized energy distributions as a function of position (see Fig. 4.1(c)) for typical operating conditions (power = 1000 W, pressure = 1 mTorr) compared to the shape of the energy distribution as launched from the reflector. The launched distribution is a parabola of the form shown in eqn. 4.2, using data for $E_{bias} = 35$ eV in Table 4.1 and shown in Fig. 4.3. These energy distributions have been cooled substantially by interactions with the thermal background. Note that the position closest to the reflector plate retains some of the character of the launched distribution while other positions, farther from the average center of the reflector, have depleted most of the high-energy end of the distribution. Distributions measured by Cuthbertson show behavior more consistent with the launched distribution in Fig. 4.9 because that work was done using a pulsed plasma at much lower pressure [11, 19].

Reproduced with permission of the copyright owner. Further reproduction prohibited without permission.

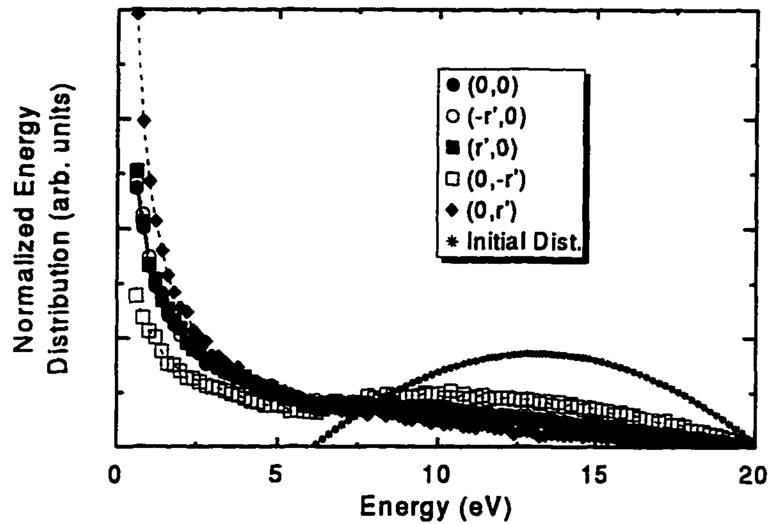

Figure 4.9: Typical normalized energy distributions at the five wafer sites as shown in Fig. 4.1(c). Pressure = 1 mTorr, power = 1000 watts, ϕ = 45°, E_{bias} = 35 eV, r_b = 0.375, FWHM = 7 eV, n = 1.3. The energy distribution of particles as launched from the reflector plate is shown for comparison.

Reproduced with permission of the copyright owner. Further reproduction prohibited without permission.

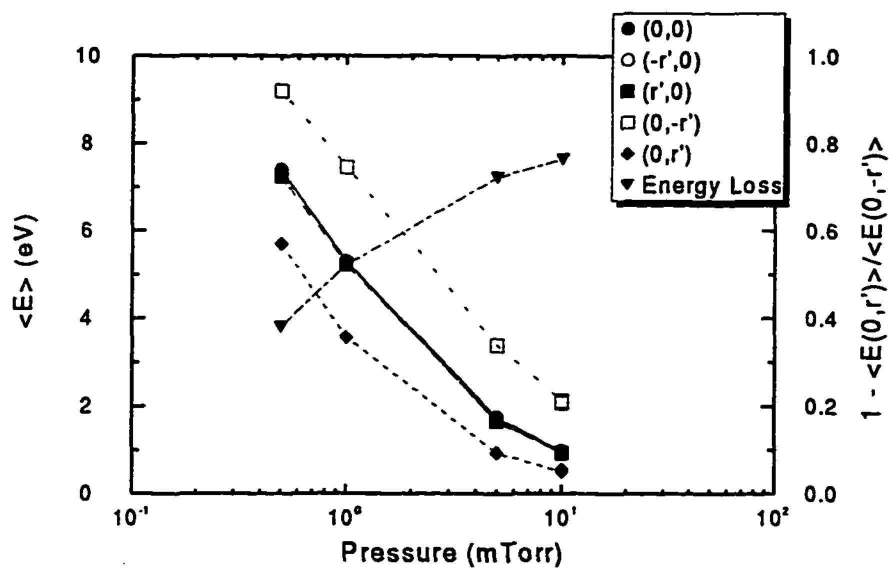

Figure 4.10: Average energy at wafer positions vs. pressure. The general cooling of the stream by interactions with the thermal background is shown. The energy loss difference between the two wafer sites with most difference in connection length increases with pressure as seen by the fractional energy loss, $1 - (< E(0, r') > / < E(0, -r') >)$.

Reproduced with permission of the copyright owner. Further reproduction prohibited without permission.

Fig. 4.10 gives the average energy of the distributions as a function of pressure. We note that the energy decreases with increasing pressure due to cooling of the stream by collisions with the background. The effect of connection length is also seen in Fig. 4.10, where the position farthest from the reflector plate shows a 50% loss in energy as connection length increases at 1 mTorr. The fractional energy loss, defined by $1 - < E(0, r') > / < E(0, -r') >$, describes the ratio of average energies at the farthest point from the reflector to the closest point. This metric is used to show the effect of connection length on the average energy.

Reflector Bias Effects

One of the most important benefits of this neutral stream source is the ability to tune the energy of the stream over a fairly large range. Generally, the reflected neutrals will leave the plate surface with an average kinetic energy approximately 1/2 to 1/3 of its initial energy [18, 19]. However, the tunability of the final stream energy (at the wafer) is limited by interactions with the background gas. This effect is shown in Fig. 4.11 where the average energy of the stream at the wafer is compared to the reflector bias.

The dimunition of the stream energy can be understood by noting that at the energies of interest, the elastic collision cross-sections (see eqn. 4.4) are nearly constant, falling by only 10% over the range of 20 to 40 eV. Further, if the flux of neutrals emitted from the reflector plate does not differ over the energy range (as assumed in this model and seen in other work [18]), the stream should lose roughly the same amount of energy, independent of initial kinetic energy. Thus, doubling the initial energy does not result in a doubling of wafer incident energy. We note, however, that there is some tunability in the energies at the wafer as seen in Fig. 4.11.

Wafer Position Effects

The position of the wafer with respect to the reflector plate is an important parameter as well. Fig. 4.12 shows the effect of moving the wafer away from the reflector plate. The reduction in flux is due to two general effects: elastic collisions with the background, and the

Reproduced with permission of the copyright owner. Further reproduction prohibited without permission.

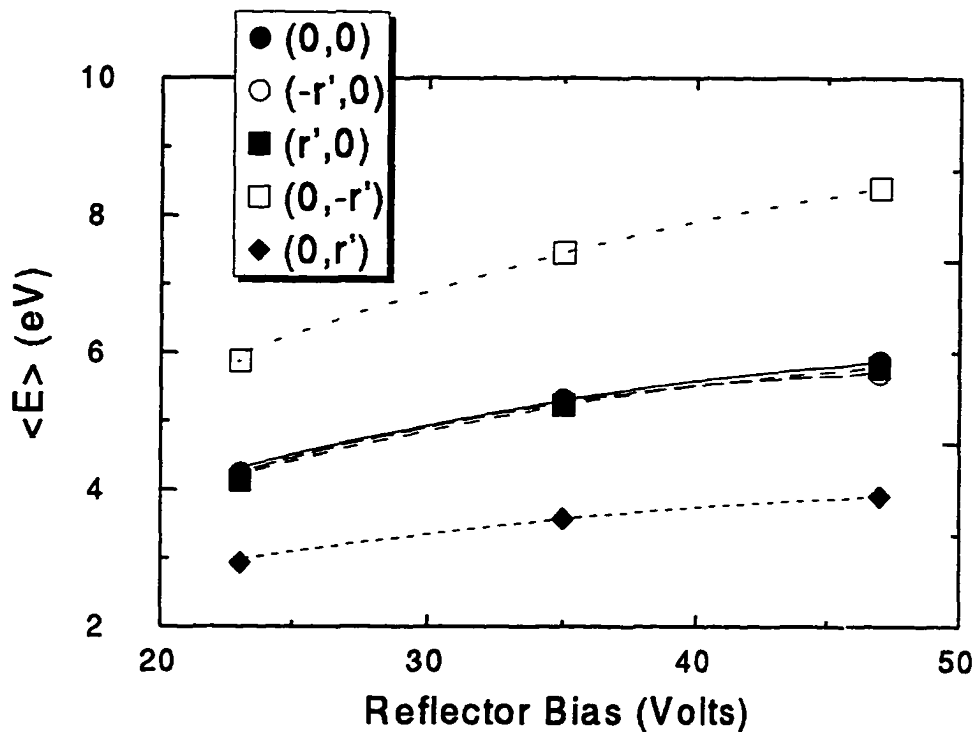

Figure 4.11: Average reflected neutral energy vs. reflector bias. While reflected neutrals tend to maintain 1/2 - 1/3 of their initial kinetic energy on reflection from metal surfaces [18,19], cooling of the stream by interactions with the background bring the average energies much lower.

Reproduced with permission of the copyright owner. Further reproduction prohibited without permission.

$1/r^2$ dependence of flux from each point on the reflector. Moving the wafer away from the reflector is similar in effect as increasing pressure. More distance to travel for the neutrals gives more opportunities to be cooled and randomized by background collisions. However, the flux does become more uniform, suggesting a possible method for increasing etch uniformity if the lower etch rate is acceptable for the process. This effect is largely due to the approximate $1/r^2$ dependence mentioned earlier.

Changing the wafer position has a beneficial effect on directionality. This is seen in Fig. 4.13 where the distribution of θ' is shown for 3 distances from the reflector. This can be understood by noting that as distance is increased, the reflector becomes more like a point source. Because the center of the wafer is directly below the center of the reflector, the neutrals will arrive more normal to the wafer surface.

Etch Rate Predictions

Given the energy distribution at the five diagnostic positions, the etch rates (for hyperthermal oxygen atoms incident on Kapton) can be determined using data obtained by Cross [41], shown in Fig. 4.14. This etch rates can be determined through the relation

$$ER(x, y, E_n) = \Gamma_n(x, y, E_n)\gamma_y(E_n) \tag{4.15}$$

where ER is the position and energy dependent etch rate in cm/sec, Γ_n is the position dependent neutral flux in cm^{-2}-sec^{-1} at a particular reflected neutral energy, and γ_y is the etch yield dependent on the reflected neutral energy, E_n, with units of cm^3/incident-oxygen-neutral. Etch rates are found by integrating eqn. 4.15 over the energy distributions. The angular dependence is not included in the prediction of etch rate although in reality the etch yield is a function of the normal component of neutral kinetic energy [41]. We can estimate the angular reduction in etch rate by the etch rates predicted here multiplying by the cosine of the energy averaged incidence angle, $< \theta' >$, shown in Fig. 4.7.

For determination of etch rates, we assume the argon plasma model will predict the flux of atomic oxygen ions to the reflector plate, thus delivering the same reflected neutral

Reproduced with permission of the copyright owner. Further reproduction prohibited without permission.

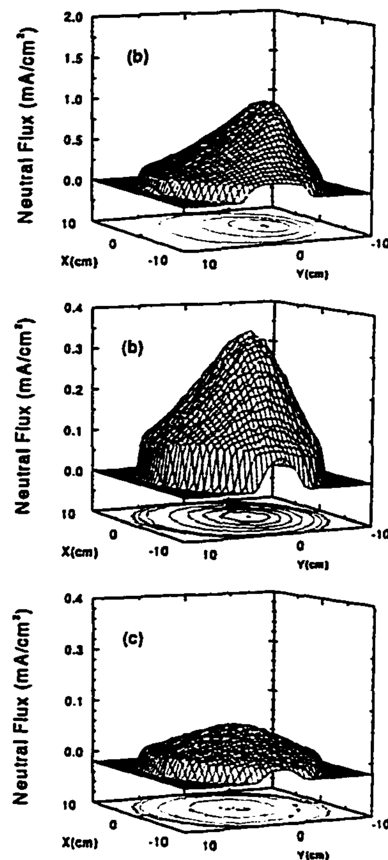

Figure 4.12: Position dependence of neutral flux. (a) 3 cm, (b) 6 cm, (c) 10 cm. As distance from reflector increases, more neutrals are lost to the background by thermalization and randomization. Note the similarity in position effects to pressure effects as seen in Fig. 4.8. (b) and (c) are not to the same scale as (a) for ease of viewing.

Reproduced with permission of the copyright owner. Further reproduction prohibited without permission.

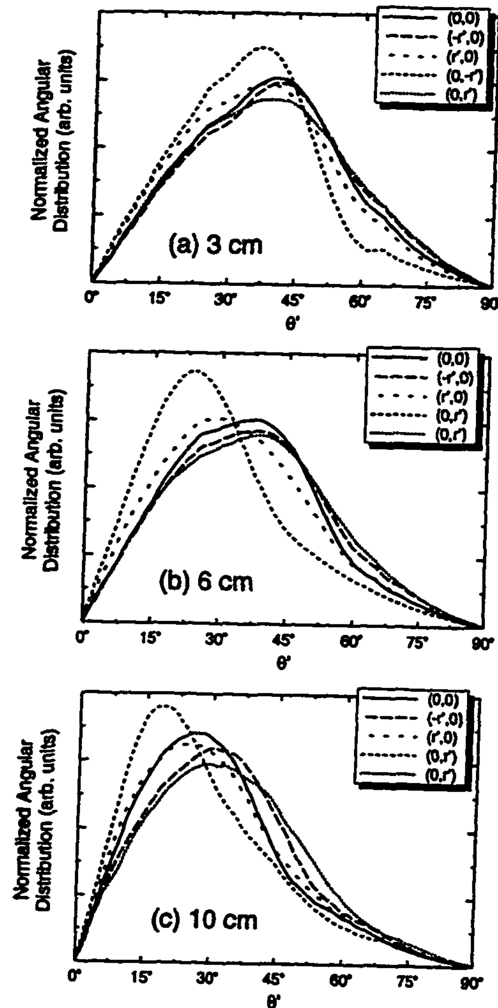

Figure 4.13: Effect of wafer position on angular distributions. Three reflector/wafer distances are shown; (a) 3 cm, (b) 6 cm, and (c) 10 cm. As this distance becomes larger, the reflected neutrals become incident nearer the wafer normal. The requirement for normal or near-normal incidence is important for semiconductor processing.

Reproduced with permission of the copyright owner. Further reproduction prohibited without permission.

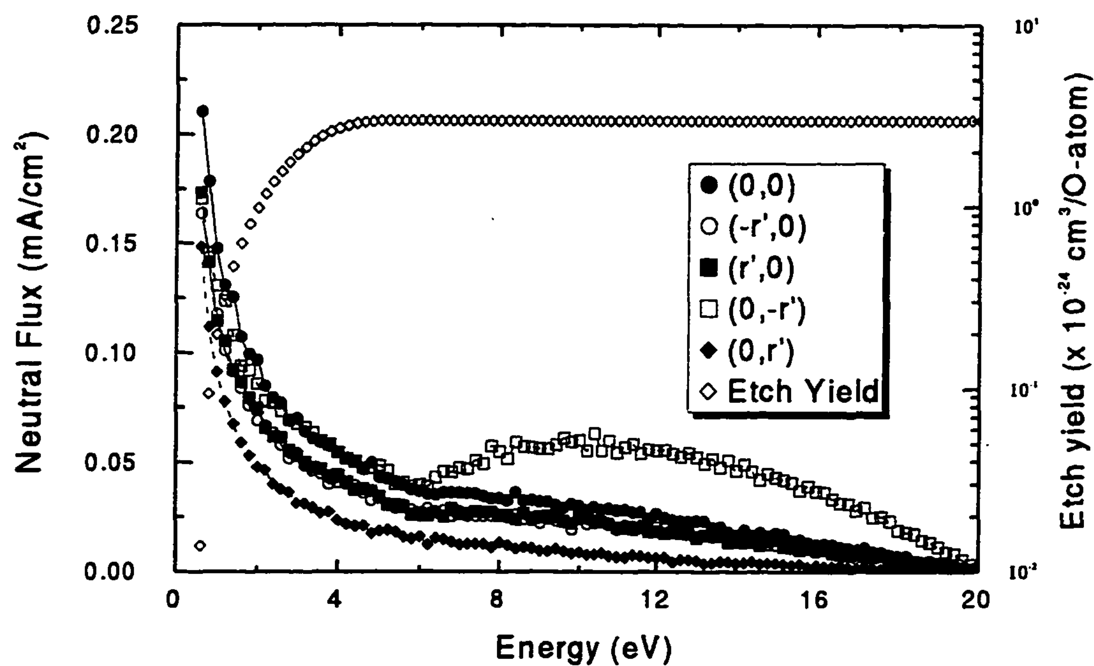

Figure 4.14: Etch yields for hyperthermal oxygen neutrals on Kapton, presented with an non-normalized set of energy distributions [mA/cm^2]. The etch rate is found by integrating eqn. 4.15 over the energy distribution. Etch yields were obtained by Cross [41], used with permission.

Reproduced with permission of the copyright owner. Further reproduction prohibited without permission.

flux. This is not the case in general, but it is expected to provide values within 30% for the powers and pressures used in this work [13,42].

The position dependent etch rates give a better picture of the required overetch times to compensate for any inherent non-uniformities in the neutral flux. According to Cross, etch yields for Oxygen on Kapton rise three orders of magnitude from thermal velocities to 5 eV, where the yields saturate. If the energy of the arriving flux can be maintained above 5 eV, there will be little energy dependence on local etch rate. This can be accomplished, in principle, by keeping pressure low (0.5 - 1 mTorr) and reflector bias high (40 - 50 volts). However, sputtering of the reflector plate at such a high bias, and the resulting wafer contamination, may limit such a method of energy control.

The variation of etch rate with pressure is shown in Fig. 3.17. The reduction in etch rate with pressure is a consequence of reduction in the magnitude of flux and average energy (see Fig. 4.10) due to elastic collisions. The etch rates reported would be suitable for cleaning or "soft-landing" etch steps. It appears from Fig. 3.17 that over-etch steps on the order of 300% could be required. For feature etching, pulsed operation at higher power and lower pressure may be required to achieve etch rates useful for a complete etch step.

4.4 Monte Carlo Conclusions

This model has shown that large fluxes of neutrals are possible using a surface reflection scheme. The magnitude of the flux is limited only by plasma source density and background pressure. Angular distributions and neutral flux uniformity are effected strongly by reflector plate orientation.

Most of the high energy range of the energy distributions have been shown to be depleted as pressure increases. However, lower pressure allows transmission of the higher energy population, and thus an increase in etch rate. The inherent non-uniformities of such a source may be overcome by manipulation of the source geometry. For example, an array of sources directed radially into a reflector assembly, or a rotating magnetic containment of

Reproduced with permission of the copyright owner. Further reproduction prohibited without permission.

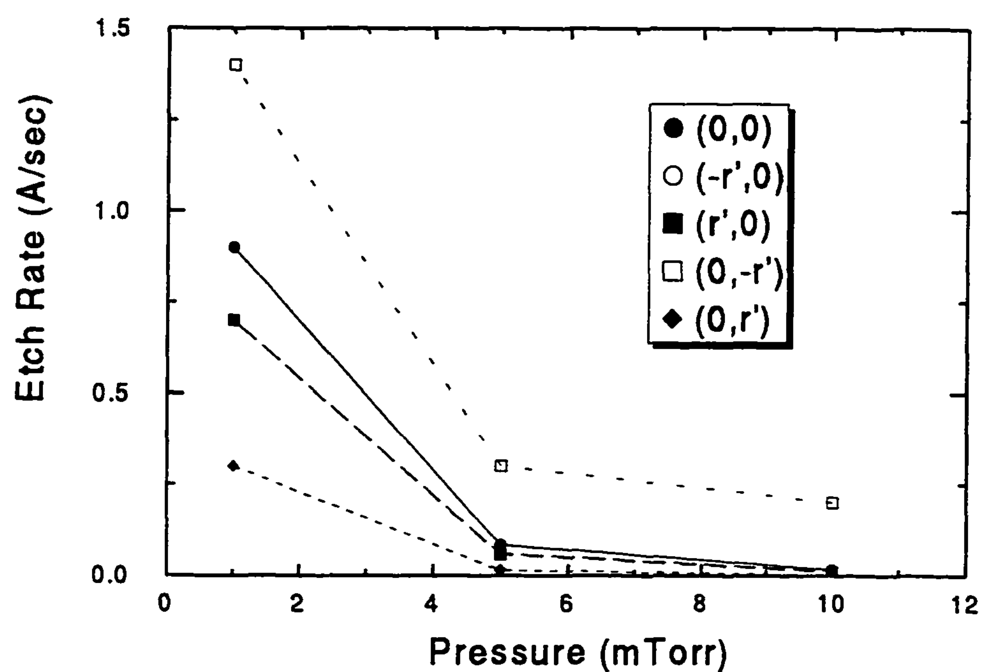

Figure 4.15: Etch rate of Kapton vs. pressure estimated from modeled energy distributions using etch yields of hyperthermal oxygen atoms measured by Jon Cross [41] (used with permission).

Reproduced with permission of the copyright owner. Further reproduction prohibited without permission.

the plasma stream could provide some uniformity control.

Placement of the wafer with respect to the reflector has shown to be an important parameter for delivery of high neutral flux. While the magnitude of the flux is attenuated by moving away from the reflector, the flux becomes more uniform and directional which is important for possible processing applications.

Preliminary calculations (2-D ray trace model) have also shown that by manipulation of the geometric contour of the reflector plate and/or by providing special mesoscale texturing of the plate surface, substantial improvements in uniformity may be gained. Meanwhile, the geometry described in this work is predicted to be suitable for cleaning applications or possibly for "soft-landing" overetch steps in semiconductor processing where charge-induced damage is most likely to occur.

Reproduced with permission of the copyright owner. Further reproduction prohibited without permission.

Chapter 5

Neutral Source Performance

5.1 Plasma Characterization

The ions for reflection are created in a high-density, low-pressure plasma source. In this work, an inductively-coupled-plasma (ICP) source is used. As stated earlier, the creation of hyperthermal neutrals is dependent on the ion density at the reflector plate. In this section, the characterization of the plasma source will be discussed. The parameters of interest are the ion density at the reflector plate and the general plasma density profile.

5.1.1 Langmuir Probes

The primary diagnostic used for density determination is the Langmuir single probe. In its simplest form, the Langmuir probe is a wire of known dimension placed directly in the plasma. A potential is applied to the wire such that it draws current from the plasma. If certain assumptions are made about the electron energy distribution (Maxwellian, non-Maxwellian, etc.), the I-V curve can be used to obtain valuable information about the density, electron temperature, and potential of the plasma. The discussion below follows largely from the excellent reviews of plasma diagnostics and electrostatic probes given by Manos and Dylla [43], Ruzic [44], and Schott [45].

Fig. 5.1 shows the general I-V curve for a Langmuir single probe. In region (1), the

Reproduced with permission of the copyright owner. Further reproduction prohibited without permission.

applied potential is very negative compared to the plasma potential. Thus, all electrons are rejected and only ions are collected. Hence this current is positive. As we move higher in applied potential, region (2), the higher energy electrons begin to overcome the applied negative potential and are collected. At this point the current begins to go more negative as we add negative charges to the current. Finally, as the potential becomes closer to the plasma potential, we begin to collect the lower energy electrons of the distribution. As we saw in Chapter 2, the peak of the electron energy distribution lies at approximately $T_e/2$. When the applied potential exceeds the plasma potential, we are collecting all electrons and repelling all ions, region (3), called electron saturation.

The curve in Fig. 5.1 shows the ideal behavior of the electron saturation current region. In reality, the current is very unstable in this regime with respect to the applied bias. Experimentally, this regime is very difficult to measure because the probe begins to perturb the plasma such that further measurements do not yield useful information. Most traces stop when the "knee" of region (3) begins in order to avoid this regime.

Ion Saturation Region and Floating Potential

If the probe is isolated from any external voltage supply, the total current through the probe is zero. Although the densities (ion and electron) in the bulk plasma are equal (quasi-neutrality), the velocities of the two species differ by many orders of magnitude. This can be seen by comparing the thermal velocities of each. Recall that the average velocity of a particle of temperature, T, and mass, m, is given by $\bar{v} = (8kT/\pi m)^{1/2}$. Thus the ratio of velocities will be $(T_e m_i/T_i m_e)^{1/2}$. The ratio of masses is on the order of 2000, while T_e approximately $3-5$ eV and T_i approximately RT to 0.5 eV, where RT = 0.025 eV is room temperature.

When the probe is initially placed in the plasma, more electrons than ions strike the probe. With no current path to bleed away charge, the negative charge accumulates, leading to a negative potential on the probe (with respect to the potential of the plasma itself). This

Reproduced with permission of the copyright owner. Further reproduction prohibited without permission.

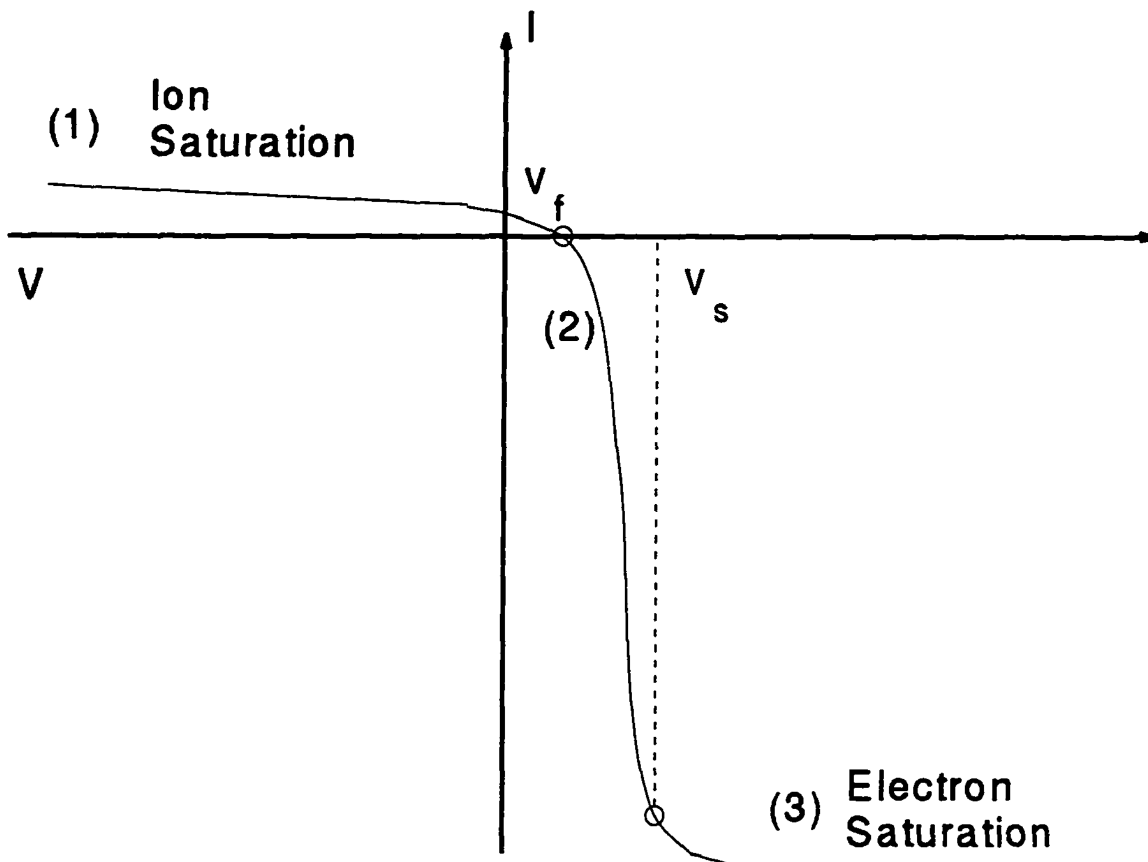

Figure 5.1: The general I-V curve from a Langmuir single probe. At high negative applied voltage, only positive ions are collected in the ion saturation regime. At high positive voltage, all electrons are collected in the electron saturation regime. The transition region between the two regimes provides information on electron temperature.

Reproduced with permission of the copyright owner. Further reproduction prohibited without permission.

negative potential accelerates ions and repels electrons. Thus a positive space charge "sheath" is formed leading to an equilibrium between electron and ion fluxes. The point on the I-V characteristic where this occurs ($I_{probe} = 0$) is called the floating potential, V_f.

If the probe potential is negative with respect to the floating potential, such that $-eV_p \gg kT_e$, then no electrons will be collected since they cannot overcome the potential barrier. The current collected is then the ion saturation current, given by

$$I_{+_{sat}} = e\left(\frac{1}{4}n_{+_o}\bar{v}_+\right)A_p \tag{5.1}$$

where n_{+_o} is the ion density at the sheath edge, and A_p is the probe area. Note that the apparent probe area can be larger than the geometrical area due to sheath size effects. How to account for this will be discussed below.

Transition Region and Electron Saturation

As we increase the probe potential near the floating potential, the higher energy electrons begin to overcome the potential barrier represented by the sheath and are collected by the probe. The density distribution in the positive sheath is governed by Boltzmann's law,

$$n_e = n_o \exp\left(\frac{eV_p}{kT_e}\right); V_p < 0 \tag{5.2}$$

where V_p, the probe voltage, is measured with respect to the plasma potential. The random electron flux to the sheath edge is given by a relation similar to eqn. 5.1,

$$I_{e_o} = -e\left(\frac{1}{4}n_{e_o}\bar{v}_e\right)S \tag{5.3}$$

where S is the area of the sheath presented to the plasma. If we assume that the mean electron velocity at the sheath edge is equal to the velocity at the probe surface, we can write

$$I_e = -e(\frac{1}{4}n_{e_o}\bar{v}_e)A_p \exp\left(\frac{eV_p}{kT_e}\right) = I_{e_o}\exp\left(\frac{eV_p}{kT_e}\right) \tag{5.4}$$

where A_p is the geometrical area of the probe. The total current to the probe in the exponentially increasing part of the I-V curve (region (2) in Fig. 5.1) can be written

$$I_p = I_{+_o} + I_{e_o}\exp\left(\frac{eV_p}{kT_e}\right) \tag{5.5}$$

Reproduced with permission of the copyright owner. Further reproduction prohibited without permission.

We note here that from eqn. 5.5, we can write

$$\frac{d[\ln(I_p)]}{dV_p} = -\frac{e}{kT_e} = -\frac{1}{T_e(eV)} \tag{5.6}$$

Thus by examining the region about the floating potential in a voltage window of approximate width $\Delta V_p = \pm(kT_e/e)$ [45], we can obtain the electron temperature directly from the I-V curve. We should note that at this point in the I-V curve, not all of the ions have been repelled. Before taking the value for T_e, we should subtract the ion saturation current from the I-V curve for improved accuracy [44].

As we reach the plasma potential, V_s in Fig. 5.1, fewer and fewer ions are collected. At $V_p = V_s$, we see that the probe current becomes $I_p = I_{+_o} + I_{e_o} \approx I_{e_o}$, at electron saturation. However, this current relation is only valid for collected currents that are small compared to the random current of eqn. 5.3. Drawing more current than this will perturb the plasma by raising the plasma potential and distorting the I-V characteristic. Thus, measurements should only be taken up to near the plasma potential.

Probe Size Regimes

The methods used to determine plasma parameters from the I-V characteristic vary depending on the relative size of the probe with respect to the Debye shielding length, $\lambda_{de}[cm] = 743\sqrt{T_e/n_e}$. This is the characteristic distance of the plasma sheath. It represents the distance over which quasi-neutrality can be locally violated. Plasma sheaths at low voltage surfaces (non-current carrying) can be on the order of 3 - 10 Debye lengths [12]. For example, a discharge with an electron temperature of 5 eV and a density of 1.0×10^{11} cm^{-3} will have a Debye length of 0.005 cm, or an approximate sheath thickness of 0.015 to 0.05 cm.

Probe sizes are divided into two main groups: planar and cylindrical. A planar probe is one where the ratio of probe radius to Debye length, $r_p/\lambda_{de} \gtrsim 3$. A cylindrical probe is then one with $r_p/\lambda_{de} \lesssim 3$. In our case, with plasma densities of approximately 5×10^{11} cm^{-3} and temperatures of approximately $3 - 5$ eV, and a probe radius of 0.0127 cm, we expect to

Reproduced with permission of the copyright owner. Further reproduction prohibited without permission.

be in the planar regime for the most part.

However, for the case where densities or temperatures vary widely, or the radius/Debye-length ratio is borderline between the planar and cylindrical cases, it is best to use the Laframboise method, which is reviewed in reference [44]. Laframboise solved Poisson's equation numerically for various ratios of probe radius to Debye length. His results do not give an analytical solution, but do give quantitative results for comparison, with the only parameter being the length ratios.

The Laframboise plot appears in Fig. 5.2. On the X axis, we find the dimensionless quantity, X_p, which is the ratio of applied probe bias with respect to the plasma potential and electron temperature. For a given length ratio, the value j_i^* gives the sheath geometrical correction factor that incorporates information about the sheath. We can now write the ion current as

$$I_i = \frac{1}{4} e n_e \sqrt{\frac{8kT_e}{\pi m_i}} A_{\text{probe}} j_i^* \tag{5.7}$$

Eqn. 5.7 can be solved for density. Written in useful units (eV, amu, etc.) the density is given by

$$n_e[\text{m}^{-3}] = 1.6 \times 10^{15} \sqrt{\frac{m_i[\text{amu}]}{T_e[\text{eV}]}} \frac{I[\text{amps}]}{A_{\text{probe}}[\text{m}^2] j_i^*} \quad . \tag{5.8}$$

where I[amps] is the current collected at the applied bias, V, used in the parameter $X_p = e(V_{\text{plasma}} - V_{\text{applied}})/kT_e$. Note that to use eqn. 5.8 directly, we must already know T_e and n_e. This apparent problem is solved by iteration of the above procedure.

The iteration proceeds as follows. First, estimate T_e from the electron retardation region of the I-V curve (region (2) in Fig. 5.1) as in eqn. 5.6, then guess a density. Obtain j_i^* from a calculation of r_p/λ_{de}, then get a new density. Continue this process until the value is obtained to sufficient precision. Generally, with a good initial guess for the density, only 2 - 5 iterations are needed. This is the method employed in this work to obtain electron temperatures, plasma potentials, and densities in the plasma source.

Reproduced with permission of the copyright owner. Further reproduction prohibited without permission.

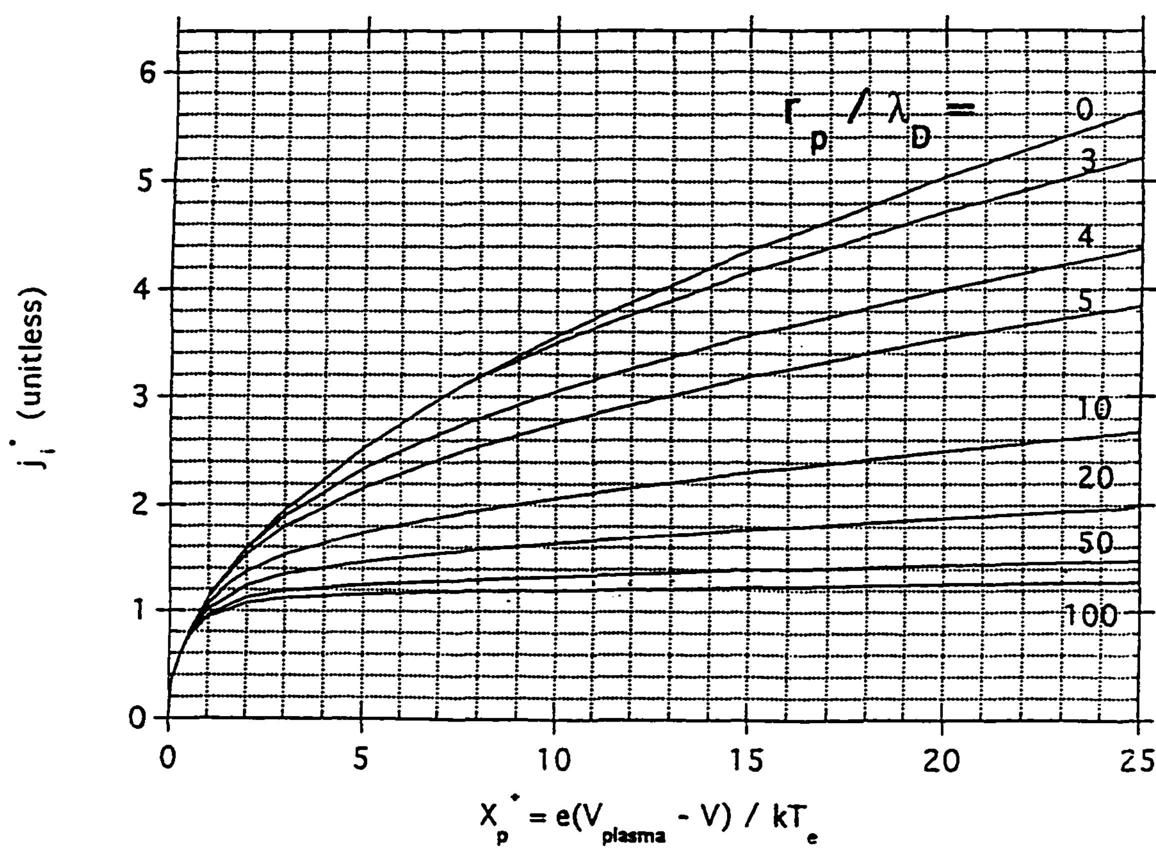

Figure 5.2: The general Laframboise plot used for determining various plasma parameters. The use of the plot is described in the text.

Reproduced with permission of the copyright owner. Further reproduction prohibited without permission.

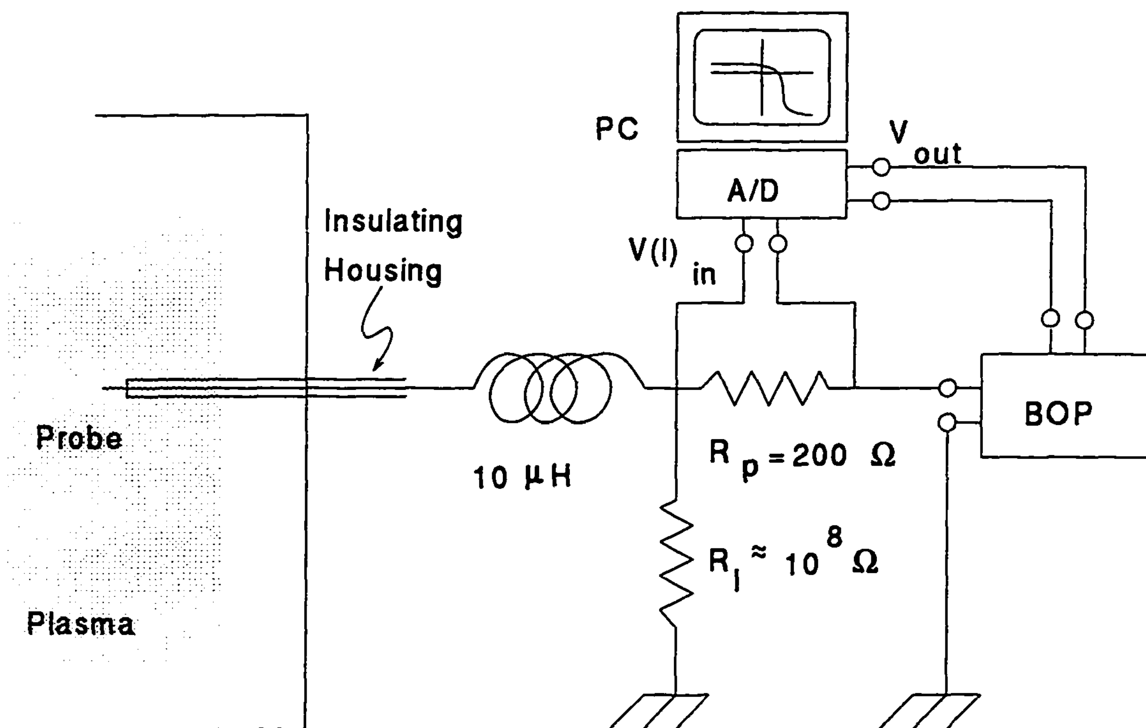

Figure 5.3: Langmuir probe circuit used in the determination of plasma parameters.

Reproduced with permission of the copyright owner. Further reproduction prohibited without permission.

Langmuir Probe Construction

The Langmuir probe circuit used for this work appears in Fig. 5.3. A 10 mil diameter tungsten wire is used as the probe for this work. The probe is sheathed by an alumina tube with a diameter of 0.065″ such that 0.25″ is exposed beyond the tube. A 10μH inductor is used for low pass filtering to reject high-frequency oscillations due to the rf plasma source. The applied bias is provided by a Kepco 500-80M bipolar operational (BOP) amplifier driven by a -10 to 10 Volt signal from the Pentium based PC. Current is read from a 120 ohm resistor in series with the BOP. A data acquisition system based on the software package LABVIEW from National Instruments, Inc. is used to obtain the data which is saved for later processing.

The probe was inserted in the vacuum vessel via a 1/4″ Viton o-ring compression fitting. While this type of vacuum feedthru can be opened and closed while the chamber is under vacuum, this act tends to contaminate the chamber, altering the plasma parameters. However, it was necessary to stroke the probe across the plasma chamber to obtain density and temperature information as a function of position.

For this purpose we designed a bellows system that could be mounted to the chamber via Conflat (copper o-ring, metal-to-metal seal) flanges. The probe was installed in the bellows system which allowed us to move the probe manually or motor-driven. The bellows was capable of 6″ total travel, which corresponds to the inner diameter of the 8″ Conflat cross used as a vacuum chamber.

5.1.2 Plasma Density Measurements

Radial Density Profiles

Fig. 5.4 shows the radial profiles for 600 W applied rf power for 1, 4, and 8 mTorr. This profile is similar to that expected from any multipole magnetically confined ICP source [16] as discussed earlier (see Fig. 2.7). Measured plasma densities for this power level are on the order of 1×10^{11} cm^{-3}, with electron temperatures of T_e approximately $3 - 5$ eV. The

Reproduced with permission of the copyright owner. Further reproduction prohibited without permission.

electron temperatures are nearly independent of power, but do vary over the range specified as a function of pressure, in agreement with the literature [16, 17].

Also shown in Fig. 5.4 are the plasma density profiles predicted by the global plasma model at the "front-end" of the Monte Carlo simulation. We note that the density profiles agree quite well (within 15%) with the simulated values. For a surface reflection neutral stream simulator to be successful, it must first determine the correct ion flux to the reflector plate. This is only possible if the simulated plasma profile is a reasonable approximation of a "real-world" system.

Also recall that the Monte Carlo model simulates the effect of neutrals falling through the plasma by considering electron impact ionization of the neutrals, as well as symmetric or asymmetric charge exchange between reflected neutrals and background ions. To fully include these effects, the plasma density profiles must be known.

Ion Flux to the Reflector Plate

The reflector plate can be biased from 0 to -60 Volts to control the kinetic energy of the ions. It is important to maximize the flux of ions at the plate without increasing sputtering of the plate material, which could dope or otherwise contaminate the wafer. The dependence of ion flux (total current) to the reflector plate as a function of plate bias is seen in Fig. 5.5.

The reflected energies considered in this work (23, 35, and 47 eV) correspond to reflector plate biases of 8, 20, and 32 Volts. In Fig. 5.5 we see that these values fall in the ion saturation region of the plate I-V curves. That is, the ion flux to the plate is maximized at these values. For reflector biases lower than 8 Volts, we begin to see a reduction in reflector current. This does not mean that the ion flux is reduced. Recalling the earlier discussion of Langmuir probes, we know that energetic electrons begin to overcome the sheath at the probe near the floating potential. The reflector plate is itself a large-area electrostatic probe. The ion current will likely stay nearly constant up to the floating potential [43–45]. However, in order to get ion flux measurements directly from the plate current, we stay in the ion

Reproduced with permission of the copyright owner. Further reproduction prohibited without permission.

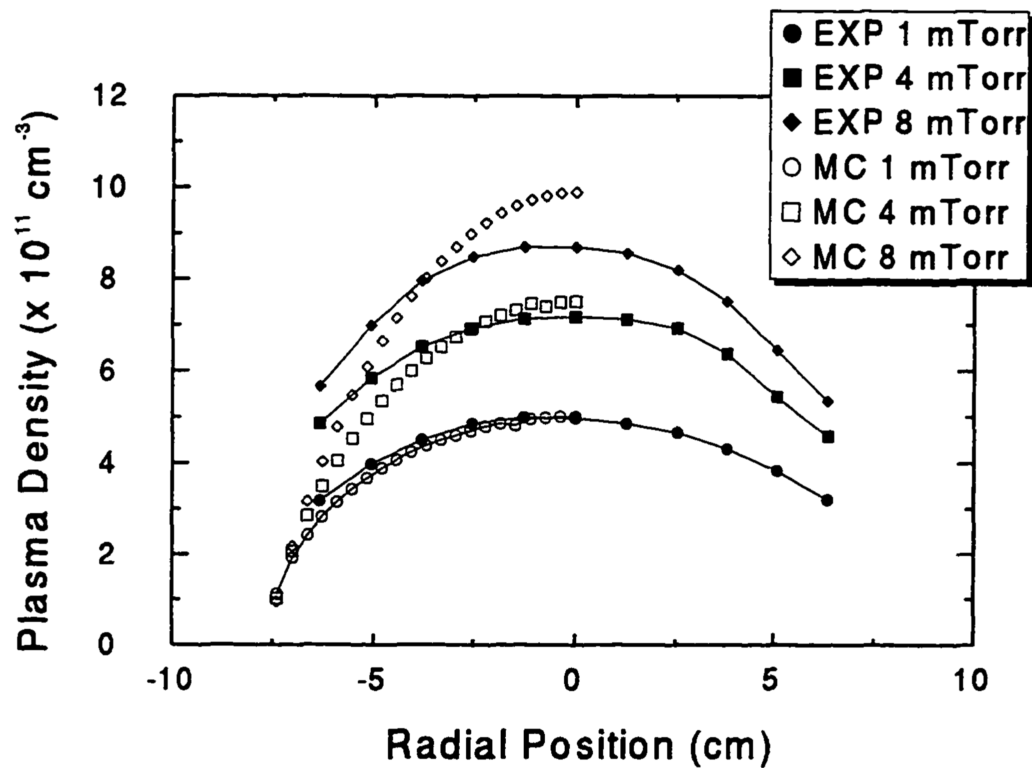

Figure 5.4: These radial plasma density profiles were measured across the plasma chamber 4 cm below the dielectric window of the ICP (refer to Fig. 2.11) at pressures of 1, 4, and 8 mTorr. A welded bellows manual translator with a 6″ stroke was used. Also shown are the profiles predicted by the global plasma model in the Monte Carlo simulation.

Reproduced with permission of the copyright owner. Further reproduction prohibited without permission.

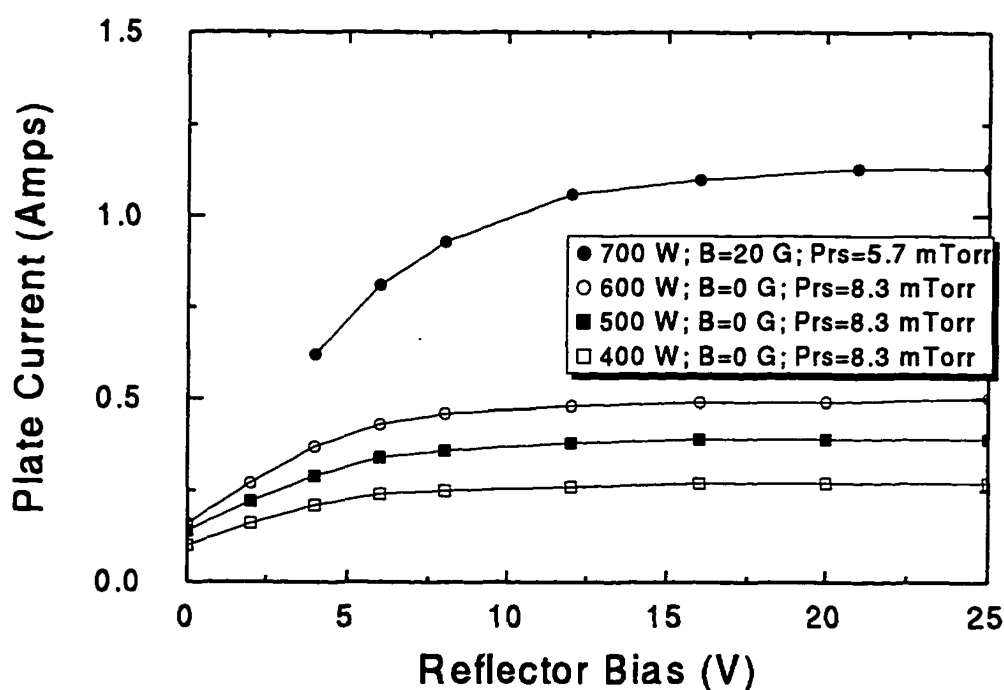

Figure 5.5: Current/Voltage curves for reflector plate vs. plate bias. Shown are the plate currents for 3 powers at 8.3 mTorr. The 700 W curve shows the increase in plasma density realized when including a longitudinal magnetic field. Note that these curves follow the same form as the ion saturation region of a Langmuir single probe.

Reproduced with permission of the copyright owner. Further reproduction prohibited without permission.

saturation region where little or no electrons are collected.

Ion current to the reflector plate as a function of pressure and applied rf power appears in Fig. 5.6. We see that the current at the reflector plate is roughly linear with power due to the linearity in plasma density in power. The collected ion current also falls somewhat with pressure as the mean free path for ion/background collisions becomes smaller. However, the falloff is roughly linear and not very pronounced (falling only 8% from 2 mTorr to 10 mTorr at 1000 W). We can expect that the neutral flux emitted at the plate will follow the same trend.

The plasma model predictions for delivered ion flux is also shown in Fig. 5.6 for comparison. There is good agreement with the model (within 10%) at all three powers. However, we note that the predicted and measured values diverge below 2 mTorr. This is due to increased radial diffusional losses of the ions from the plasma, which are not considered in this simple global model.

Magnetic Confinement

Two axial-field magnetic confinement schemes were tested in this work. Two 200-turn Helmholtz coils were constructed from 10 AWG insulated solid copper wire. One confinement scheme involved placing an electromagnet around the plasma source such that the maximum axial magnetic field would be in the center of the discharge just below the dielectric window of the ICP. Although this method showed an increase in plasma density (see Fig. 5.5, the plasma streamed along the diverging magnetic field lines. The effect was to allow plasma to flow throughout the chamber such that no collimation of the plasma stream was realized. The purpose of magnetic confinement is to minimize plasma (reactant ions) at the edges where the wafer is situated. Thus when the plasma fills the entire discharge chamber, large ion fluxes at the wafer would defeat the stated goal of charge-free processing.

The second possible scheme involved placing a single Helmholtz coil opposite of the plasma source (the bottom coil in Fig. 2.11). In this case, the field lines intersecting the

Reproduced with permission of the copyright owner. Further reproduction prohibited without permission.

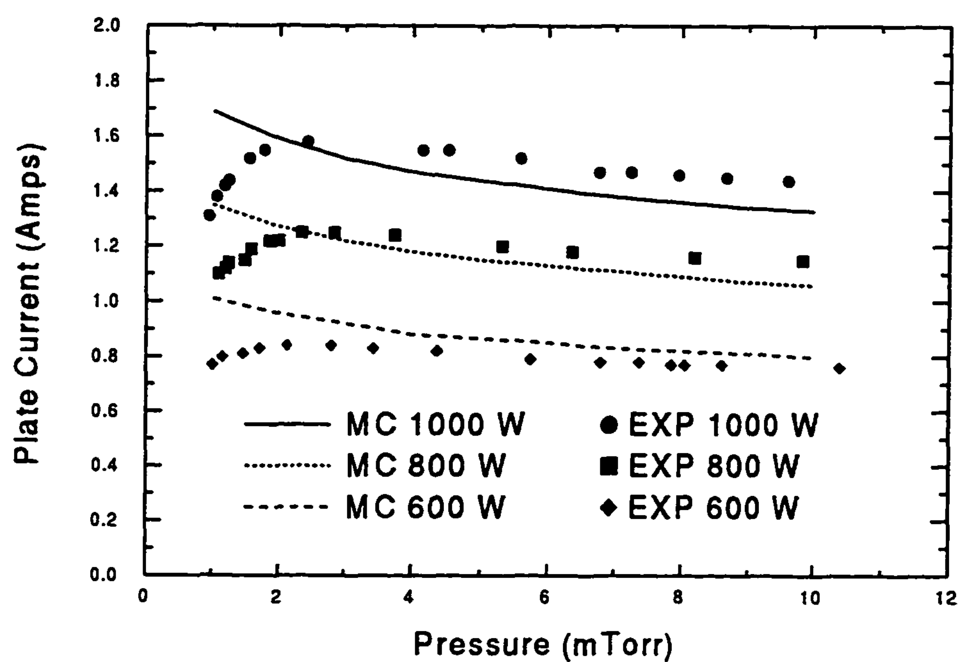

Figure 5.6: Ion flux measured by the reflector plate for various powers (600, 800, and 1000 W) and pressures (1 - 10 mTorr). Predicted values of plate current are shown for comparison.

Reproduced with permission of the copyright owner. Further reproduction prohibited without permission.

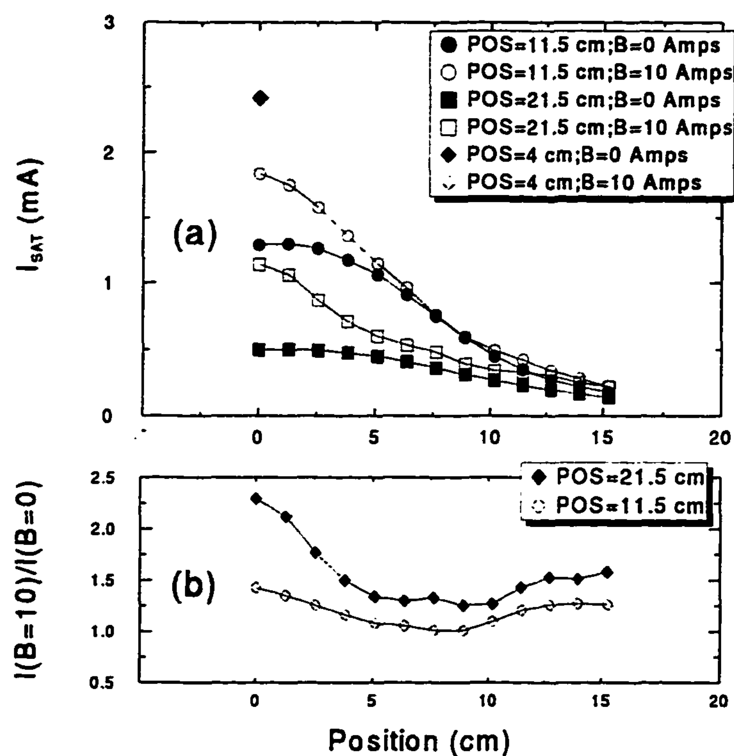

Figure 5.7: Improvement in plasma density with introduction axial magnetic field. Measurements of ion saturation current (proportional to plasma density) with a Langmuir probe are given for three distances from the dielectric window of the ICP; 4, 11.5 and 21.5 cm. The bellows probe translator was used to obtain the profiles at 11.5 and 21.5 cm. The ratio of I(B=10 Amps)/I(B=0 Amps) is shown in (b). The B-field values are reported in units of current in the 200-turn coil. A current of 10 Amps corresponds to 20 gauss in the center of the discharge vessel.

Reproduced with permission of the copyright owner. Further reproduction prohibited without permission.

plasma would be near normal to the plasma source, i. e., no diverging field lines to allow plasma to flow radially. The effects were measured with the Langmuir probe in the absence of the reflector plate. The results appear in Fig. 5.7.

The values reported in Fig. 5.7(a) are the ion saturation current on the Langmuir probe. This value is largely proportional to plasma density and is unaffected by the magnitude of the magnetic field used here. Analysis of probe data in the presence of a magnetic field is difficult (electrons are highly perturbed by small fields) and is not attempted here. However, full analysis is not necessary since we are only interested in the ratio of densities.

Although the plasma density along the axis is clearly improved by the introduction of the axial field, the edge density is not reduced. This is due to diffusion of the ions along the radial density gradient. The profiles beyond 5 cm show an exponential falloff dependence with a characteristic distance of approximately 7 cm. The presence of charge at the wafer position will be a problem when attempting to use this source in a charge-free etch step. Further complications arise in the ion density gradient itself because these radially-going ions can attain high energies (5 - 10 eV) as they fall across the plasma potential gradient [46]. This added energy may result in further etching of the substrate, overshadowing the expected benefit of hyperthermal neutral etch.

These measurements were taken in the absence of a reflector plate. The values are not compared to simulated values because the model does not account for complicated geometrical effects. The plasma model assumes a cylinder of radius R and length L. In the prototype device, the dimensions of the chamber change (see Fig. 2.11) near the center of the discharge. This complicated geometry is difficult to model accurately with a simple global model. A fluid model (3-D) is required to if geometrical effects need to be considered.

When an axial magnetic field is applied to a discharge with the reflector plate installed, the shape and angle of the plate affect the collected ion current. It is found that with a circular reflector plate at an angle near 45°, the collected ion current is actually reduced as magnetic field is increased. This effect can be understood by visual inspection of the plasma through

Reproduced with permission of the copyright owner. Further reproduction prohibited without permission.

a window on the chamber. As coil current is increased, the discharge becomes a column of bright plasma. This column follows the magnetic field lines rigorously. However, the magnetic field lines do not intersect the plate on the edges of the plate so the plasma streams past the reflector plate without increasing collected plate current. Conversely, if the plate is placed at an angle of 0°, such that the plate normal is directed at the plasma source, the collected ion current increased by about the same factor found for the 11.5 cm case of Fig. 5.7. This apparent problem could be corrected with an elliptical reflector plate. The Monte Carlo model assumes such an elliptical reflector.

5.2 Etch Rate Characterization

A full experimental verification of the modeled reflected neutral flux characteristics is beyond the scope of this work. However, preliminary studies introducing etch samples at model locations in the prototype device were performed. Below are the methods employed to determine the etch rate due to reflected neutral flux. A comparison is made to the expected etch rates based on simulated values.

Simulation Parameters

In order to simulate the flux expected from the prototype device, we input the actual geometric parameters used in the experiment. Table 5.1 gives the input parameters for this analysis.

Parameter	Value(s)
Wafer Radius	10 cm
Reflector Angle	45°
Pressure [mTorr]	1.0
Cosine Emission (n_θ)	1.3
Reflector Bias [Volts]	-25
Wafer Distance [cm]	3

Table 5.1: Parameters for simulation in etch rate analysis.

Reproduced with permission of the copyright owner. Further reproduction prohibited without permission.

This simulation is run and results compiled before the sample is inserted in the device. The expected peak flux position is determined from the wafer flux maps. The peak flux position is chosen as the sample position to provide direct comparison.

Before an etch sample can be attempted, the contribution of the ions to the total etch rate must be determined. This is done by introducing a 1.8 cm^2 conductor in the sample position where the ion flux can be read directly.

The ions need to be rejected before a comparison of neutral to ion etch rates can be attempted. This is accomplished by placing a cylinder of 2:1 (Length/Diameter) aspect ratio (see Fig. 5.8) over the sample to shield it from the ions. Further ion shielding is realized by placing a 200 line-per-inch 304 stainless steel grid at the entrance to the cylinder. The transparency of the grid is 50%.

Fig. 5.9 shows the I-V curves for the current probe placed at the sample position. It is found that the cylinder reduces the ion current to the sample position by a factor of approximately 200×. Thus any etch rate found in the presence of the cylinder may be safely assumed to be due to neutral etch.

The possibility of photo-activated surface dissociation and etching is currently not considered because the same etch conditions with a MgF_2 window in front of the cylinder (to allow large fluxes of 10 eV uv photons) shows no surface modification. The transmission of 1305 Å uv photons from the oxygen plasma through the MgF_2 window is approximately 10%. It is possible that all of the etching could be due to photo-activated etching of the Kapton surface. However, if this were true, some etching of the surface at approximately 0.2 Å/sec would be detectable with the cylinder and window in place. Since no etch rate is observed, this possibility is discounted.

There is some evidence [47] that hyperthermal neutral etching can be enhanced or activated by the synergism between vacuum ultraviolet radiation and hyperthermal reactive neutral flux. In the work cited above, a beam of 1.5 eV atomic oxygen is directed at a number of samples, including Kapton, in the presence of 10 eV (123.6 nm Kr line) photons. It was

Reproduced with permission of the copyright owner. Further reproduction prohibited without permission.

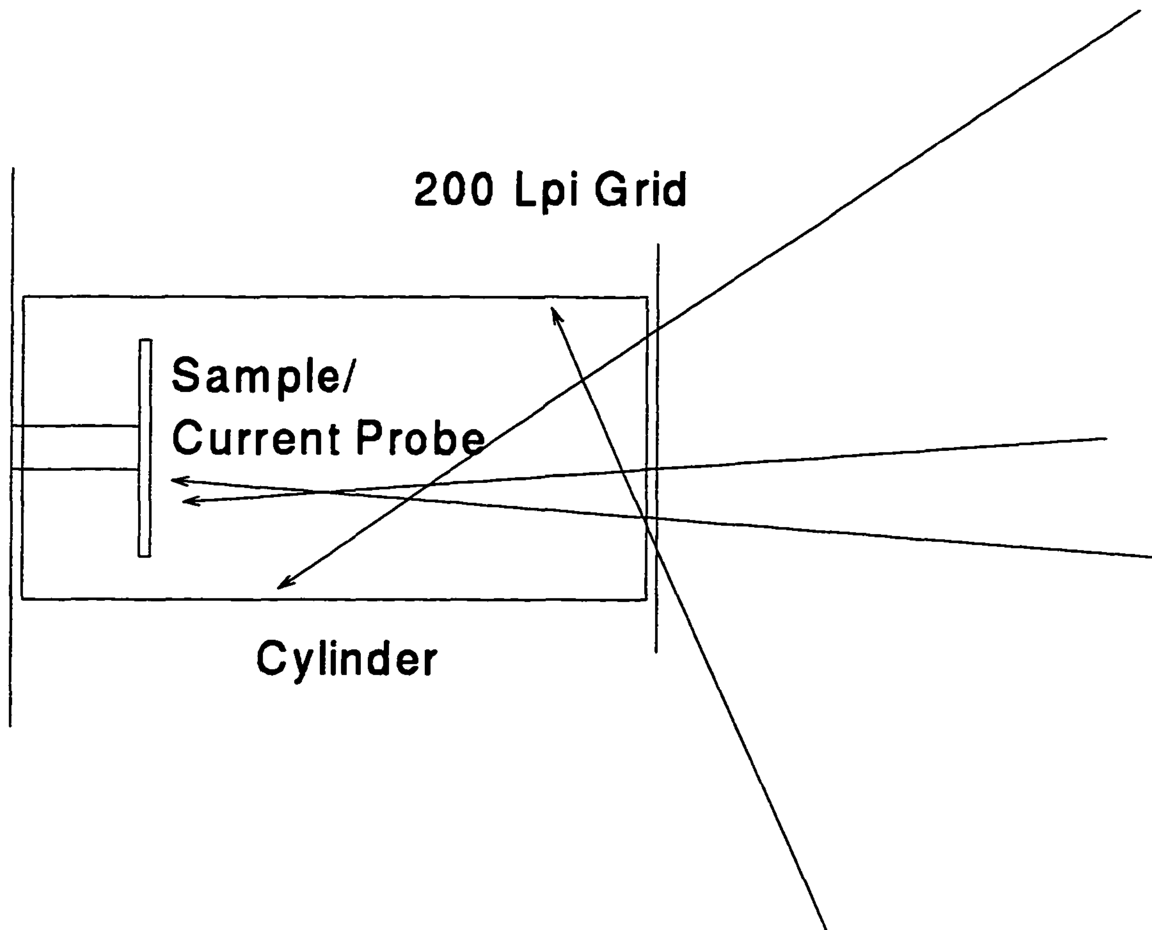

Figure 5.8: Ion current repeller for sample position. Shown are several neutral trajectories showing cutoff of flux associated with cylinder.

Reproduced with permission of the copyright owner. Further reproduction prohibited without permission.

found that significant etching of the samples occured with photons and atoms incident on the surface. If either were removed from the sample, no etching took place. The possibility that this process is responsible for our observed effects should be closely investigated in the future.

The parameters used in the sample runs were 800 W and 1 mTorr. Ion saturation currents were 0.012 mA/cm^2 with the cylinder present, and 2.5 mA/cm^2 with the cylinder absent. These can be converted to fluxes of 6.9×10^{13} and 1.5×10^{16} ions/cm^2/sec, respectively.

The cylinder represents a flux barrier to neutrals incident at angles larger than the 2:1 aspect ratio allows ($\theta' \leq 14^o$). Integrating the θ' angular distribution from 0 to 14° gives the ratio of fluxes with and without the cylinder. Carrying out this integration for the simulated distribution gives a value of 15%. If it is assumed that the neutral etch rate is independent of incident angle (which is not true in general [48]), the neutral component of the etch rate without the cylinder would be 6.6X the measured value with the cylinder in place.

Etch Rate Determination

The etch rates of the Kapton samples are determined by placing a 500 line-per-inch tungsten electro-formed mesh over the sample. This provides a mask through which neutrals (or ions) can travel. The etch rates are determined by comparing the depth of the unmasked regions to those regions covered by the mesh. The surface profile measurements were carried out using an Atomic Force Microscope (AFM). The etch runs lasted for 1 hour at 800 W and 1 mTorr.

Etch Due to Ions and Neutrals

Table 5.2 gives the etch rate values with the ion saturation currents. As the ion cylinder is removed, a 200$\times$ increase in ion current is seen. Part of the current increase is likely due to to ion collection on the back of the sample probe, which is open to the plasma. However, this would only introduce an worst-case error in ion current of a factor of two for

Reproduced with permission of the copyright owner. Further reproduction prohibited without permission.

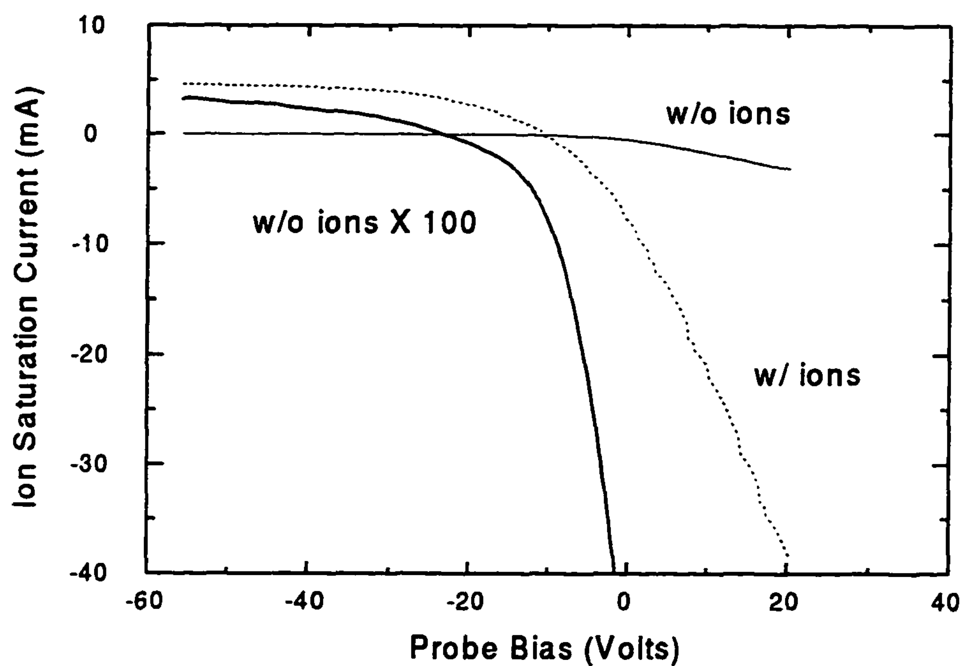

Figure 5.9: I-V curves for sample position. In the presence of the ion-rejecting cylinder, the ion saturation current is reduced by approximately 200×.

	Ion Flux	Etch Rate [Å/sec]
w/ Cyl	0.0012	1.89
w/o Cyl	2.5	9

Table 5.2: Etch rates and ion fluxes [mA/cm^2] at sample.

Reproduced with permission of the copyright owner. Further reproduction prohibited without permission.

the no-cylinder case. The etch rate is seen to increase by only a factor of five between the cylinder and no-cylinder cases. One would expect an increase of at least 100× from such an increase in oxygen ion current density. The samples were shorted to ground during the experimental etch runs, thus the ions would not have achieved the kinetic energy that they normally would see in falling across the plasma sheath at a negatively biased substrate. This may help to explain why the etch rate does not increase simply with flux, unless some kinetic energy is added to the ions to activate their contribution to the etch [49].

There is some evidence that this etch rate for no-cylinder may be enhanced, or completely due to reflected, hyperthermal neutrals. The factor of five increase is consistent with removing the angle constraint of the cylinder, thereby allowing all neutrals to strike the wafer when the cylinder is removed.

Better evidence for neutral enhanced etching is provided by AFM measurements. The AFM allows cross sectional analysis of etch profiles. The 2-D cross section of the unmasked region of an etch sample shows that one side of the mask has been etched at a larger angle than the opposite side. This non-directionality of etch could be due to the angular distribution of the beam as seen by the angular distributions predicted in Chapter 4. This behavior is not expected or seen in ion-based etch steps where the ion flux is largely electrostatically collimated by the plasma sheath. At present, we can find no other mechanism at work in this source that could account for the etch anisotropy found in the samples.

However, results from other wafer etch experiments involving a smaller scale surface reflection neutral stream source show that the angle of the incoming stream does effect the profile of the feature [7]. A full geometrical wafer etch experiment with semiconductor damage measurements will be required to confirm the suggestions of the possible dominance of fast neutrals over ion etch in the prototype source.

Reproduced with permission of the copyright owner. Further reproduction prohibited without permission.

Comparison to Model

The Monte Carlo simulation predicts a reflected neutral flux of approximately 1.88 mA/cm^2 for the above conditions. The etch rate expected for such a flux (assuming all of the energy distribution contributed to the etch) is 3.3 Å/sec. This is a factor of three smaller than actually observed for the no-cylinder case, but twice that seen with the cylinder installed.

For the level of assumptions made for the model (equality of argon and oxygen plasma, cylindrical geometry, etc.), an agreement in final flux of within a factor of ten is reasonable. Large uncertainties in etch rate characteristics of hyperthermal neutrals (angular and energy dependencies, etc.) cause difficulty in modeling the final process with any accuracy.

5.3 Performance Conclusions

It is shown that the global plasma model used for the Monte Carlo simulation can accurately predict the plasma density profile of the prototype device. The ion flux to the reflector is also well predicted. Prediction of the ion flux to the reflector plate is quite important because this represents the source of hyperthermal neutrals.

Magnetic confinement of the plasma stream has been shown to be effective in increasing the plasma density along the center of the discharge. The best arrangement was an electromagnet coil placed opposite of the plasma source on the chamber, such that the magnetic field lines intersected the reflector plate. It is expected that such an improvement in plasma density will translate to higher collected ion currents at the reflector plate. However, this improvement could not be realized with the circular reflector plate used in this work. A design improvement was suggested for using an elliptically formed reflector plate to increase collected ion current.

Using a electromagnet coil near the plasma source proved to increase the plasma density in the source. However, the plasma was forced to flow along diverging field lines which filled the chamber with plasma. This would defeat any attempts at charge-free etching.

Preliminary measurements of etch rate were presented for cases with and without ions.

Reproduced with permission of the copyright owner. Further reproduction prohibited without permission.

It is seen that the Monte Carlo simulation can predict the etch rate to better than a factor of ten. However, with further refinement of the large assumptions made in the model for etch rates, the model agreement may be improved. Further study of the etch rates possible in this source, including angular and energy distributions, will be necessary to fully test the predictions of the model.

Our work suggests that the neutral etch is potentially dominant over ion-induced etch for this geometry. The increase in etch rate from samples with the ion repelling cylinder present over that of the no-cylinder case is approximately what would be expected for neutral etch after removal of the cylinder. Further, the cross sectional analysis of the etch profile suggests strongly a directional component of etch that would not be expected for an ion based etch process.

The etch rates found are expected to be suitable for semiconductor cleaning steps. Another possible application are soft-landing etch steps where this process is used for the last 10% of the feature etch process where charge induced damage is most likely to occur.

Reproduced with permission of the copyright owner. Further reproduction prohibited without permission.

Chapter 6

Discussion and Future Work

In this Chapter, conclusions are drawn about the suitability of this source for cleaning or feature etch. Suggestions are made for improvements to the design. Finally, a discussion of further characterization of the source needed for better understanding of the reflection characteristics is given.

6.1 Discussion

Uniformity

From the 3-D flux maps obtained by the ray-trace model of Chapter 3 and the Monte Carlo model of Chapter 4, we see that the reflected neutral fluxes are quite non-uniform. ICP based etch steps today can achieve best case uniformities of 2% (std. dev. /mean) [50] over an 8" wafer which is enough to reduce current-stress induced damage [51].

There are two reasons to keep the plasma etch step uniform over the wafer. First, non-uniformities in the plasma density and/or plasma potential cause current stress through the wafer or catastrophic oxide breakdown [4, 5] as discussed in Chapter 1. Potentially, this problem is overcome by not using ions to etch. The prototype device discussed in this work is optimal for testing the effect of neutral based etching in the presence of electrons because a positive dc bias on the wafer would eliminate ion flux while collecting electrons. Allowing the

Reproduced with permission of the copyright owner. Further reproduction prohibited without permission.

wafer to float is another method for balancing ion and electron fluxes, but does not guarantee current flow through the wafer (see Chapter 1) will be reduced.

A second reason for maintaining uniformity is based on relative material removal rates. The best uniformity from the 3-D flux maps of the Monte Carlo simulation gives approximately 60%. This means that for a perfectly uniform film thickness to be removed (e. g., 1 μ of photoresist over 100 Å of oxide), the film will be etched through at the peak approximately twice as fast as at the edges. Thus for the entire film to be removed, a 66% overetch is required (66% longer than time required to break through the film at the peak flux). This overetch has important implications for wafer damage during charge based processes [51].

If the chemistry is selective for the top film over the bottom film (oxygen will etch photoresist readily but will not attack SiO_2), the overetch in a neutral-based etch step will not cause a change in the bottom film thickness during overetch. As long as the etch process is charge free, uniformity issues should be unimportant when deciding potential etch applications.

Angular Distributions

It should be clear that in order to correctly transfer the pattern from the lithographically defined mask (see discussion, Chapter 1), a highly directional flux of reactants is required. Any off-normal incident ions or neutrals will cause erosion in the horizontal direction, so that critical dimension control will be lost. Ion-based etch steps do see some horizontal erosion, but for the most part the ions are collimated by the sheath.

Looking at the predicted angular distributions in Chapter 4, we see that the neutral flux is highly non-directional. Not only is the flux incident at some large angle with respect to the wafer normal, the flux has an azimuthal (projected) angular distribution weighted heavily towards the reflector plate. If this process is to be used for feature delineation, a much more directional flux needs to be realized. This will require a redesign of the surface

Reproduced with permission of the copyright owner. Further reproduction prohibited without permission.

reflection neutral stream source.

However, it is possible to use this flux for a cleaning application where uniformity or directionality are not required. For particularly aggressive etch steps, there is left on the wafer some thin residue that must be removed before continuing to the next process, usually a deposition step. Because this layer is quite thin, an cleaning process with a low etch rate may be used. Thus it is expected that this source could be used in the current form for cleaning applications.

Redesign of Neutral Stream Source

A number of design improvements suggest themselves based on this work. First, we found that a circular reflector plate reduced the collected ion current when an axial magnetic field is applied. It is suggested that an elliptical reflector plate be used instead. The models assume an elliptically shaped reflector.

Local texturing or faceting of the reflector plate, as opposed to a simple flat plate, showed some improvements in uniformity and directionality. Thus designing a reflector plate with these shapes would be a logical next step in trying to improve these parameters.

The 2-D results also show that an array of tunable sources could provide some measure of uniformity control. This would be especially useful because the uniformity becomes a function of external controls available to the user for optimization, rather than a non-variable parameter of the system.

A potential improvement in uniformity and directionality could be gained from the arrangement of Fig. 6.1. This arrangement utilizes a metal "cone" as the reflector. It could be fabricated by sputter deposition on some working metal sheet. A spiral ICP coil would be used to excite the plasma. The coil could be *in situ* as in the ionized physical vapor deposition (I-PVD) apparatus of appendix A [52, 53] or outside a quartz tube as seen in the original ICP work [54]. It is expected that the profiles realized by this design would appear as a surface of rotation of the profiles seen in the right-angle design.

Reproduced with permission of the copyright owner. Further reproduction prohibited without permission.

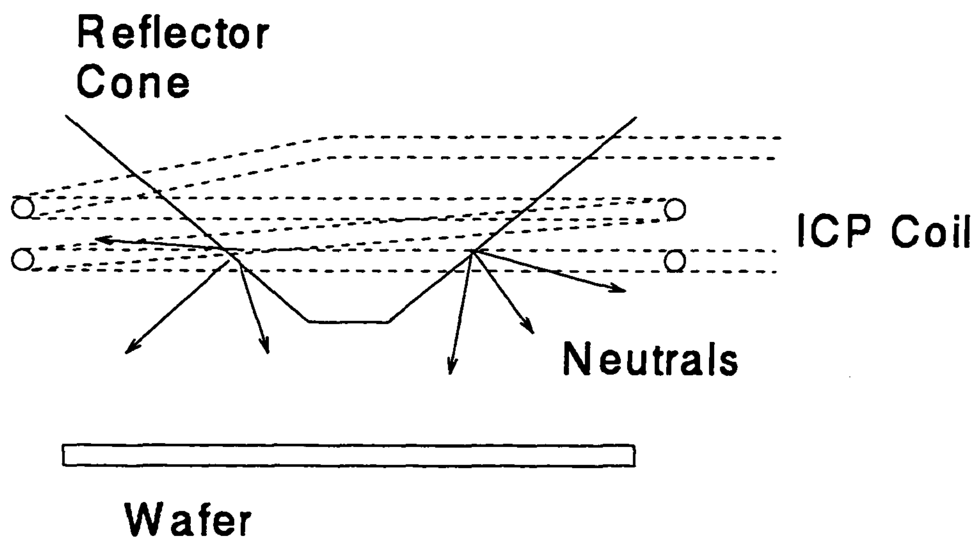

Figure 6.1: Alternate neutral stream source design.

Reproduced with permission of the copyright owner. Further reproduction prohibited without permission.

Improvements in atomic ion production can be made by going to lower frequency exciting power. It has been found that a lower frequency (0.46 MHz compared to 13.6 MHz) actively heats the ions of the plasma which promotes dissociation and the production of O^+ over O_2^+ [42]. This trend increases with applied rf power.

6.2 Future Work

A battery of experiments will be needed to fully understand the capabilities of this source. First the model predictions must be tested thoroughly. This entails direct measurements of the energy and angular distributions at the wafer position. Angular distributions can be elucidated from feature etch samples where the feature is examined after etch and the profiles compared to calibrated yield vs. angle curves. Energy distributions can be measured through the use of an energy analyzer, called a Bessel-box, in combination with a quadrupole mass spectrometer.

Wafer reflected neutral fluxes can be tested by directly placing full wafers, or an array of wafer pieces, in the apparatus. Etch rates vs. position would be compared to the relative fluxes and energy distributions predicted by the model. Each sample area on the wafer could also include the angular distribution test features.

The Monte Carlo model could also be used as a sputter deposition simulator with only minor modifications. The model is well suited for such a task because it considers collisions over all pressure regimes. Angular and energy information is obtained which could be coupled with a surface diffusion model to provide accurate deposition profiles.

6.3 Conclusions

Based on the results of this work, it is expected that a surface-reflection neutral-stream source can provide adequate fluxes and uniformity for at least a cleaning process. Further improvements to the current design could lead to feature etch capability. A number

Reproduced with permission of the copyright owner. Further reproduction prohibited without permission.

of improvements in design are suggested based on this work.

Reproduced with permission of the copyright owner. Further reproduction prohibited without permission.

Appendix A

Ionized Magnetron Sputter Deposition

Below appears a paper submitted and accepted by the Journal of Vacuum Science and Technology on ionized physical vapor deposition of copper for device interconnects. This work was performed by the author at IBM, with co-authors Steve Rossnagel and Satoshi Hamaguchi. Although not directly related to the bulk of this thesis, there are common threads. For instance, the plasma source is an ICP as in the thesis Also, the sputtered copper neutrals and reflected argon neutrals (the target is a biased metal plate) behave similarly to the reflected neutrals modeled in the thesis. In fact, the Monte Carlo model presented in the thesis could be modified to act as a simulator for the process described in this appendix.

A.1 Abstract

The ionized physical vapor deposition (I-PVD) technique is used to fill high aspect ratio trenches with copper. This technique allows directional filling of damascene features by sputtering metal atoms into a high density plasma. Large metal-atom ionized-flux fractions are achievable ($\approx$ 85%) leading to high directionality of deposition at the biased substrate. In this paper, we report quantitative measurements of fill directionality of Cu using an induct-

Reproduced with permission of the copyright owner. Further reproduction prohibited without permission.

ively coupled plasma (ICP) high density source. Copper is deposited into fairly aggressive (depth/width ≤ 1.5) damascene trenches. Metal ion flux fractions are estimated from direct measurement of the trench step coverage and compared to simulation. Estimates of the Cu+/Ar+ density ratios are also made to understand the influence of applied ICP power and Cu atom density (magnetron power) on fill directionality. It is found that at high magnetron powers (high copper atom densities) the plasma becomes "copper-rich", where the flux of copper ions exceeds that of the argon ions. At low magnetron power and high ICP power, we find the trench fill to be highly directional. As magnetron power is increased, directionality suffers due to cooling of the plasma by higher copper atom flux.

A.2 Introduction

Current sputter-based metallization techniques were designed for blanket film deposition, followed by reactive ion etch (RIE) patterning, to produce interconnect lines and vias. However, the sputtering process produces a flux with a roughly cosine angular distribution. When attempting to utilize this technology to fill high aspect ratio damascene vias and trenches, significant voiding occurs due to the nearly isotropic flux (pinch-off). The industry is currently studying metallization techniques that produce void-free fills.

A number of deposition methods are under consideration, or currently in production. These include chemical-vapor-deposition [55], electro-plating [56], mechanical collimation [57, 58] of sputtered species and ionized-physical-vapor-deposition (I-PVD) [53,59,60]. A review describing directional deposition techniques based on sputtering is available [61].

The I-PVD technique involves sputtering metal atoms into an inductively-coupled-plasma (ICP) region, although Cu atoms have also been evaporated into an ECR plasma region [62], producing high ionization fractions. The metal atoms are ionized in the high-density plasma, where they fall across a thin sheath at the biased wafer. These ions are thus electrostatically collimated to produce a highly directional trench (or via) fill. Ion energies at the wafer are easily controllable by wafer bias.

Reproduced with permission of the copyright owner. Further reproduction prohibited without permission.

This method has been the focus of previous experimental characterization [53,59,60] as well as modeling [63,64]. In this study, we report evaluation of the directional deposition in fairly aggressive aspect-ratio (AR $\leq$ 1.5) damascene trenches using I-PVD. The profiles achieved are compared to simulation [64] to assist in determining optimal process characteristics. This information is then used to qualitatively describe the synergistic interaction between magnetron and ICP powers, and their accompanying effects on fill directionality.

A.3 Experiment

A 28.5 cm diameter Cu target was used in an Applied Materials Endura rotating-magnet magnetron to sputter metal atoms into the high density plasma region. Magnetron power could be varied over the range 0 to 3 kW. Rf power applied to the 2-turn copper coil could also be varied to 3 kW. The wafer was mechanically clamped using a conventional Applied Materials perimeter clamp and substrate assembly, eliminating concerns with backside wafer electrical contact and conduction of current through the wafer. Substrate bias for these experiments was dc, variable from 0 - -100 Vdc, although rf biasing could also be used. All experiments were performed at low bias voltage, $V_{bias} = -10$ Vdc. The substrate assembly was water cooled, with the maximum measured temperature for all experiments below 50° C. The wafer position was 15 cm below the Cu cathode, and 5 cm below the 2-turn ICP coil. The coil was constructed of 1 cm copper tubing to allow water cooling through the matching network. A schematic of the deposition tooi appears in Fig. A.1.

Although not shown in Fig. A.1, the complete tool consists of two chambers, each outfitted with similar Endura-class rotating-magnet magnetron sources. The first chamber is used to deposit a Ta adhesion layer at low pressure ($\approx$ 0.2 Pa). The wafer is then passed in-situ to the ionized-PVD chamber for processing. This enables Cu to be deposited cleanly without a pre-deposition sputter clean that would be necessary following an up-to-air vent to transfer the wafer from the Ta chamber. This closely simulates the path a wafer would take to copper deposition in a production tool. The complete system is capable of processing 20

Reproduced with permission of the copyright owner. Further reproduction prohibited without permission.

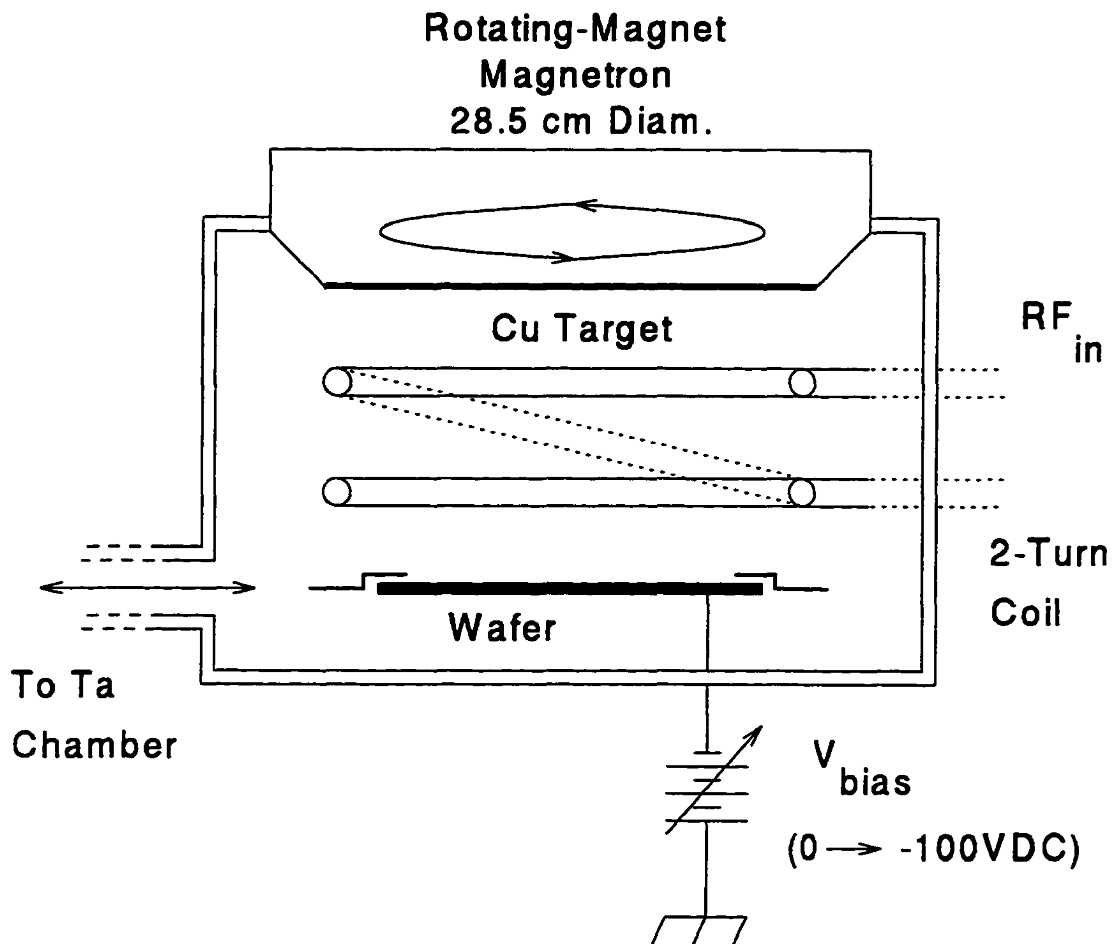

Figure A.1: Schematic view of I-PVD apparatus. Not shown is the Ta PVD chamber used to deposit an adhesive layer prior to Cu deposition.

Reproduced with permission of the copyright owner. Further reproduction prohibited without permission.

cm diameter wafers. However, for this study, only small samples in the center of the wafer position are examined.

The samples were Si wafers prepared with a SiO_2 dielectric layer. Trenches and vias were etched into the dielectric layer, with a depth of 1.2 μ, presenting a variety of aspect ratios up to AR = 2.4 (width = 0.5 μ). Prior to Cu deposition, a layer of Ta was deposited in-situ as an adhesion layer. The Ta layer was generally much thicker ($\approx$ 450Å) than that normally used as an adhesion layer ($\approx$ 50 – 100Å) to ensure good conformality. The thick Ta layer also served to assist in the analysis of each sample via high resolution SEM. Each sample was cleaved in air at room temperature.

Previous results indicate that metal-ion flux fractions (metal-ion flux/total metal flux) are highly dependent on background pressure [53, 59]. This fraction ranges from approximately 20% at 0.66 Pa to approximately 80% at 6 Pa. In this study, we maintain a pressure of 6 Pa in order to ascertain the effect of varying ICP and magnetron powers on fill directionality.

Fig. A.2(a) shows a typical damascene trench fill as found in this study. Fig. A.2(b) gives the positions measured to quantify step coverage, which is defined as the relative thickness of the film on the sidewall, top, and bottom of the trench. The particular ratios used for the discussion of directionality are $r_1 = a/c$ (bottom trench thickness/top thickness) and $r_2 = b/a$ (sidewall thickness/bottom thickness). A higher value of r_1 indicates a highly directional deposition with an ideal value of unity. A lower r_2 value is also indicative of good directionality with an ideal value of zero. These ideal values of step coverage are required because the sidewall coverage at low bias ($\approx 10V$) and low temperature ($\approx RT$) is generally columnar in structure leading to overall loss of trench conductivity. A completely directional deposition, $r_1 = 1$, would tend towards lower resistivity due to its large grain structure. The differences in bottom and sidewall film structure is evident in Fig. A.2(a).

The step coverage can be used as an empirical indication of flux fraction, provided the deposition time is long enough to provide adequate shadowing of neutrals. r_1 is particularly useful in this regard because it is directly related to the ion-to-neutral flux fraction. At this

Reproduced with permission of the copyright owner. Further reproduction prohibited without permission.

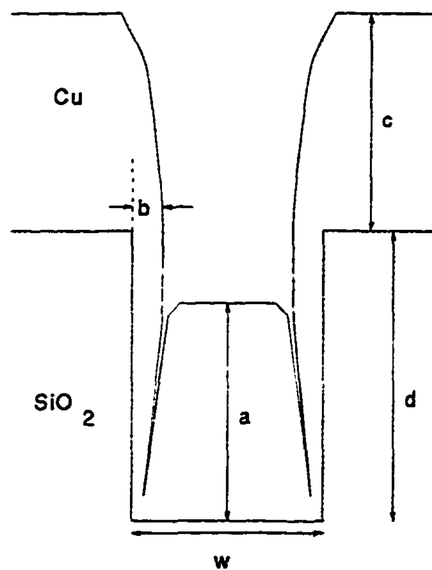

Figure A.2: (a) A representative trench fill (AR = 1.5). (b) The measurement points used for determination of step coverage.

Reproduced with permission of the copyright owner. Further reproduction prohibited without permission.

high pressure (6 Pa), sputtered neutrals lose preferential direction after several collisions with the background, so deposition at the bottom of the trench is assumed mostly due to directed ions. Also, if the assumption of unity sticking coefficient is made, r_1 measures directly the ratio of bottom deposition rate[ions]/top deposition rate[ions + neutrals]. The quantitative nature of this assumption will be tested by comparison to simulation [64].

In Fig. A.3, the ratios r_1 and r_2 are shown as ICP power is varied for several aspect ratios. The magnetron power, and thus the metal-atom density, is kept constant at 600 W. Previous experiments [53, 59] indicate that the metal-ion flux fraction saturates at $\approx 100\ W$ to a value of $\approx 85\%$. For low rf powers, $\approx 400\ W$, the directionality is seen to be lower by comparing the r_1 and r_2 ratios. As rf power is increased above 800 W, directionality increases as well, indicating an increase in copper ion flux fraction. Since r_1 seems to saturate at a value somewhat less than unity, the Cu degree of ionization must have also reached saturation.

As rf power is increased even further, beyond 1500 W, direct measurements from the SEM become difficult. In this regime of high ion fluxes collected by the wafer, enhanced surface mobility for the Cu caused recrystallization of the film. This reduced the accuracy of the thickness measurements. However, taking r_1 and r_2 together suggest a dip in the directionality at 2000 W ICP power. More tests will be needed in the high ICP power regime.

Step coverage is shown for various magnetron powers at constant ICP power (800 W) in Fig. A.4. We see that reduction of directionality by an decreasing r_1 and increasing r_2 as metal-atom density is increased. Previous results [53, 59] and modeling [63] have suggested that as metal-atom density is increased, flux fraction decreases markedly. This is primarily due to cooling of the high-density plasma by introduction of metal-atoms where the ionization potentials ($IP_{\mathrm{Cu}} = 7.7\ eV$) are much lower than the background gas ($IP_{\mathrm{Ar}} = 15.7\ eV$). This cooling phenomena can be seen by the reduction of collected substrate current as magnetron power is increased, as shown in Fig. A.5.

However, as magnetron power is increased, the local background gas density has

Reproduced with permission of the copyright owner. Further reproduction prohibited without permission.

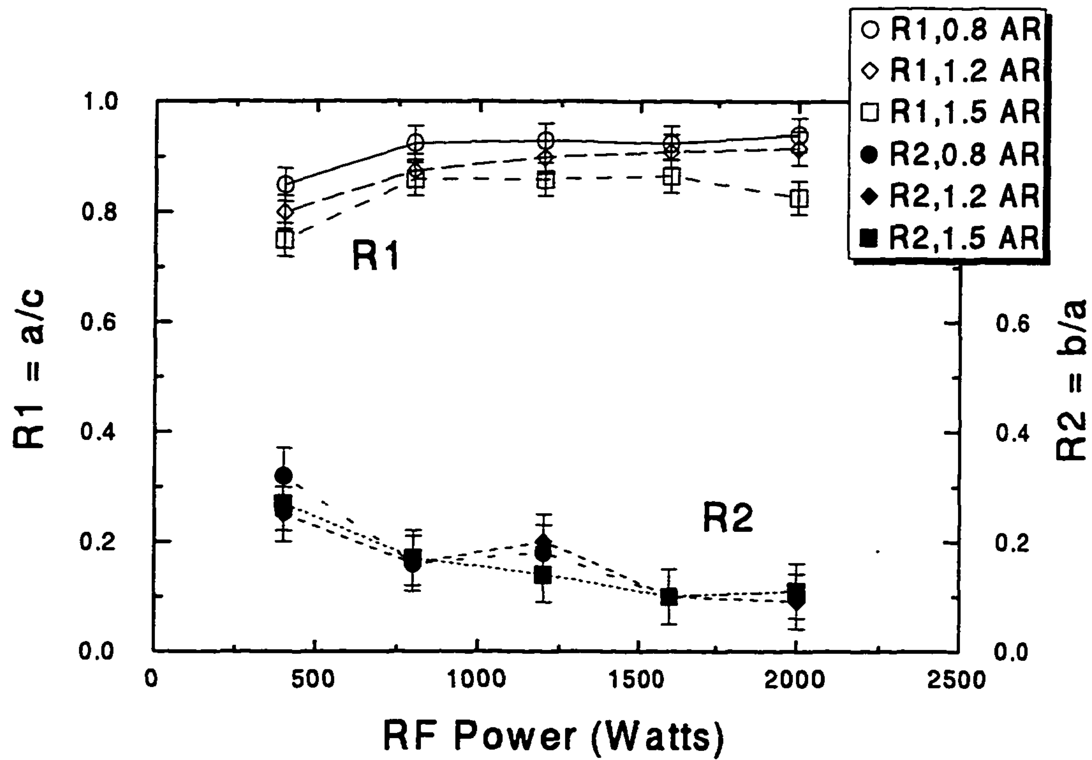

Figure A.3: Step coverage ratios, $r_1 = a/c$ and $r_2 = b/a$, shown as applied ICP power is increased. The magnetron power was kept constant at 600 W, pressure = 6 Pa, wafer bias = -10 volts.

Reproduced with permission of the copyright owner. Further reproduction prohibited without permission.

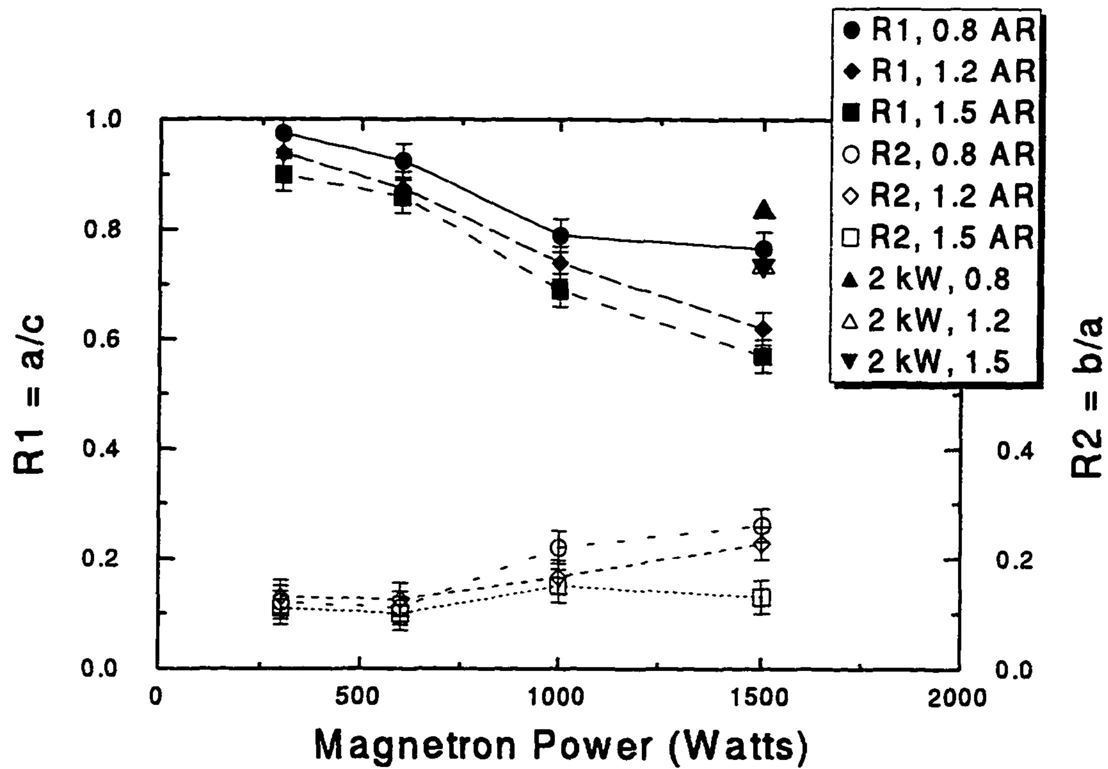

Figure A.4: Step coverage versus magnetron power. The applied ICP power was kept constant at 800 W, pressure = 6 Pa, wafer bias = -10 volts. An additional run at higher ICP power (ICP = 2 kW, Mag power = 1.5 kW) is shown as triangles.

Reproduced with permission of the copyright owner. Further reproduction prohibited without permission.

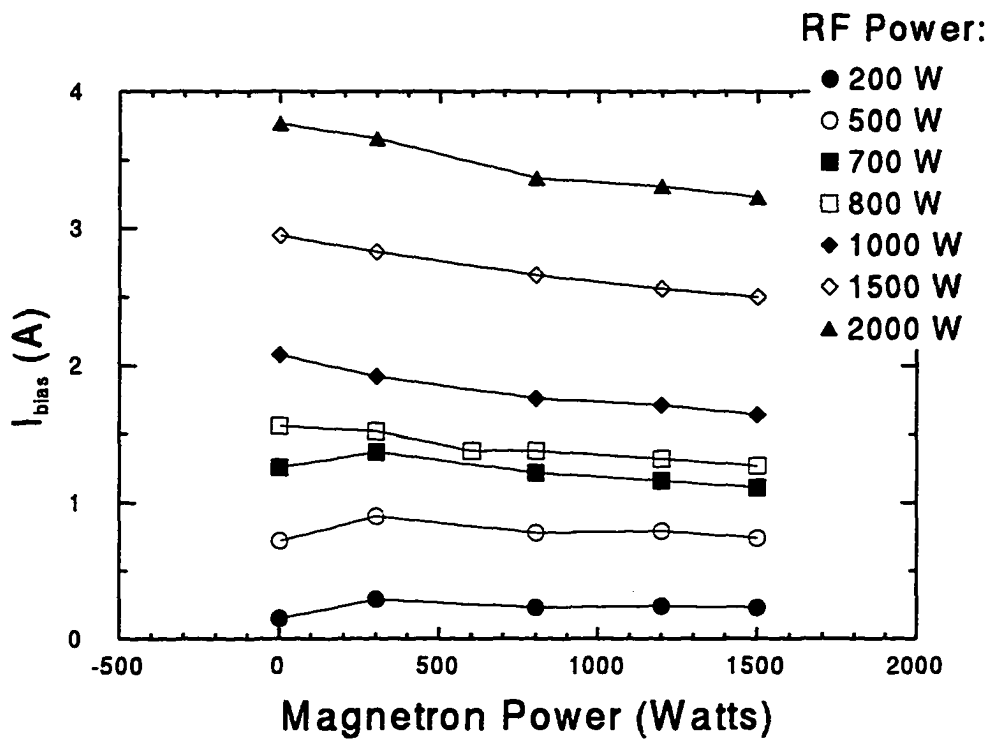

Figure A.5: Collected ion current versus magnetron power for several applied ICP powers. Wafer bias is -40 volts, which is well into ion saturation.

Reproduced with permission of the copyright owner. Further reproduction prohibited without permission.

been shown to decrease substantially [65]. This would have the effect of increasing the sputtered copper mean free path, which decreases the probability of ionization in the high density plasma [53]. This gas rarefaction effect would also likely contribute to the decrease in collected ion current vs. magnetron power in Fig. A.5.

ICP sources have been shown to saturate with rf power due to neutral depletion by rarefaction [16] under certain conditions, but collected ion current at the wafer does not indicate saturation (see Fig. A.6). In fact, as is generally the case for high-density plasma sources [16,53,59,63,66], the plasma density increases linearly with input power. This is seen in this experiment by the roughly linear increase in collected wafer current as ICP power is increased. Thus very little Cu ion flux fraction is expected to be lost due to rarefaction of the background by the ICP, although this may be more important at higher powers.

A single run was completed at ICP power = 2000 W and magnetron power = 1500 W in order to determine if the plasma cooling effect seen upon introduction of Cu atoms could be compensated by increasing ICP power. These data points appears as triangles in Fig. A.4, where we show the ratio r_1 for three aspect ratios. What we note is that incrëasing ICP power does compensate somewhat by increasing the Cu flux fraction to levels similar to that seen at $\approx 600 - 700\ W$ magnetron power. This is probably due to the increasing temperature required to maintain a high argon ion density. This suggests that one method of increasing deposition rate while maintaining directionality is simply to increase ICP power with magnetron power. The higher power regime will be studied in the future.

The Cu deposition rates for the parameter space under consideration appear in Fig. A.7. We note that the deposition rate is linear in magnetron power, which would be expected with a linear increase in Cu density. Also notable is the linearity in deposition rate with ICP power. This behavior is maintained for two constant magnetron powers, although the rate of increase is greater for the 1500 W case. The deposition rate for zero magnetron power is also shown in Fig. A.7. Part of this increase in Cu deposition rate is presumed to be due to sputtering of the copper coil through capacitive coupling. However, the zero-

Reproduced with permission of the copyright owner. Further reproduction prohibited without permission.

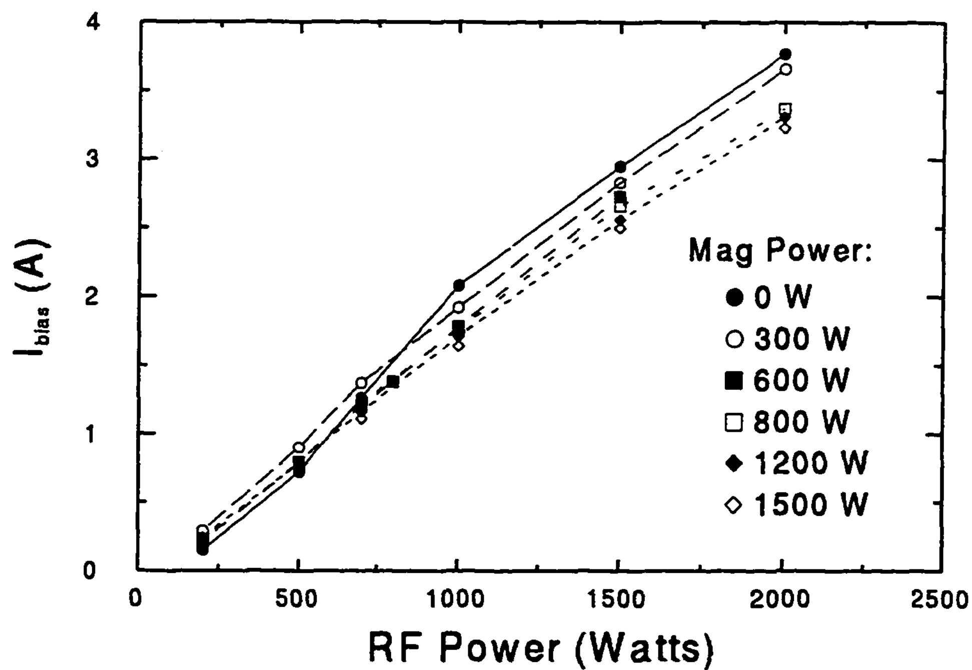

Figure A.6: Collected ion current versus applied ICP power for several magnetron powers. Wafer bias is -40 volts.

Reproduced with permission of the copyright owner. Further reproduction prohibited without permission.

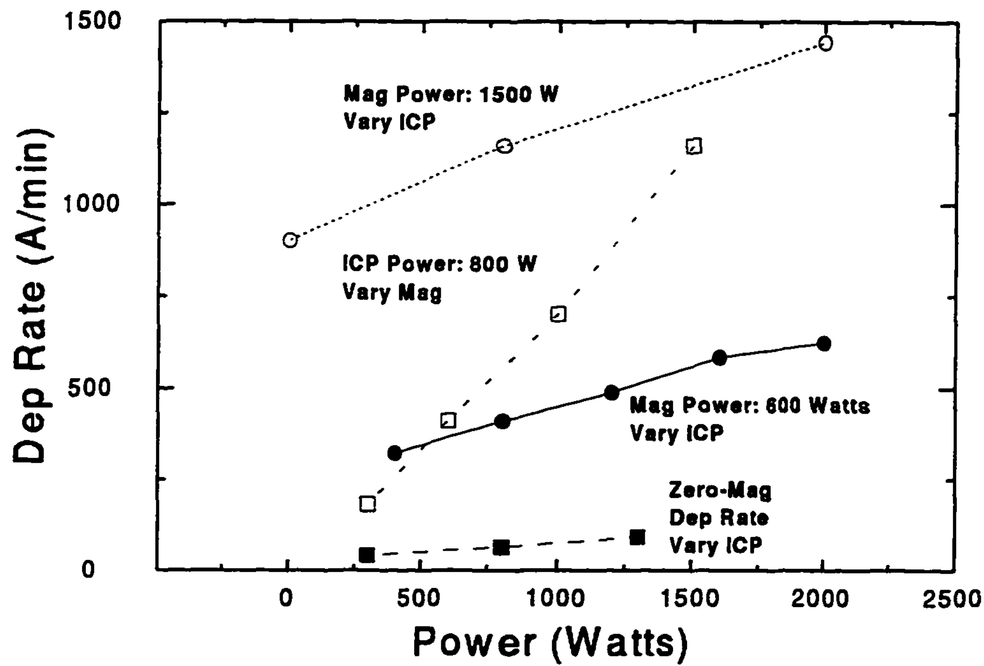

Figure A.7: Deposition rates vs. magnetron and ICP power. The deposition rates for varying ICP power at zero magnetron power is also shown.

Reproduced with permission of the copyright owner. Further reproduction prohibited without permission.

magnetron deposition rate alone does not account for the increase in deposition rate with ICP power for the 0.6 and 1.5 kW magnetron powers shown.

We note that in raising the ICP power from 800 W to 2000 W, the deposition rate increases by approximately the same factor as the increase in power. The Cu ion current density also increases by a similar factor. This suggests that as applied coil power (plasma density) is increased, sputtering from the copper coil becomes more important. Because the copper ion density increases as well, ionization of coil species appears to be as efficient as for copper originating at the Cu target. The voltages on the coil were not measured for each run, but was found to be in the range of several hundred volts.

As is shown below, the plasma becomes "copper-rich" at high magnetron powers. Thus the apparent rate of increase in deposition rate with ICP power should be larger at higher magnetron power due to the higher sputter yield of Cu on Cu over Ar on Cu. This is seen to be the case in Fig. A.7 where the slope of the deposition rate vs. ICP power is higher for 1500 W ($269\frac{\mathring{A}}{kW-min}$) than 600 W ($193\frac{\mathring{A}}{kW-min}$).

A.4 Discussion

In order to test the assumption that r_1 directly represents the Cu ion flux fraction, we compare the data to a numerical model previously used to simulate I-PVD fill profiles [64]. We find that with the assumption of non-collimated, completely isotropic neutral flux, the Cu ion flux fraction and r_1 track fairly well. However, the simulation accounts for the fraction of Cu neutral flux that does reach the bottom of the features, while letting $r_1 = \delta$ assumes only Cu ions are incident at the bottom of the trench. Thus we use the simulation value, matched to the SEM photographs, as the actual value of δ in the following discussion.

With an estimate of Cu ion flux fraction, we can also make estimates of the fraction of the total plasma density that is Cu ions. For this analysis we assume the directionality and deposition rate to be uniform over the entire wafer surface. This will not be true in general, but will be useful for qualitative estimates of global density fractions.

Reproduced with permission of the copyright owner. Further reproduction prohibited without permission.

The deposition rate of Cu, R_T, and the total collected ion current, j_T, are given by

$$R_T = R_o + R_+ \quad (A.1)$$

$$j_T = j_{Ar} + j_+ \quad (A.2)$$

where R_o = deposition rate due to Cu neutrals only, j_{Ar} = current density due to Ar ions only. The Cu ion current density, j_+, and the Cu ion deposition rate, R_+, can be related if we assume unity sticking coefficient. Further, this analysis ignores the effect of secondary electrons on the collected ion current, which is expected to introduce an error of less than 5%. Using the above assumptions

$$j_+ = \frac{I_+}{A_w} = \frac{eR_+}{d_+ A_+} \quad (A.3)$$

where A_w = area of current collecting substrate [cm^2], d_+ = diameter of a single Cu atom (2.8Å), and A_+ = area of a single Cu atom [cm^2/atom].

The Cu ion flux fraction is defined in eqn. A.4. Assuming unity sticking coefficient and using eqn. A.1

$$\delta = \frac{\Gamma_{Cu_+}}{\Gamma_{Cu_+} + \Gamma_{Cu_o}} = \frac{R_+}{R_o + R_+} \quad (A.4)$$

where Γ_{Cu_+} is the Cu ion flux and $\Gamma_{Cu_+} + \Gamma_{Cu_o}$ is the total copper flux. Eqn. A.4 gives the copper ion deposition rate, $R_+ = \delta R_T$ for a known δ.

Assuming that the collected current for each species is driven by Bohm presheath diffusion, we can write the ratio of Cu ion density to Ar ion density in the bulk of the high density plasma as

$$f = \frac{n_{Cu}}{n_{Ar}} = \sqrt{\frac{m_{Cu}}{m_{Ar}}} \frac{j_+}{j_T - j_+} \quad (A.5)$$

where m_{Cu} and m_{Ar} are the masses of copper and argon (in amu), respectively, and n_{Cu} and n_{Ar} are the individual bulk ion densities.

Fig. A.8 shows the Copper density ratio, f, using the area of the wafer clamp (diameter = 31 cm) as the current collecting surface, and the simulation values of δ. We note that as

Reproduced with permission of the copyright owner. Further reproduction prohibited without permission.

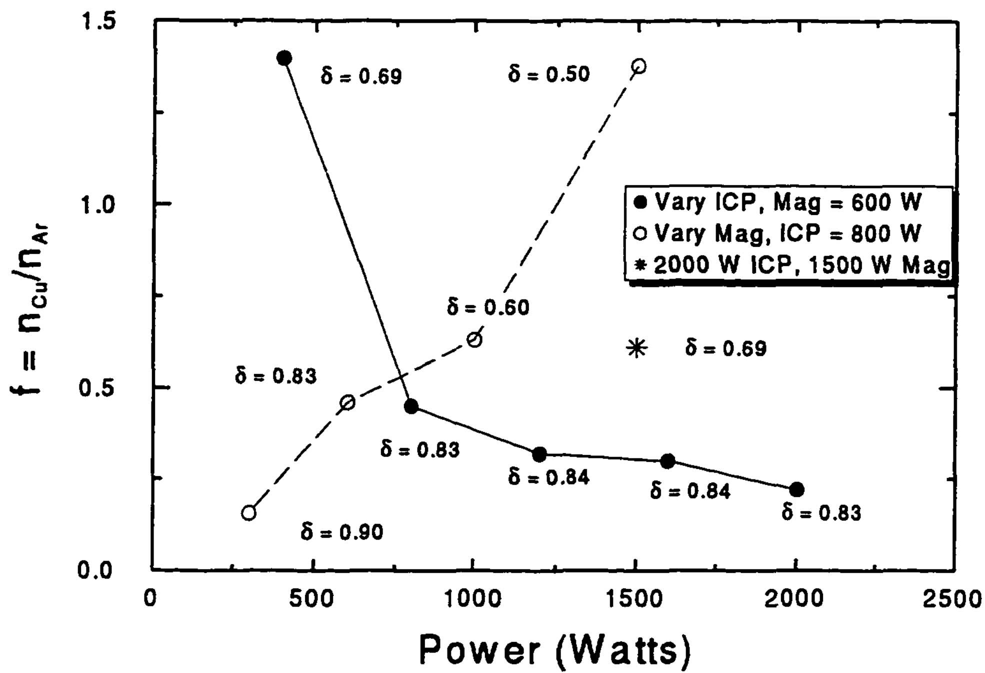

Figure A.8: Cu+/Ar+ ion density ratio vs. magnetron and ICP powers. The value of the Cu ion-flux fraction, δ, is shown for each case.

Reproduced with permission of the copyright owner. Further reproduction prohibited without permission.

we vary ICP power, while keeping magnetron power constant, the Cu/Ar ion density ratio, defined by eqn. A.5 decreases rapidly in the beginning with a slightly less dramatic falloff past $\approx 800\ W$. This indicates that most of the extra ICP power is deposited in the argon background after the Cu ion density saturates. Coupled with previous results at lower rf power [53, 59], we find that rf coupling to Cu is very efficient, while a distinct cooling effect takes place upon introduction of Cu. But as power is increased, the electron temperature also increases to accommodate coupling to argon.

The effect of varying magnetron power is also seen in Fig. A.8. Here the density of Cu increases with respect to the argon almost linearly in magnetron power. In fact, at higher magnetron powers, the copper ion density reaches almost $1\frac{1}{2}$ times that of argon at 1500 W, and may go even higher as magnetron power is increased. However the reduction in copper ion flux fraction with magnetron power suggests that while the copper density ratio, f, may increase, the accompanying decrease in electron temperature reduces the Ar ion density.

Over the range shown in Fig. A.8, magnetron power is increased by a factor of five, Cu deposition rate increases by a factor of six, and the Cu+/Ar+ ion density ratio increases by a factor of nine. However, the Cu ion flux fraction decreases by $\approx$ two over the same range. From Bohm pre-sheath assumptions,

$$j_T = 0.61e(\frac{n_{\mathrm{Cu}}}{\sqrt{M_{\mathrm{Cu}}}} + \frac{n_{\mathrm{Ar}}}{\sqrt{M_{Ar}}})\sqrt{(T_e)} \tag{A.6}$$

the ratio of total current density at power levels A and B from Figs. A.5 and A.6, and the Cu+/Ar+ ratios from Fig. A.8 we can write the ratio of Bohm currents for each species as

$$b_{+,\mathrm{Ar}} \equiv \frac{j_{+,\mathrm{Ar}_A}}{j_{+,\mathrm{Ar}_B}} = sqrt\frac{T_{e_A}}{T_{e_B}}\frac{n_{+,\mathrm{Ar}_A}}{n_{+,\mathrm{Ar}_B}} \tag{A.7}$$

In going from 300 W to 1500 W magnetron power at 800 W ICP power, we get Bohm current ratios of $b_- = 0.25$ and $b_{Ar} = 2.2$, *i.e.*, we see a four-fold increase in Cu ion flux while Ar ion flux is halved. The decrease in Ar ion flux is likely due to a decrease in electron temperature which accompanies an increase in Cu atom density [53, 59, 63]. The reduction in Cu ion flux fraction is also likely due to reduced electron temperature.

Reproduced with permission of the copyright owner. Further reproduction prohibited without permission.

We note that the increase in deposition rate due to the Cu ions is only a factor of 3.3, not the factor of four that we get for the increase in Bohm flux of Cu ions. This discrepancy can be understood by noting that the deposition rate and Cu ion flux fraction were measured at a single point (center of 20 cm wafer), while the ion current was collected over the entire surface. Thus any non-uniformities in the plasma would cause errors in this analysis. However, because the above factors agree within 20%, this error is small and the general trends are uncompromised.

It was shown previously that increasing ICP power at high magnetron powers did indeed increase directionality (see Fig. A.4). That same run (ICP power = 2 kW, magnetron power = 1.5 kW) is shown in Fig. A.8. The Cu ion flux fraction is seen to increase to δ = 0.69, from 0.5, as the ICP power is increased from 800 W to 2000 W. Further, the Cu ion density fraction decreases by a factor of approximately 2.3. Over the same range, the total collected ion current, shown in Fig. A.5, increases 2.5 times. We get Bohm flux ratios of $b_+ = 0.63$ and $b_{Ar} = 0.55$. The Ar ion flux is seen to increase slightly more than the Cu ion flux. Since the Cu ion flux fraction also increases, the electron temperature probably increases which promotes ionization of Ar and an increase in the Cu degree of ionization.

A.5 Conclusions

The ionized-PVD method has been used to fill damascene trench structures with copper. The directionality of the fill, which is closely related to the trench microstructure and thus the interconnect resistivity, has been studied as a function of ICP power and Cu atom density. It is found that the cooling of the high-density plasma associated with an increase in metal-atom density (magnetron power) decreases the fill directionality. Conversely, increasing ICP power at low magnetron power tends to increase the Cu flux fraction to an asymptotic value of approximately 85%, consistent with previous results [53]. Increasing ICP power at high magnetron powers can offset the loss of flux fraction somewhat but more work in the high power regime is needed. The effect of coil sputtering is shown to be important as ICP

Reproduced with permission of the copyright owner. Further reproduction prohibited without permission.

power is increased. The Bohm flux of Cu ions is found to increase with magnetron power is increased, while Ar ion flux decreases. Together with the Cu+/Ar+ flux ratio of Fig. A.8, this suggests that copper becomes the dominant ionic species.

Reproduced with permission of the copyright owner. Further reproduction prohibited without permission.

Bibliography

[1] R. M. Burger, J. A. Glaze, T. Seidel, and O. Williams. The SIA's roadmap: Consensus for cooperation. *Solid State Technology*, pages 38–54, Feb 1995.

[2] Stephen R. Leone. Kinetic-energy-enhanced neutral etching. *Jpn. J. Appl. Phys.*, 34(4B):2073, 1995.

[3] R. Behrisch, G. Maderlechner, B. M. U. Scherzer, and M. T. Robinson. *J. Appl. Phys.*, 18:391, 1979.

[4] H. Shin, N. Jha, X. Qian, G. W. Hills, and C. Hu. Plamsa etching charge-up damage to thin oxides. *Solid State Technology*, page 29, Aug 1993.

[5] Calvin T. Gabriel and James P. McVittie. How plasma etching damages thin gate oxides. *Solid State Technology*, page 81, June 1992.

[6] T. Mizutani and T. Yunogami. Neutral-beam-assisted etching of SiO_2 –a charge-free etching process–. *Jap. J. App. Phys.*, 29:2220, 1990.

[7] W. E. Mlynko, S. R. Kasi, and D. M. Manos. Oxide degradation effects in dry patterning of resist using oxygen beams. Materials Research Society, April 1992.

Reproduced with permission of the copyright owner. Further reproduction prohibited without permission.

[8] J. C. Arnold and H. H. Sawin. Charging of pattern features during plasma etching. *J. Appl. Phys.*, 70(10):5314, 1991.

[9] R. W. Motley, D. M. Manos, W. D. Langer, and S. A. Langer. Neutral particle surface alteration. U. S. Patent no. 4,662,977.

[10] H. D. Hagstrum. Low energy de-excitation and neutralization processes near surfaces. In N. H. Tolk, J. C. Tully, W. Heiland, and C. W. White, editors, *Inelastic Ion-Surface Collisions*, chapter 1, pages 1–26. Academic Press, New York, 1976.

[11] John William Cuthbertson. *Reflection of Plasma Ions From Metals.* PhD thesis, Princeton University, October 1991. Available from University Microfilms, Ann Arbor, MI.

[12] Michael A. Lieberman and Allan J. Lichtenberg. *Principles of plasma discharges and materials processing.* Wiley-Interscience, New York, 1994.

[13] C. Lee and M. A. Lieberman. Global model of Ar, O_2, Cl_2, and Ar/O_2 high density plasma discharges. *J. Vac. Sci. Technol.*, A13(2):368, 1995.

[14] V. A. Godyak. *Soviet Radio Frequency Discharge Research*, chapter 5. Monograph Series on the Soviet Union. Delphic Associates, Falls Church, VA, 1986.

[15] J. Hopwood, C. R. Guarnieri, S. J. Whitehair, and J. J. Cuomo. Electromagnetic fields in a radio-frequency induction plasma. *J. Vac. Sci. Technol.*, A11(1):147, 1993.

[16] J. Hopwood, C. R. Guarnieri, S. J. Whitehair, and J. J. Cuomo. Langmuir probe measurements of a radio frequency induction plasma. *J. Vac. Sci. Technol.*, A11(1):152, 1993.

Reproduced with permission of the copyright owner. Further reproduction prohibited without permission.

[17] M. S. Barnes, J. C. Forster, and J. H. Keller. Electron energy distribution function measurements in a planar inductive oxygen radio frequency glow discharge. *Appl. Phys. Lett*, 62(21):2622, May 1993.

[18] G. V. Roslyakov and G. I. Fiksel'. Source of low-energy hydrogen atoms. *Sov. J. Plasma Phys.*, 12(2):136, Feb 1986.

[19] John W. Cuthbertson, Robert W. Motley, and William D. langer. High-flux source of low-energy neutral beams using reflection of ions from metals. *Rev. Sci. Instrum.*, 63(11):5279, Nov 1992.

[20] Chodura. Plasma wall transition in an oblique magnetic field. *Phys. Fluids*, 25:1628, 1982.

[21] J. O'Hanlon. *A User's Guide to Vacuum Technology.* Wiley, 1980.

[22] A. Roth. *Vacuum Technology.* North-Holland Publishing, Amsterdam, 1976.

[23] R. A. Stewart, P. Vitello, and D. B. Graves. Two-dimensional fluid model of high density inductively coupled plasma sources. *J. Vac. Sci. Technol.*, B12(1):478, Jan/Feb 1994.

[24] J. Hopwood, D. K. Reinhard, and J. Asmussen. Charged particle densities and energy distributions in a multipolar electron cyclotron resonant plasma etching source. *J. Vac. Sci. Technol.*, A8(4):3103, Jul/Aug 1990.

[25] Milton Ohring. *The Material Science of Thin Films.* Academic Press, Boston, 1992.

Reproduced with permission of the copyright owner. Further reproduction prohibited without permission.

[26] L. C. Woods. *Kinetic Theory of Gases and Magnetoplasmas.* Oxford University Press, New York, 1993.

[27] P. W. May, D. Field, and D. F. Klemperer. Modeling radio-frequency discharges: Effects of collisions upon ion and neutral particle energy distributions. *J. Appl. Phys.*, 71(8):3721, 15 Apr 1992.

[28] B. Singh, L. J. Amore, W. Saylor, and G. Racette. Laboratory simulation of low earth orbital oxygen interation with spacecraft surfaces. In *Proc. of the 23rd Aerospace Sciences Meeting*, Reno, NV, Jan 14-17 1985. AAIA-85-0477.

[29] T. W. Motley, S. Bernabei, and W. M. Hooke. *Rev. Sci. Inst.*, 50:1586, 1979.

[30] W. H. Press, W. T. Vetterling, S. A. Teukolsky, and B. P. Flannery. *Numerical Recipes in Fortran: The Art of Scientific Computing.* Cambridge University Press, 1992.

[31] L. L. Carter and E. D. Cashwell. *Particle-Transport Simulation with the Monte Carlo Method.* U. S. Energy Research and Development Administration, 1975.

[32] W. H. Cramer. Elastic and inelastic scattering of low-velocity ions: Ne^+ in A, A^+ in Ne, and A^+ in A. *J. Chem. Phys.*, 30(3):641, 1959.

[33] Y. Weng and M. J. Kushner. Method for including electron-electron collisions in Monte Carlo simulations of electron swarms in partially ionized gases. *Phys. Rev. A*, 42(10):6192, 1990.

Reproduced with permission of the copyright owner. Further reproduction prohibited without permission.

[34] P. L. G. Ventzek, T. H. Hoekstra, and M. J. Kushner. Two-dimensional modeling of high plasma density inductively coupled sources for materials processing. *J. Vac. Sci. Technol.*, A12(1):461, 1994.

[35] M. A. Lieberman and R. A. Gottscho. Design of high density plasma sources for materials processing. In M. H. Francombe and J. L. Vossen, editors, *Physics of Thin Films*, volume 18. Academic Press, San Diego, 1994.

[36] B. E. Thompson, H. H. Sawin, and D. A. Fisher. Monte Carlo simulation of ion transport through rf glow-discharge sheaths. *J. Appl. Phys.*, 63(7):223, 1988.

[37] B. Window. Removing the energetic neutral problem in sputtering. *J. Vac. Sci. Technol.*, A11(4):1522, Jul/Aug 1993.

[38] Robert A. Brizzolara and C. Burleigh Cooper. Measurments of energy distributions of neutral Cu_2 and Cu_3 species sputtered from Cu by low energy Ar^+ ions. *Nuclear Instruments and Methods in Physics Research*, B43:136, 1989.

[39] B. Window an K.-H. Müller. Strain, ion bombardment and energetic neutrals in magnetron sputtering. *Thin Solid Films*, 171:183, 1989.

[40] D. M. Mattox. Particle bombardment effects on thin-film deposition: A review. *J. Vac. Sci. Technol.*, A7(3):1105, May/Jun 1989.

[41] J. Cross. Sematech Neutral Beam Working Group Meeting, Orlando, FL, Nov 1993. Cited with permission.

Reproduced with permission of the copyright owner. Further reproduction prohibited without permission.

[42] M. Tuszewski, J. T. Scheuer, and J. A. Tobin. Composition of the oxygen plasmas from two inductively coupled sources. *J. Vac. Sci. Technol.*, A13(3):839, May/Jun 1995.

[43] D. M. Manos and H. F. Dylla. Diagnostics of plasmas for materials processing. In D. M. Manos and D. L. Flamm, editors, *Plasma Etching: An Introduction*. Academic Press, Boston, 1989.

[44] David N. Ruzic. *Electric probes for low temperature plasmas*. Number M-13 in AVS Monograph Series. AVS Press, New York, 1994.

[45] L. Schott. Electrical probes. In W. Lochte-Holgreven, editor, *Plasma Diagnostics*, AVS Classics, chapter 11, page 669. AIP Press, New York, 1995.

[46] J. O'Neill, M. S. Barnes, and J. H. Keller. Optical ion energy measurements in a radio-frequency-induction plasma source. *J. Appl. Phys.*, 73(4):1621, 1993.

[47] Steven Koontz, Lubert Leger, Keith Albyn, and Jon Cross. Vacuum ultraviolet radiation/atomic oxygen synergism in material reactivity. *J. Spacecraft*, 27(3):346, May/Jun 1989.

[48] Sylvia T. Ceyer. New mechanisms for chemistry at surfaces. *Science*, 249:133, 13 Jul 1990.

[49] J.W. Coburn and E. Kay. *J. Vac. Sci. Technol.*, 8:738, 1971.

[50] Calvin T. Gabriel and Yosias Melaku. Gate oxide damage in a high density inductively coupled plasma. *J. Vac. Sci. Technol.*, B12(1):454, Jan/Feb 1994.

Reproduced with permission of the copyright owner. Further reproduction prohibited without permission.

[51] P. K. Gadgil, T. D. Mantei, and X. C. Mu. Evaluation and control of device damage in high density plasma etching. *J. Vac. Sci. Technol.*, B12:102, 1994.

[52] C. A. Nichols, S. M. Rossnagel, and S. Hamaguchi. Ionizied-pvd of Cu for high-aspect-ratio damascene trench fill applications. *J. Vac. Sci. Technol.*, B14(4), Sep/Oct 1996.

[53] S. M. Rossnagel and J. Hopwood. Metal ion deposition from ionized magnetron sputtering discharge. *J. Vac. Sci. Technol.*, B12(1):449, Jan/Feb 1994.

[54] J. Hopwood. Review of inductively coupled plasmas for plasma processing. *Plasma Sources Sci. Technol.*, 1:109–116, 1992.

[55] Pascal Doppelt and Thomas H. Baum. *MRS Bulletin*, page 41, Aug 1994.

[56] J. S. H. Cho, H. K. Kang, S. S. Wong, and Y. Shacham-Diamand. *MRS Bulletin*, page 31, Jul 1993.

[57] D. Mikalsen and S. M. Rossnagel. U. S. Patent 4,824,544, Apr 1989.

[58] S. M. Rossnagel, D. Mikalsen, H. Kinoshita, and J. J. Cuomo. *J. Vac. Sci. Technol.*, A9:261, 1991.

[59] S. M. Rossnagel and J. Hopwood. *Appl. Phys. Lett.*, 63:3285, 1993.

[60] Peter F. Cheng, S. M. Rossnagel, and David N. Ruzic. *J. Vac. Sci. Technol.*, B13(2):203, 1995.

[61] S. M. Rossnagel. *Thin Solid Films*, 263:1, 1995.

Reproduced with permission of the copyright owner. Further reproduction prohibited without permission.

[62] W. M. Holber, J. S. Logan, H. J. Grabarz, J. T. C. Yeh, J. B. O. Caughman, A. Sugarman, and F. E. Turene. *J. Vac. Sci. Technol.*, A11(6):2903, 1993.

[63] J. Hopwood and F. Qian. Mechanisms for highly ionized magnetron sputtering. *J. Appl. Phys.*, 78(2):758, 1995.

[64] S. Hamaguchi and S. M. Rossnagel. *J. Vac. Sci. Technol.*, B13(2):183, 1995.

[65] S. M. Rossnagel. *J. Vac. Sci. Technol.*, A6(1):19, 1988.

[66] John H. Keller, John C. Forster, and Micheal S. Barnes. *J. Vac. Sci. Technol.*, A11(5):2487, 1993.

Reproduced with permission of the copyright owner. Further reproduction prohibited without permission.

Vita

Christopher Allan Nichols

Chris was born in Little Rock, Arkansas on 06/28/68. He attended High School at Searcy High School in Searcy, Arkansas and graduated in June, 1986. He married Cathy Lynn Turnbull on May 19, 1990 in Searcy, Arkansas. Chris received his Bachelor of Science degree in Physics from Arkansas State University in Jonesboro, Arkansas in May, 1991. Following undergraduate studies, Chris entered the Physics department of The College of William & Mary in Virginia where he received his Master of Science in Physics in December, 1992. Chris will begin a post-doctoral position with the Microelectronics Development Laboratory of Sandia National Labs in Albuquerque, New Mexico on July 1st, 1996. Chris and his wife are expecting their first son in mid-November, 1996.

Reproduced with permission of the copyright owner. Further reproduction prohibited without permission.